



저작자표시-비영리-변경금지 2.0 대한민국

이용자는 아래의 조건을 따르는 경우에 한하여 자유롭게

- 이 저작물을 복제, 배포, 전송, 전시, 공연 및 방송할 수 있습니다.

다음과 같은 조건을 따라야 합니다:



저작자표시. 귀하는 원저작자를 표시하여야 합니다.



비영리. 귀하는 이 저작물을 영리 목적으로 이용할 수 없습니다.



변경금지. 귀하는 이 저작물을 개작, 변형 또는 가공할 수 없습니다.

- 귀하는, 이 저작물의 재이용이나 배포의 경우, 이 저작물에 적용된 이용허락조건을 명확하게 나타내어야 합니다.
- 저작권자로부터 별도의 허가를 받으면 이러한 조건들은 적용되지 않습니다.

저작권법에 따른 이용자의 권리는 위의 내용에 의하여 영향을 받지 않습니다.

이것은 [이용허락규약\(Legal Code\)](#)을 이해하기 쉽게 요약한 것입니다.

[Disclaimer](#)

박사학위논문

Data uncertainty and predictability
of tropical cyclone wind radius

제주대학교대학원

해양기상학협동과정

김혜지

2022년 8월

열대저기압 바람반경의 자료 불확실성과 예측가능성

지도교수 문 일 주

김 혜 지

이 논문을 이학 박사학위 논문으로 제출함

2022년 6월

김혜지의 이학 박사학위 논문을 인준함

심사위원장	최광용	
위 원	문일주	
위 원	강노영	
위 원	차문정	
위 원	김성훈	

제주대학교 대학원

2022년 6월

Data uncertainty and predictability of tropical cyclone wind radius

Hye-Ji Kim

(Supervised by Professor Il-Ju Moon)

A thesis submitted in partial fulfillment of the requirement for the
degree of Doctor of Science

2022. 6.

This thesis has been examined and approved.

Thesis director, Gwangyong Choi, Prof. of Geography Education in JNU

Il-Ju Moon, Prof. of Marine Industry and Maritime Police in JNU

Nam-Young Kang, Prof. of Department of Geography in KNU

Eun-Jeong Cha, Ph. D. of National Institute of Meteorological Science

Sung-Hun Kim, Ph. D. of Korea Institute of Ocean Science & Technology

June, 2022

Interdisciplinary Postgraduate Program
in Marine Meteorology

GRADUATE SCHOOL
JEJU NATIONAL UNIVERSITY

Contents

Abstract	i
List of Figures	v
List of Tables	xi
List of Acronyms	xiii
1. Introduction	1
2. Comparison of tropical cyclone wind radius estimates between KMA, JMA, and JTWC	5
2.1. Introduction.....	5
2.2. Data and methods.....	9
2.3. Results.....	11
2.3.1. Comparison of wind radius estimates between the three agencies.....	11
2.3.2. Relationship between wind radii and potential TC size–related environmental variables	17
2.3.3. Asymmetrical characteristics	22
2.3.4. Case studies comparing TC wind radius estimates.....	26
2.4. Summary and discussion	35
3. Tropical cyclone wind radius prediction based on a statistical-dynamical approach and track pattern clustering	38
3.1. Introduction	38
3.2. Data and methods	42

3.2.1. Data.....	42
3.2.2. Calculation of dependent variable and predictors.....	43
3.2.3. Clustering method and its effect	47
3.2.4. Regression method of statistical-dynamical model	50
3.2.5. Estimation of symmetric wind radius	51
3.3. Statistical-dynamical TC wind radius prediction scheme	53
3.3.1. Effect of clustering on dependent variable	53
3.3.2. Characteristic and selection of predictor.....	58
3.4. Comparison of model performances.....	65
3.4.1. Training and testing periods	65
3.4.2. Real-time predictions of dependent variable, R30, and R50	71
3.5. Summary and discussion	81
4. Prediction of the gale wind radius in western North Pacific based on Global Forecast System	84
4.1. Introduction.....	84
4.2. Data and methods.....	87
4.2.1. Information of TC and model input.....	87
4.2.2. Preprocessing of TC wind field	89
4.2.3. Estimation of gale wind radius of TC.....	92
4.3. Results.....	95
4.3.1. Comparison of R30 estimates in four experiments.....	95
4.3.2. Predictions of longest and shortest R30.....	100

4.4. Summary and discussion	105
5. Conclusion	107
References	110
국문 초록	121

Abstract

The size of a tropical cyclone (TC) has important implications in terms of disaster prevention as it can determine the area directly affected by storms. However, the TC size has not been studied extensively, mainly due to the lack of long-term and objective observation datasets and the issues such as difficulty in determining a reasonable TC size so far. This dissertation covers three topics related to TC size in terms of wind radii: (i) comparison of tropical cyclone wind radius estimated by Korean, Japanese, and U.S agencies, (ii) tropical cyclone wind radius prediction based on statistical-dynamical approach and track pattern clustering, and (iii) prediction of the gale wind radius in western North Pacific based on Global Forecast System.

First, this study compared estimates of gale-force wind radii (R30 or R34) and storm-force wind radii (R50) of tropical cyclones (TC) by three agencies—the Korea Meteorological Administration (KMA), the Japan Meteorological Agency (JMA), and the Joint Typhoon Warning Center (JTWC)—in the western North Pacific during 2015–2018 and investigated the characteristics of these estimates. The results showed that the KMA's R30 and R50 estimates were smaller (38% and 29%, respectively) than those of the JMA, and larger (11%) for R30 and smaller (12%) for R50 than those of the JTWC. The differences between these agencies seem to be largely determined by whether the agency estimates wind radii based only on a TC's own winds or on TC winds combined with other mid-latitude synoptic systems to make TC warnings more comprehensive. The former is mainly the practice of the KMA and JTWC, whereas the latter is mainly the practice of the JMA. The factors considered for estimating wind

radii also differ between the agencies: the KMA heavily relies on TC intensity—the higher the intensity, the larger the radius—while the JMA and JTWC rely less on TC intensity than the KMA but additionally consider the latitude and storm translation speed in their estimations. In particular, the TC translation speed considered by the JMA and JTWC explains why their estimated wind radii exhibit, on average, greater asymmetries (i.e., greater differences between the longest and shortest radii) than those estimated by the KMA.

Second, an operational scheme for predicting the symmetric R30 and R50 of WNP TCs has been developed using a statistical regression method and track pattern clustering. For model training, TC tracks classified at 5-day intervals were categorized into four clusters based on the fuzzy c-means clustering method. The statistical-dynamical model employs multiple linear regressions of 2 to 8 variables selected from 11 predictors at each cluster and forecast time. The dependent variable for prediction is the change in the 5-kt wind radius (R5)—a proxy of TC size—relative to initial time. To avoid overfitting and multicollinearity among variables, smart predictors are selected using an Elastic Net regression method. The performance of model is compared for training (2008~2016) and testing (2017~2018) periods. The effect of clustering on TC size prediction was evaluated by comparing the performance of non-clustering and clustering models. The results showed that the clustering model improved the prediction of TC size by 3-24% at all lead times during the training period, especially with a significant improvement of up to 43% in Cluster 2. During the test period, the clustering model also reduced the mean error at all lead times, with the greatest improvement in Cluster 2, although the improvement was relatively small

compared to the training period. In cluster 2, most TCs develop strongly and continue to increase in size, which greatly reduced the standard deviations (or variability) in TC size through clustering, allowed for smarter predictor selection, and ultimately improved TC size prediction. In the real-time R30 and R50 predictions for 2017 and 2018 TCs, the average mean absolute error at all lead times was 61 ± 27 km and 21 ± 9 km for R30 and R50, respectively, and the error of the clustered model was 18-19% less than that of the non-clustered model. The analysis reveals that the real-time prediction errors of the current model increase due to the inherent errors of TC intensity prediction and R5 estimate as well as when the TC tracks are located between two clusters, making it difficult to classify them into specific clusters.

Finally, an automated system for objectively estimating and predicting the gale wind radius or R30 of WNP TCs has been developed using the predicted wind data of the Global Forecast System (GFS). To effectively estimate the longest and shortest R30 from the GFS dataset in the system, the filtering technique for extracting the TC itself winds is applied to the 1000 hPa and 850 hPa wind fields. The results showed that the use of an 850 hPa wind field with filtering has significant improvements to the performance of the R30 estimates, especially in the shortest R30. For real-time R30 prediction, 5-day forecast wind fields are applied to the final system, including filtering technique and bias correction. The performance of predicted R30 before the 48-h forecast time has been greatly improved by the use of 850 hPa winds, with a mean absolute error of 53 km and 48 km, on average, in the longest and shortest axes, respectively.

Key words: tropical cyclone, wind radii, prediction, statistical regression method, track pattern clustering, filtering technique

List of Figures

- Figure 2.1. Scatter plots of tropical cyclone wind radius estimates of the KMA, JMA, and JTWC. The top (R30) and bottom (R50) panels compare the KMA and JMA (a, d), the KMA and JTWC (b, e), and the JMA and JTWC (c, f). Correlation coefficients (r) and mean differences (MD) between the agencies are indicated in the bottom right corner of each panel. The unit of MD is km..... 12
- Figure 2.2. Mean differences in wind radius estimates between the KMA and JMA (black), between the KMA and JTWC (red), and between the JMA and JTWC (blue) for each bin of R30 (a) and R50 (b). The bins were divided based on the tropical cyclone wind radius estimates of the KMA. The error bars indicate standard deviations. The gray bar graph represents the numbers (N) of R30 and R50 samples for each bin at 100- and 50-km intervals, respectively. The filled circles indicate significant differences at the 95% level..... 13
- Figure 2.3. Comparisons of the spatial distributions of tropical cyclone R30 (top panels) and R50 (bottom panels) between the KMA (a, d), JMA (b, e), and JTWC (c, f) during 2015–2018. In each grid, the values were averaged along a moving window of 4° by 4° to smooth the wind radius of each grid..... 14
- Figure 2.4. Comparisons of the spatial distributions of mean differences in tropical cyclone R30 (top panels) and R50 (bottom panels) between the KMA and JMA (a, d), between the KMA and JTWC (b, e), and between the JMA and JTWC (c, f) during 2015–2018. In each grid, the values were averaged along a moving window of 4° by 4° to smooth the wind radius of each grid..... 16
- Figure 2.5. Spatial distributions of maximum wind speed (V_{max}) (a), TC translation speed (TCTS) (b), and storm age (Age) (c) based on the KMA best track data during 2015–2018. In each grid, the values were averaged along a moving window of 4° by 4° for smoothing..... 19
- Figure 2.6. Comparison of the mean values (circles) and standard deviations (error bars) in each bin of maximum wind speed (V_{max}) (a, e), latitude (b, f), TC translation speed (TCTS) (c, g), and storm age (Age) (d, h) for R30 (top panels) and R50

(bottom panels) estimates of the KMA (black), JMA (red), and JTWC (blue). The bins are divided into intervals of 10 kts, 5°N, 2 m s ⁻¹ , and 1 day for Vmax, latitude, TCTS, and storm age, respectively.....	21
Figure 2.7. Same as in Figure 2.3, but for mean asymmetry values of tropical cyclone wind radii.	24
Figure 2.8. Same as in Figure 2.6, but for mean asymmetry values of tropical cyclone wind radii.	25
Figure 2.9. Comparison of mean R30 value estimates of the KMA (blue), JMA (red), and JTWC (green) with the mean (solid black line) and top 20% (dashed black line) R30 values estimated from GFS winds at 1000 hPa for Typhoon Jebi (2018) from 00:00 UTC on August 31 to 18:00 UTC on September 12 at 6-h intervals. The solid gray line represents the maximum wind speed (Vmax) estimated by the JMA. The triangles indicate the times of the spatial distributions presented in Figure 2.11.....	27
Figure 2.10. Mean radial wind profiles of 1000-hPa GFS wind at 18:00 UTC on September 4 when Typhoon Jebi (2018) rapidly weakened. Thin and thick black lines indicate mean and top-20% mean values, respectively. Blue, red, and green dashed lines indicate R30s estimated from the KMA, JMA, and JTWC, respectively. Points A and B are where Vmax is 15 m s ⁻¹ . At 18:00 UTC on September 4, all mean radial winds (thin black line) were less than 15 m s ⁻¹ , which explains why the model-estimated mean R30 was zero in Figure 2.9.....	28
Figure 2.11. Comparison of R30 (gray contour) estimated from the GFS winds (shade) at 1000 hPa with the mean R30 values estimated by the JMA (red circle), KMA (blue circle), and JTWC (green circle) for Typhoon Jebi (2018) at 06:00 UTC on September 1 (a), 06:00 UTC on September 3, 06:00 UTC on September 4 (c), and 18:00 UTC on September 4 (d). The red crosses indicate the tropical cyclone's center. The maximum wind speed (Vmax) estimated by the JMA and the mean R30 values of the three agencies are shown in each panel.....	30
Figure 2.12. Comparison of the R30 asymmetries (a) estimated by the KMA (blue), JMA (red), and JTWC (green) with the TC translation speed (TCTS) (b) for Typhoon Soulik (2018) from 00:00 UTC on August 16 to 06:00 UTC on August 24 at 6-h intervals.	

The triangles represent the times of the spatial distributions presented in Figure 2.13..... 31

Figure 2.13. Comparison of R30 (gray contours) estimated from the GFS winds (shade) at 1000 hPa with the longest and shortest R30 values estimated by the JMA (red circle), KMA (blue circle), and JTWC (green circle) for Typhoon Soulik (2018) at 12:00 UTC on August 16 (a), 00:00 UTC on August 19 (b), 06:00 UTC on August 22 (c), and 00:00 UTC on August 24 (d). The solid and dashed circles indicate the longest and shortest R30. The red crosses indicate the tropical cyclone’s center. The maximum wind speed (Vmax) estimated by the JMA and the longest and shortest R30 of the three agencies are shown in each panel. 33

Figure 3.1. Tangential winds estimated from the GFS analysis winds (shade, $m s^{-1}$) at 850 hPa for Typhoon Trami (2018) at 12:00 UTC on September 29 (a), 18:00 UTC on October 1 (b), 00:00 UTC on October 3 (c), and 00:00 UTC on October 6 (d). The solid circles indicate the 500 km radius from the storm center (black cross) for calculating V500 and R5 (right corner in each panel). The maximum wind speed (Vmax) from JMA best track is shown in the bottom left corner of each panel, respectively..... 44

Figure 3.2. Value of three scalar validity measures according to the number of clusters. (a) Partition coefficient (PC), (b) Xie and Beni’s index (XB), and (c) alternative Dunn index (DI)..... 48

Figure 3.3. Scatter plots of averaged R30 (top panels) and R50s (bottom panels) between estimates from JMA best track data (x-axis) and estimates as a function of the TC intensity and R5 (y-axis, Equation (3.9) and (3.10) for R30 and R50, respectively) during the training (2008-2016, left panels) and testing (2017-2018, right panels) periods. The correlation coefficient (r), mean absolute error (MAE), number of samples (N), and bias (only testing period) are presented in the right bottom corner of each panel..... 52

Figure 3.4. TC tracks in the western North Pacific classified using the fuzzy c -Means clustering method for the training period from 2008-2016. Each panel represents the TC tracks in classified four clusters (light gray) and their mean track of C1 (dark gray), C2 (red), C3 (blue), and C4 (green) with the number of cases in

parentheses. For the classified similar tracks, TC tracks are interpolated equally
 21 storm positions with 5-day tracks..... 54

Figure 3.5. Correlation coefficients between eleven predictors, (a) iSIZE, (b) VM, (c) DVMX,
 (d) LAT, (e) VWS, (f) RH, (g) D200, (h) RV850, (i) SST, (j) RSST, and (k) PI and
 the change in TC size ($\Delta R5$) for four clusters of C1-C4 (gray, red, blue, and green
 circle lines) and all TC cases (black and bold lines) using all TCs at 6-, 24-, 48-,
 72-, 96-, and 120-h forecast lead times during the training period (2008-2016).
 61

Figure 3.6. Maps of regression coefficients (shade) of final selected predictors (y-axis) for All
 TC cases and four clusters of C1-C4 (x-axis) using Elastic Net multiple linear
 regression at 24- (a), 48- (b), 72- (c), 96- (d), and 120-h (e) forecast lead times
 during the training years of 2008-2016. Number of selected predictors are
 indicated in parentheses with gray text (ranging 2-8 predictors). 63

Figure 3.7. Comparisons of MAEs (a, c), R^2 (b, d), and bias (only testing, e) for $\Delta R5$
 predictions between the clustering (four clusters, black and solid lines) and non-
 clustering cases (all TCs, black dashed lines) at each lead time during the training
 (2008-2016, a-b) and testing periods (2017-2018, c-e). The unit of $\Delta R5$ is km (1
 degrees latitude = 111.11km). Sample sizes are indicated in parentheses at bottom
 of each panel for 0-, 24-, 48-, 72-, 96-, and 120-h forecast lead times. 66

Figure 3.8. Scatter plots of $\Delta R5$ predictions using a clustering (black circle) and non-
 clustering model (orange cross) compared with $\Delta R5$ estimates (x-axis) at 72-h (a,
 d), 96-h (b, e), and 120-h (c, f) forecast lead times for C1 (a-c) and C4 (d-f) during
 the testing period (2017-2018). The bias of the results is indicated in the bottom
 right corner of each panel by clustering (black text) and non-clustering model
 (orange text). The unit of $\Delta R5$ is km. 69

Figure 3.9. Schematic diagram of the present statistical-dynamical model for real-time R30
 and R50 predictions..... 72

Figure 3.10. The same as Figure 3.7, but for MAEs (a), R^2 (b), and bias (c) of real-time
 predictions of $\Delta R5$ 73

- Figure 3.11. Scatter plots of $\Delta R5$ predictions using a clustering (black cross) and non-clustering models (orange cross) of real-time cases and clustering model of testing cases (gray circles) compared with $\Delta R5$ estimates (x-axis) at 24-h (a), 48-h (b), 72-h (c), 96-h (d), and 120-h (e) forecast lead times for all TC cases in 2017 and 2018. The unit of $\Delta R5$ is km. 75
- Figure 3.12. Comparisons of MAEs for real-time R30 (a) and R50 (b) predictions between the clustering (four clusters, black solid lines) and non-clustering cases (all TCs, black dashed lines) at each lead time. The unit of MAE is km. 76
- Figure 3.13. TC tracks of Typhoon Sanvu (blue line) and Lan (red line) in 2017, and Typhoon Mangkhut (yellow line) and Soulik (purple line) in 2018. The thick black lines in map represent the mean track for four clusters. 78
- Figure 3.14. Results of individual R30 predictions (gray lines) using a present TPC-based statistical-dynamical model (a-d) and time series of the track membership coefficient (blue lines) and intensity (red lines) of TC (e-f) for Typhoons Sanvu (a, e), Lan (b, g), Mangkhut (c, f), and Soulik (d, f). The black solid and dashed lines in (a-d) indicate R30 estimates of the model and best track. The numbers at the bottom of the panels of (a-d) denote corresponding cluster number. 80
- Figure 4.1. Comparison of the spatial wind fields (shade) from GFS model analysis for using the four experiments, CTRL1000 (a), KF1000 (b), CTRL850 (c), and KF850 (d), and the R30 (black and solid contours) for Typhoon Wukong (2018) at 00:00 UTC on July 24 (upper-left corner in (a) with red text). Red plus symbols indicate the tropical cyclone's center. Red and blue dashed circles indicate the longest and shortest axes of R30 from the KMA best track. The maximum wind speed (V_{max}) from KMA is shown in (a). 91
- Figure 4.2. Comparison of radial wind profiles as the same case in Figure 4.1 for four experiments, CTRL1000 (a), KF1000 (b), CTRL850 (c), and KF850 (d) and longest (red profiles and values) and shortest (blue profiles and values) axes of R30 extracted from the sixteen profiles (gray) in the current system. Black solid and dashed lines indicate the longest axis and shortest axis of R30 from the KMA best track, by 250 km and 180 km, respectively..... 93

Figure 4.3. Comparison of estimates of longest (a-b) and shortest R30 (c-d) after bias correction from KF1000 (a, c) and KF850 (b, e), compared with KMA best track data during 2015-2019. Correlation coefficients (r) and mean absolute errors (MAE) are indicated in the bottom right corner of each panel. The unit in MAE is km..... 98

Figure 4.4. Schematic procedure for predicting the longest and shortest axes of R30 in this system..... 101

Figure 4.5. Comparisons of MAEs (a, c), R^2 (b, d), and bias (c, e) for longest (a-c) and shortest (d-e) R30 predictions of the outputs in current system (KF experiments, solid lines) and CTRL experiments (dashed lines) at 1000 hPa (black) and 850 hPa (red) using a model forecast wind fields at each lead time. The units of MAE and bias is km. 103

List of Tables

Table 2.1. Comparison of mean tropical cyclone wind radius values and their standard deviations between the KMA, JMA, and JTWC. “ <i>N</i> ” indicates the number of samples. The parenthetical values represent the difference between KMA and other agencies, and the ratio of the difference to the KMA value.....	12
Table 2.2. Pearson’s correlation coefficients and their <i>p</i> -values between tropical cyclone wind radii (R30, R50) and tropical cyclone size–related environmental variables (maximum wind speed, latitude, TC translation speed, and storm age) for the three agencies. The units of Vmax, Latitude, TCTS, and Storm age are kt, °N, m s ⁻¹ and day, respectively..	18
Table 2.3. Same as in Table 2.1, but for mean asymmetry of tropical cyclone wind radii. Normalized values are shown in parentheses.....	23
Table 3.1. List of static and synoptic potential predictors used in the present statistical-dynamical model.	46
Table 3.2. Comparison of mean values of ΔR5 for four clusters and all TCs at 24-, 48-, 72-, 96-, and 120-h forecast lead times during training period. The standard deviations of mean values are indicated in parentheses. The unit is degrees latitude (in parentheses in the first column).	55
Table 3.3. Comparisons of standard deviations (σ_{all} and σ_c) of ΔR5 using their mean value for each cluster and at each forecast lead time. The reduction rates of σ_c relative to σ_{all} are indicated in parentheses with bold text.	57
Table 3.4. Same as Table 3.2, but a comparison of the three static predictors, iSIZE, VM, and LAT. Only the standard deviations of the overall mean value for each cluster and all TCs are shown in parentheses.	60
Table 3.5. Comparison of relative error reduction of ΔR5 predictions for four clusters (C1-C4) compared to all TCs during training and testing periods at 24-, 48-, 72-, 96-, and 120-h forecasting times. Negative values in bold here indicate that the clustering	

model has improved by that result. The sample sizes are shown in parentheses at the bottom of each relative error reduction. 67

Table 3.6. Comparison of averaged MAE and NMAEs of real-time R30 and R50 predictions using the clustering and non-clustering models for four clusters..... 77

Table 4.1. The brief names and descriptions of four sensitivity experiments..... 90

Table 4.2. Mean absolute error (MAE), correlation coefficient (r), and R30 bias between the longest and shortest axes of R30s estimated from four sensitivity experiments (see Table 4.1) and KMA best track data. Units for R30 bias and MAE are km. 96

Table 4.3. The equations for bias correction (slope and y-intercept) and the mean absolute errors (MAEs) of fitted R30 estimates in four experiments. The unit of MAE is km. 97

List of Acronyms

ASCAT	Oceansat-2 Advanced Scattrometer
CLIPER	statistical wind radius climatology and persistence
D200	divergence at 200 hPa
DI	Dune index
DVMX	intensity change within 12 hours
FCM	fuzzy <i>c</i> -means clustering
GFS	Global Forecast System
HyCOM	Hybrid Coordinate Ocean Model
IBTrACS	International Best Track Archive for Climate Stewardship
iSIZE	initial tropical cyclone size based on R5
JMA	Japan Meteorological Agency
JTWC	Joint Typhoon Warning Center
KF	Kurihara filtering
KP	Korean Peninsular
LASSO	least absolute shrinkage and selection operator
LAT	sine of tropical cyclone latitude
MAE	mean absolute error
MTCSWA	Multiplatform Tropical Cyclone Surface Wind Analysis
NCODA	Navy Coupled Ocean Data Assimilation
NHC	National Hurricane Center
NMAE	normalized mean absolute error

NWP	Numerical weather prediction
PC	partition index
PI	empirical potential intensity
R30	maximum extents of 30-kt wind
R34	34-kt wind radii
R50	50-kt wind radii
R5	azimuthal mean radius of 5 kt
R64	64-kt wind radii
RH	environmental relative humidity
ROCI	radius of the outermost closed isobar
RSST	relative sea surface temperature
RV850	relative vorticity at 850 hPa
SST	sea surface temperature
TC	tropical cyclone
TCTS	tropical cyclone translation speed
TPC	track pattern clustering
VM	current tropical cyclone intensity
VWS	vertical wind shear
WNP	western North Pacific
XB	Xie and Beni index

1. Introduction

Tropical cyclones (TCs) are one of the most devastating natural disasters in the western North Pacific (WNP), resulting in enormous economic and human losses in coastal regions (Song et al., 2020). The destructive potential of a TC is not only related to its maximum sustained wind speed, but also to the TC size in terms of the radial extent of the near-surface wind (Powell and Reinhold 2007; Irish et al. 2008; Matyas 2010). Therefore, understanding of the structures of TCs such as the evolution of the inner and outer cores (Kimball and Mulekar, 2004), and physical factors that cause TC size changes (Holland and Merrill 1984; Lin et al. 2014; Chavas et al. 2017; Chan and Chan 2018), it is important for improving the TC size prediction skill.

In general, the structure of a TC vortex can be defined as a set of parameters: central pressure, maximum wind speed, a radius of maximum wind speed radius, and outer TC size, such as gale-force wind radius and radius of the outermost closed isobar (ROCI) (Weber et al., 2014). In early studies, Brand (1972) and Merrill (1984) used the ROCI as the metric of outer size. In particular, ROCI is known to be related to the tangential wind speed profiles. When the ROCI is larger (smaller), the TC's tangential wind speed profile is broader (compact) (Merrill 1984). Since the launch of scattermeters in 1999, the satellite-based ocean surface winds have been utilized for a more realistic estimation of TC outer size in terms of wind fields by various metrics such as 17 m s^{-1} (Chan and Chan, 2012), 15 m s^{-1} (Shoemaker 1989; Cocks and Gray 2002), and 12 m s^{-1} (Chavas and Emanuel, 2010; Chavas et al., 2016). Instead of surface wind data, Knaff et al. (2014) employed tangential winds at the 850 hPa and then estimated

an azimuthal mean radius of 5 kt (R_5 , about 2.5 m s^{-1}) from a combination of satellite infrared data and a climatological linear model of the outer wind field. However, it is still difficult to estimate the vortex structure and define the TC size well, especially in terms of wind speed. First, when the TC is affected by the monsoon trough, it is difficult to determine where the monsoon westerlies or trade easterlies end and where TC circulation begins. Second, TCs frequently have large-scale asymmetries because it is highly influenced by the surrounding the TC background weather system (Weber et al., 2014).

Global TC warning centers, including the National Hurricane Center (NHC), the Joint Typhoon Warning Center (JTWC), the Japan Meteorological Agency (JMA), and Korea Meteorological Administration (KMA), estimate the TC size based on the maximum radial extent of critical wind speed thresholds, such as 30-, 34-, 50-, and 64-kt wind radii, from the storm center (hereafter R_{30} , R_{34} , R_{50} , and R_{64} respectively). However, the time constraints under which forecasters operate and the subjectivity of the methods by agencies still make it challenging to issue accurate TC size advisory and warnings (Pérez-Alarcón et al., 2021). TC agencies generally use similar observations, such as satellite images and scatterometers in their postseason analysis to generate wind radius, but each agency has its own method of estimating TC wind radii, which results in different estimates of the same storm. These issues create difficulty in predicting and evaluating wind radius from the global TC warning centers (Cangialosi and Landsea; 2016). Currently, there are a few techniques based on satellite-derived data, numerical weather predictions (NWP), and statistical regression models for real-time estimating and predicting the wind radius, but it is still

challenging, and the number of reliable forecasting tools also remains limited (Knaff et al., 2017).

TC size is known to be related to a number of factors. The relationship between TC maximum wind speed (V_{max}) and R34, which shows a strong positive correlation, has been widely used in operations (Weatherford and Gray, 1988; Chan and Chan, 2012; Song and Klotzbach, 2016). However, the outer wind radius can be shrink at strong V_{max} , and can be extended at weak V_{max} (Kimball and Mulekar, 2004). This implies that knowing the V_{max} is not enough information to determine the TC's wind field structure (Knaff et al., 2014). Latitude is the most frequently used factor for TC size estimations after V_{max} —the higher the latitude, the larger the TC size (Merrill, 1984; DeMaria and Pickle, 1988). Contrastively, Chan and Chan (2014) found that the TC vortex size is not necessarily greater at higher latitudes in the numerical study. The latitude and TC translation speed are key factors affecting not only wind radii but also their asymmetries: the higher the latitude and the faster the TC translation speed (TCTS), the greater the asymmetry (Frank and Gray, 1980; Dougherty and Davis, 2014; Knaff et al., 2016). Storm age is closely related to V_{max} and latitude (Kossin et al., 2007; Knaff et al., 2016; Dolling et al., 2016; Schenkel et al., 2017).

Furthermore, TC size is affected by the various environmental systems. First, synoptic flow patterns are associated with TC size. Liu and Chan (2002) found that TCs can expand as it enters the break of a strong subtropical ridge and westerly flow poleward of the ridge, while can shrink in the dominant region of the strong subtropical region. Initially larger TC generally has a larger size at a later stage (Chan and Chan 2014; Kilroy and Smith 2017; Xu and Wang 2010). Xu and Wang (2010) showed that

TCs with a large initial size lead to the development of spiral rainbands with a large radial extent, and then outward extension of the tangential wind fields by the released latent heat flux in the rainband. In addition, large TC size is related to higher environmental relative humidity (Hill and Lackmann 2009; Wang 2012; Xu and Wang 2010) and sea surface temperature (Chavas et al. 2016; Lin et al. 2015) releases more latent heat flux. More recently, Wang and Toumi (2022) found that the growth of TC outer size is primarily dominated by four factors such as the initial size, growth duration, mean growth latitude, and mean effective inflow angle and highlighted that the inflow angle is a crucial physical variable of TC size growth by linking the effects of internal and external conditions.

This dissertation focuses on key three topics, and contains the introduction, summary, and discussion in each section. In section 2, we compare the estimates of R30 and R50 among the TC agencies over the WNP. In section 3, an operational scheme for predicting the symmetric R30 and R50 of a WNP TC has been developed using a statistical regression method and track pattern clustering, and verified the model performance of a developed statistical model. In section 4, the system for estimating the longest and shortest R30s objectively has been developed based on the wind fields of the Global Forecast System, and tested for applicability of real-time prediction. Finally, this thesis will be concluded in section 5.

2. Comparison of tropical cyclone wind radius estimates between KMA, JMA, and JTWC

This chapter has been published in “Asia-Pacific Journal of Atmosphere Science” by the authors (Kim et al. 2022).

2.1. Introduction

The size of a tropical cyclone (TC), which is directly related to the extent of its damage area, is important information that global TC warning centers provide as part of their TC advisory and warning processes. Global TC warning centers estimate the TC size based on the maximum radial extent of critical wind speed thresholds, such as 30-, 34-, and 50-kt wind radii, from the storm center (hereafter R30, R34, R50, respectively). The TC size is mainly used for wind-based risk and impact assessments, as well as wave and surge forecasting (Knaff et al., 2017). However, studies on the TC size have received little attention compared to studies using other metrics, such as TC track and intensity, despite the importance of the TC size in operational forecasts (Chavas et al., 2015). This is partly because the TC size is usually estimated in a subjective way, which reduces the accuracy and consistency of the data (Landsea and Franklin, 2013; Knaff et al., 2017, Cha et al., 2020), making the study of the TC size difficult. Indeed, although global TC warning centers make significant efforts to produce accurate TC size data, they exhibit significant differences between them (Song and Klotzbach, 2016).

In general, TC wind radii are estimated based on available information using numerical models, statistical wind radius climatology and persistence (CLIPER)

models, and satellite-derived data from various operational agencies (McAdie, 2004; Sampson and Knaff, 2015; Knaff et al., 2016). In particular, satellite winds are primary observation sources for estimating the wind radius by agencies instead of aircraft reconnaissance and surface observations that are not routinely available (Brennan et al., 2009). In U.S. TC warning centers, namely the National Hurricane Center, the Central Pacific Hurricane Center (NHC), and the Joint Typhoon Warning Center (JTWC), numerous scatterometers such as Quick scatterometer (Lungu and Callahan, 2006), WindSat, Oceansat-2, Advanced Scatterometer (ASCAT) (Bentamy et al., 2008), Scatterometer Satellite (Misra et al., 2019) and more recently Haiyang-2 scatterometer (Zhao and Zhao, 2019) are used to postseason subjective and objective reanalysis of wind radii (Sampson et al., 2017, 2018; Knaff et al., 2021). In the Japan Meteorological Agency (JMA), TC parameters including R30 and R50 are determined with overall available observations such as Himawari-8 satellite images, Radar, surface synoptic observations, ship, buoy, and ASCAT. In the absence of necessary observations, the JMA estimates R30 and R50 from regression equation between central pressure and wind radius (Muroi, 2018). In the Korea Meteorological Administration (KMA), the postseason analysis of wind radii is primary based on direct estimates from satellite observations such as ASCAT, Multiplatform Tropical Cyclone Surface Wind Analysis (MTCSWA) (Knaff et al., 2011), and Microwave Radiometers (Hong and Shin, 2013). When these data are not available, the KMA indirectly estimates TC wind radii from the regression between wind radii and maximum wind speed (V_{max}) using the KMA infrared satellite data (Kwon, 2012; Lee and Kwon, 2015). As such, agencies generally use similar data in their postseason

analysis to generate wind radius, but each agency has its own method of estimating TC wind radii, which results in different estimates of the same storm. For instance, Song and Klotzbach (2016) found a considerable discrepancy in wind radius estimates between the JMA and the JTWC due to differences in their detailed estimation techniques.

Understanding such differences in wind radius estimates among agencies is a prerequisite for performing TC size-related studies. The International Best Track Archive for Climate Stewardship (IBTrACS) has been providing TC wind radii since version 4, in which the JMA has provided the longest and shortest R30 and R50, respectively, from 1979 to the present (Knaff et al., 2021). Meanwhile, the JTWC has provided R34 and R50 data from 2001 to the present (Lee et al., 2010). The KMA has also provided postseason reanalysis or best tracking of wind radii, which include the longest and shortest R30 and R50, since 2015 (KMA, 2019). However, how the wind radius estimates of the KMA, JMA, and JTWC differ from each other and whether they have unique characteristics have not yet been evaluated.

The TC size is known to be related to the V_{max} , latitude, TC translation speed (TCTS), and storm age (Merrill, 1984; Weatherford and Gray, 1988; Bell and Ray, 2004; Kimball and Mulekar, 2004; Knaff et al., 2007; Kossin et al., 2007; Wu et al., 2012). Such parameters are used for the development of statistical models, such as the CLIPER model, which is one of the operational models of the NHC and the JTWC (Knaff et al., 2007). In particular, the relationship between V_{max} and R34, which show a strong positive correlation, has been widely used in operations (Weatherford and Gray, 1988; Chan and Chan, 2012; Song and Klotzbach, 2016). Latitude is the most

frequently used factor for TC size estimations after V_{max} —the higher the latitude, the larger the TC size (Merrill, 1984; DeMaria and Pickle, 1988). It has also been reported that fast poleward-moving TCs increase their angular momentum, which is associated with an increase in TC size, suggesting that the TC size can be affected by the TCTS as well as the latitude (Chan and Chan, 2013). The latitude and TCTS are key factors affecting not only wind radii but also their asymmetries: the higher the latitude and the faster the TCTS, the greater the asymmetry (Frank and Gray, 1980; Dougherty and Davis, 2014; Knaff et al., 2016). Storm age is closely related to V_{max} and latitude—as storm age increases, the TC moves to higher latitudes and V_{max} tends to increase (Knaff et al., 2016), resulting in a high correlation between storm age and TC size (Kossin et al., 2007; Dolling et al., 2016; Schenkel et al., 2017). Therefore, it is important to know how each agency considers these TC size–related parameters in its wind radius estimations, as this helps to understand wind radius estimation discrepancies among agencies.

This study aimed to investigate the characteristics of R30, R34, and R50 estimated by three agencies—the KMA, JMA, and JTWC—including their asymmetrical characteristics in terms of V_{max} and spatial distributions. We also aimed to examine how each agency considers TC size–related factors (V_{max} , latitude, TCTS, and storm age) in its TC wind radius estimations by comparing the correlation coefficients between these factors and the TC wind radii. The rest of this chapter is organized as follows. Section 2.2 describes the data and methods used. Section 2.3 presents the results of the comparison of wind radius estimates between the three agencies. Section 2.4 describes how each agency considers the factors affecting the TC size. The final section summarizes the results and concludes the chapter.

2.2. Data and methods

JMA and JTWC best track data from 2015–2018 were obtained from IBTrACS version 4, which includes TC position, intensity, and wind radius information at 6-h intervals. KMA best track data were obtained from the National Typhoon Center of the KMA. For a unified analysis, all wind radius data (R30, R34, and R50) were reconstructed by averaging the longest and shortest radius estimates of the KMA and JMA and four-quadrant wind radii (northeast, southeast, southwest, and northwest) for the JTWC based on KMA information. The R30 data were the 30-kt wind radii used by both the JMA and the KMA based on 10-min mean wind speeds, while the R34 data were the 34-kt wind radii used by the JTWC based on 1-min mean wind speeds. The definition difference in wind speeds between the JMA/KMA and the JTWC can make a direct comparison between R30 and R34 difficult. However, a sensitivity experiment that converted the data to the same wind speed definition showed that the difference had a minor effect. This may be because 34 kts in 1-min mean wind speed intervals is about 30 kts in 10-min mean wind speed intervals when a conversion factor of 1.14 is used (Barcikowska et al., 2012). Therefore, we directly compared R30 and R34 (hereafter, for convenience, the JTWC's R34 is used as R30). Meanwhile, the JTWC's R50 have been analyzed after applying the conversion factor.

The ways in which each agency considers TC size-related factors (V_{max} , latitude, and TCTS) in its TC wind radius estimations were examined by comparing the correlation coefficients between these factors and the estimated TC wind radii. The results were also used to investigate the agency-dependent asymmetrical

characteristics of wind radii. The TCTS was calculated using centered time differencing based on changes in latitude and longitude at 12-h intervals, except for the first and last cases, in which one-sided time differencing was used (Xu and Wang, 2018). The asymmetries in wind radii used in this study are consistent with methods suggested by Song and Klotzbach (2016). For the KMA and JMA, the asymmetries were calculated as the differences between the longest and shortest radii of the TCs divided by 2. Meanwhile, the JTWC are calculated as follows:

$$\text{Asymmetry}_{\text{JTWC}} = \frac{1}{2} \sqrt{(R_{\text{NE}} - R_{\text{SW}})^2 + (R_{\text{SE}} - R_{\text{NW}})^2} \quad (2.1)$$

Here, the terms R_{NE} , R_{SW} , R_{SE} , and R_{NW} indicate wind radii in the northeast, southwest, southeast, and northwest quadrants, respectively.

2.3. Results

2.3.1. Comparison of wind radius estimates between the three agencies

To examine the characteristics of the TC wind radii estimated by the KMA, JMA, and JTWC, the correlations and mean values were first compared between the three agencies. The first observation was that the correlation coefficient (0.75–0.81) of R30 was overall higher than that of R50 (0.57–0.70). This suggests that the agencies have greater difficulty estimating TC wind radii in stronger winds due to the relatively smaller sample and few tools available for radius estimation. The KMA and JMA showed the strongest correlations in R30 and R50 (0.81 and 0.70, respectively; Figure 2.1a, d), while the KMA and JTWC showed the weakest correlations (0.75 and 0.57, respectively; Figure 2.1b, e). The JMA showed strong R30 and R50 correlations with the other two agencies (Figure 2.1a, c, d, and f).

A comparison between the mean values of each agency showed that the JMA had the largest mean value (334 ± 134 km) for R30, followed by the KMA (242 ± 92 km) and the JTWC (216 ± 95 km). The mean R30 value of the JMA was about 91 and 117 km larger than those of the KMA and JTWC, respectively (Table 2.1). The KMA's mean R30 was smaller than that of the JMA but larger than that of the JTWC. For R50, the JMA also had the largest mean value (129 ± 52 km), followed by the JTWC (113 ± 45 km) and the KMA (100 ± 35 km). The KMA's mean value was about 12–29 km smaller than those of the other two agencies.

Table 2.1. Comparison of mean tropical cyclone wind radius values and their standard deviations between the KMA, JMA, and JTWC. “*N*” indicates the number of samples. The parenthetical values represent the difference between KMA and other agencies, and the ratio of the difference to the KMA value.

	KMA	JMA	JTWC
R30 (Num= 1913)	242.3±92.3 km	333.7±133.6 km (-91.4 km, -38%)	216.2±95.4 km (26.1 km, 11%)
R50 (Num= 1081)	100.4±34.5 km	129.3±51.5 km (-28.9 km, -29%)	112.7±45.0 km (-12.3 km, -12%)

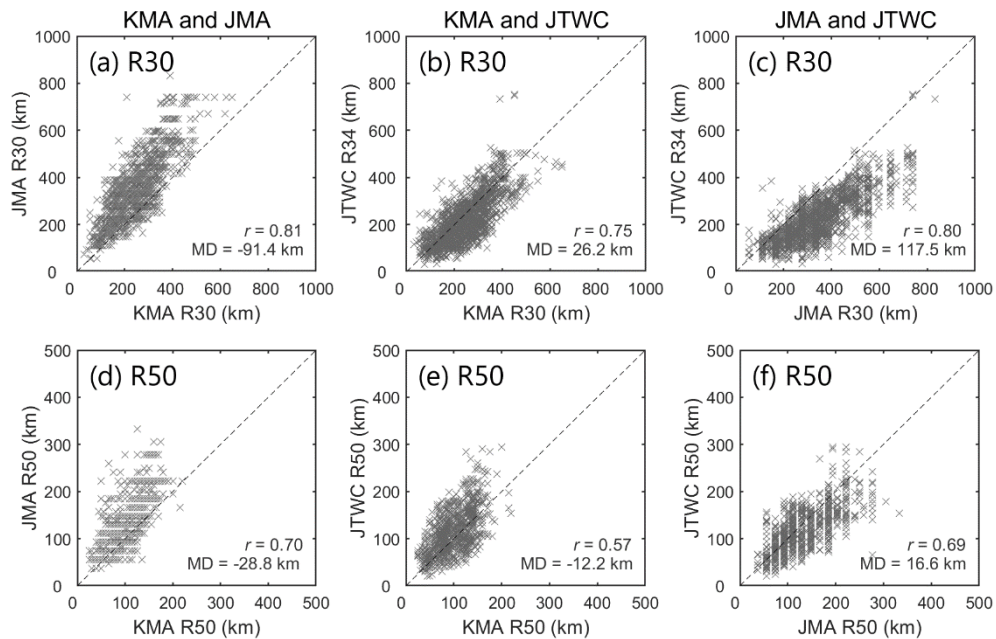


Figure 2.1. Scatter plots of tropical cyclone wind radius estimates of the KMA, JMA, and JTWC. The top (R30) and bottom (R50) panels compare the KMA and JMA (a, d), the KMA and JTWC (b, e), and the JMA and JTWC (c, f). Correlation coefficients (*r*) and mean differences (MD) between the agencies are indicated in the bottom right corner of each panel. The unit of MD is km.

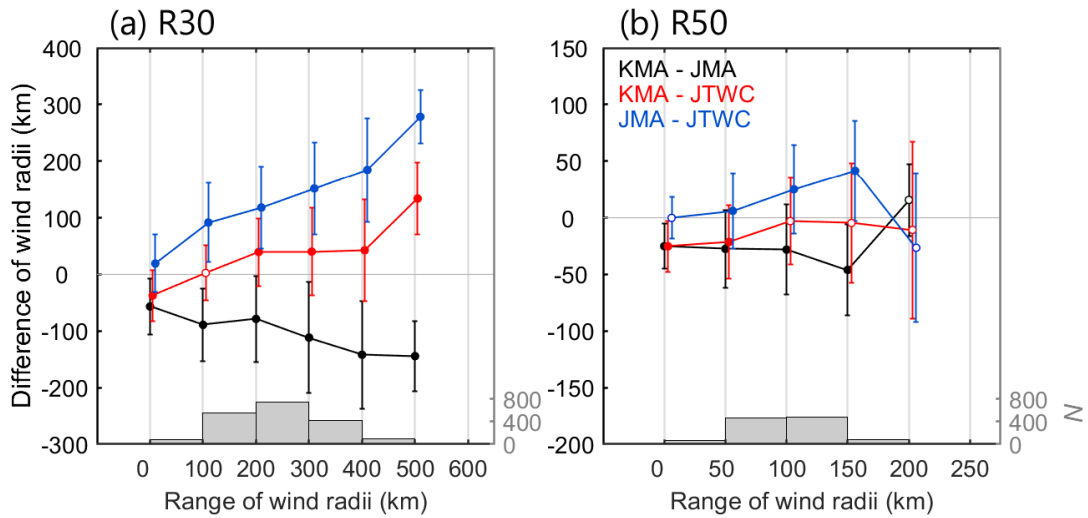


Figure 2.2. Mean differences in wind radius estimates between the KMA and JMA (black), between the KMA and JTWC (red), and between the JMA and JTWC (blue) for each bin of R30 (a) and R50 (b). The bins were divided based on the tropical cyclone wind radius estimates of the KMA. The error bars indicate standard deviations. The gray bar graph represents the numbers (N) of R30 and R50 samples for each bin at 100- and 50-km intervals, respectively. The filled circles indicate significant differences at the 95% level.

To determine the range in which differences in TC wind radii mainly appeared between the agencies, the differences were compared by dividing R30 and R50 into bins at 100- and 50-km intervals, respectively (Figure 2.2). In R30, the difference between the JMA and JTWC showed positive values in all ranges, while the difference between the KMA and JMA had negative values (blue and black lines, respectively, in Figure 2.2a). This suggests that the JMA estimated larger R30 values than the JTWC and KMA in all ranges. The JTWC had larger R30 values than the KMA in wind radii of less than 100 km but smaller values than the KMA in radii of over 200 km. The absolute differences between the agencies increased as the TC wind radii increased.

In R50 (Figure 2.2b), the differences both between the KMA and JMA (black) and between the KMA and JTWC (red) had negative values except over 200 km. This suggests that the KMA estimated smaller R50 values than the JMA and JTWC in most ranges. The JTWC had smaller R50 values than the JMA except over 200 km. Unlike R30, the absolute differences between the agencies did not change significantly as the TC wind radii increased.

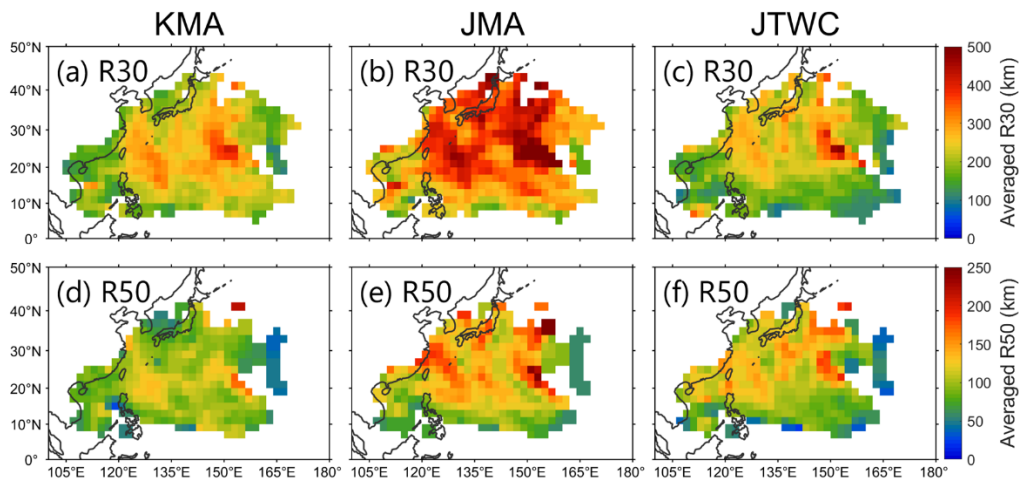


Figure 2.3. Comparisons of the spatial distributions of tropical cyclone R30 (top panels) and R50 (bottom panels) between the KMA (a, d), JMA (b, e), and JTWC (c, f) during 2015–2018. In each grid, the values were averaged along a moving window of 4° by 4° to smooth the wind radius of each grid.

To compare the spatial distributions of estimated TC wind radii between the agencies, the wind radii of all TCs occurring during the study period were averaged for the grid of $2^\circ \times 2^\circ$ using a moving window of 4° by 4° to remove outliers with large spatial variability (Figure 2.3). In R30, all three agencies had larger values than average in the central region of the WNP ($120\text{--}160^\circ\text{E}$, $15\text{--}45^\circ\text{N}$) and relatively small values at low latitudes (below 15°N), the South China Sea, and the inland area of East Asia (Figure 2.3a–c). The difference between the KMA and JMA showed negative values (Figure 2.4a), while the difference between the JMA and JTWC showed positive values (Figure 2.4c). This suggests that the JMA estimated larger R30 values than the JTWC and KMA in most regions. In particular, the JMA had larger R30 values than the other two agencies at higher latitudes. The JTWC had larger R30 values than the KMA in the inland area of China and along the coast of the Korean Peninsula but smaller R30 values than the KMA at latitudes below 20°N (Figure 2.4b).

In R50, the JMA and JTWC showed similar spatial distributions, especially in that they have large values near Japan and Taiwan, but the KMA showed different distributions overall (Figure 2.3d–f). The spatial differences between the agencies showed that the KMA had smaller R50 values than the JMA and JTWC in most regions except low latitudes below 10°N (Figure 2.4d and e). For the JMA and JTWC significant differences were found in the open seas east of 150°E (Figure 2.4f).

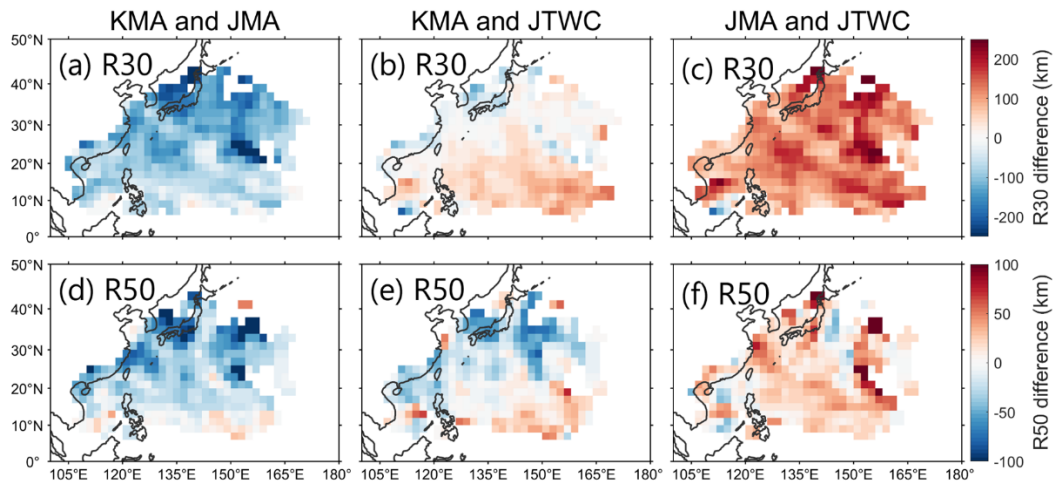


Figure 2.4. Comparisons of the spatial distributions of mean differences in tropical cyclone R30 (top panels) and R50 (bottom panels) between the KMA and JMA (a, d), between the KMA and JTWC (b, e), and between the JMA and JTWC (c, f) during 2015–2018. In each grid, the values were averaged along a moving window of 4° by 4° to smooth the wind radius of each grid.

2.3.2. Relationship between wind radii and potential TC size-related environmental variables

To examine the extent to which the four key parameters related to the TC size (V_{max} , latitude, TCTS, and storm age) affected the three agencies' estimations of TC wind radii, the correlations between the four parameters and the TC wind radii were examined (Table 2.2). The results showed that of the four parameters, V_{max} had the strongest correlations with R30 and R50 overall, with stronger correlations in the KMA (0.61–0.62) estimations than in the estimations of the other two agencies (0.27–0.44). The similarity of the spatial distribution of V_{max} to that of R30 and R50 supports the strong correlation between them (see Figure 2.5a and Figure 2.3).

Latitude did not correlate with wind radii in the KMA estimates (–0.04 to 0.05) but had weak correlations in the JMA and JTWC estimates (0.20–0.28). Similarly, the TCTS showed little correlation with wind radii in the KMA estimates (–0.02 to 0.06) and weak correlations in the JMA and JTWC estimates (0.10–0.19). These results indicate that the KMA mainly consider only V_{max} when estimating TC wind radii (Lee and Kwon, 2015), while the JMA and JTWC additionally consider the latitude and TCTS in addition to V_{max} (Knaff et al., 2007).

Meanwhile, storm age had a significant correlation with wind radii of all agencies (JMA, 0.35~0.37; JTWC, 0.23~0.41; KMA, 0.18~0.37). The high correlations can be explained by the fact that storm age is correlated with V_{max} (0.34~0.43) and latitude (0.40~0.46), respectively. On the other hand, the large difference in wind radii (especially in R50) between the KMA and other agencies in the East Sea and the eastern seas of Japan (Figure 2.3) seems to be due to the influence of TCTS and storm

age, which have large values in the vicinity (Figure 2.5b and c). This is because the KMA considers TCTS and storm age relatively less than other agencies.

Table 2.2. Pearson’s correlation coefficients and their p -values between tropical cyclone wind radii (R30, R50) and tropical cyclone size-related environmental variables (maximum wind speed, latitude, TC translation speed, and storm age) for the three agencies. The units of Vmax, Latitude, TCTS, and Storm age are kt, °N, m s⁻¹ and day, respectively.

TC wind radii		Correlation coefficient		
		KMA	JMA	JTWC
R30	Vmax	0.62 ($p < 0.01$)	0.38 ($p < 0.01$)	0.44 ($p < 0.01$)
	Latitude	0.05 ($p < 0.01$)	0.24 ($p < 0.01$)	0.28 ($p < 0.01$)
	TCTS	0.06 ($p < 0.01$)	0.18 ($p < 0.01$)	0.19 ($p < 0.01$)
	Storm age	0.37 ($p < 0.01$)	0.37 ($p < 0.01$)	0.41 ($p < 0.01$)
R50	Vmax	0.61 ($p < 0.01$)	0.41 ($p < 0.01$)	0.27 ($p < 0.01$)
	Latitude	-0.04 ($p = 0.90$)	0.20 ($p < 0.01$)	0.24 ($p < 0.01$)
	TCTS	-0.02 ($p = 0.26$)	0.10 ($p < 0.01$)	0.17 ($p < 0.01$)
	Storm age	0.18 ($p < 0.01$)	0.35 ($p < 0.01$)	0.23 ($p < 0.01$)

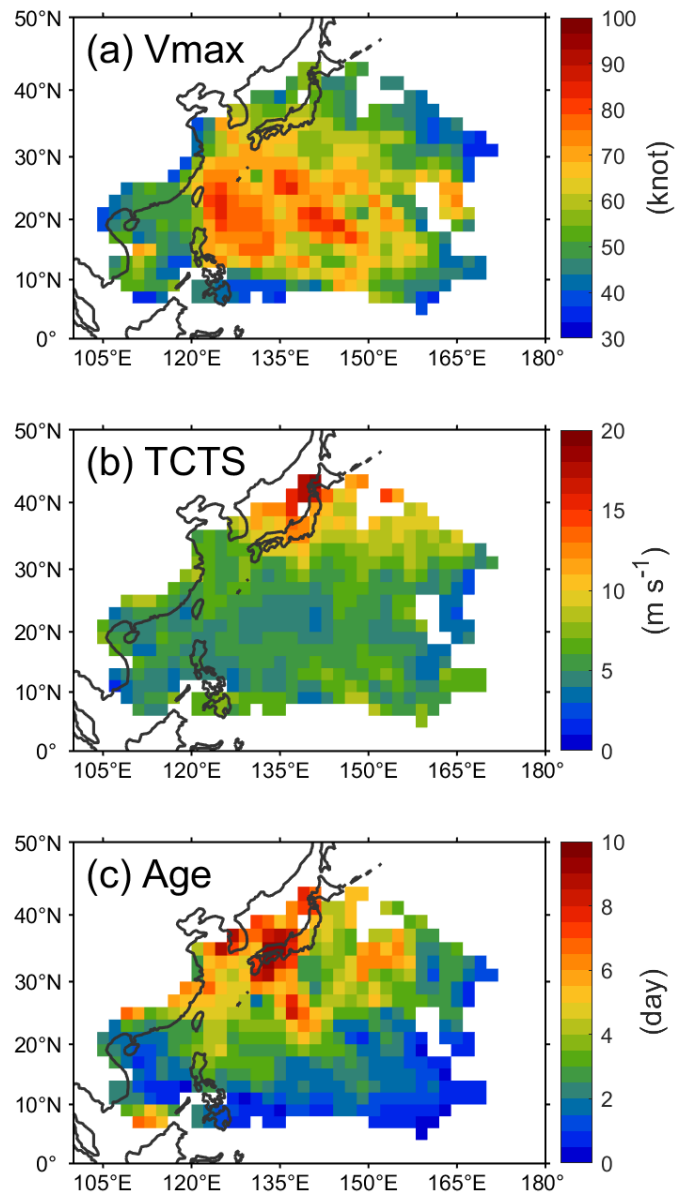


Figure 2.5. Spatial distributions of maximum wind speed (V_{\max}) (a), TC translation speed (TCTS) (b), and storm age (Age) (c) based on the KMA best track data during 2015–2018. In each grid, the values were averaged along a moving window of 4° by 4° for smoothing.

To determine the range in which the wind radius differences between the three agencies were large for V_{max} , latitude, TCTS, and storm age, the mean wind radii and their standard deviations were compared by dividing the parameters into bins at intervals of 10 kts, 5° , 2 m s^{-1} , and 1 day, respectively. The spacing of bins were determined such that the sample size of each bin was sufficient for statistical analysis. In terms of V_{max} (Figure 2.6a and e), R30 and R50 tended to increase as V_{max} increased in all agencies' estimations. Specifically, the JMA had the largest R30 values in all bins, followed by the KMA and JTWC. For R50, the JMA also had the largest values in all bins, followed by the JTWC and KMA. The order, by agency, for R30 and R50 is also generally similar for latitude, TCTS, and storm age (Figure 2.6b–d and f–h).

Regarding latitude (Figure 2.6b and f), R30 and R50 tended to increase as the latitude increased in the JMA and JTWC estimates but did not change significantly in the KMA estimates. These results are consistent with the finding that the TC wind radii in the KMA estimates did not correlate with latitude. Because of this tendency, the KMA's estimates of wind radii at low latitudes were similar to those of other agencies, but the differences gradually increased at higher latitudes. The TCTS trends were similar to the latitude trends (Figure 2.6c and g). This is because the TCTS correlates strongly with latitude, increasing with higher latitudes. For storm age, as it increases, R30 and R50 tended to increase in all agencies (Figure 2.6d and h), which can be explained by the fact that storm age is significantly correlated with both V_{max} and latitude. In particular, for a high storm ages of more than 6 days, it is more similar to the trend of latitude than V_{max} .

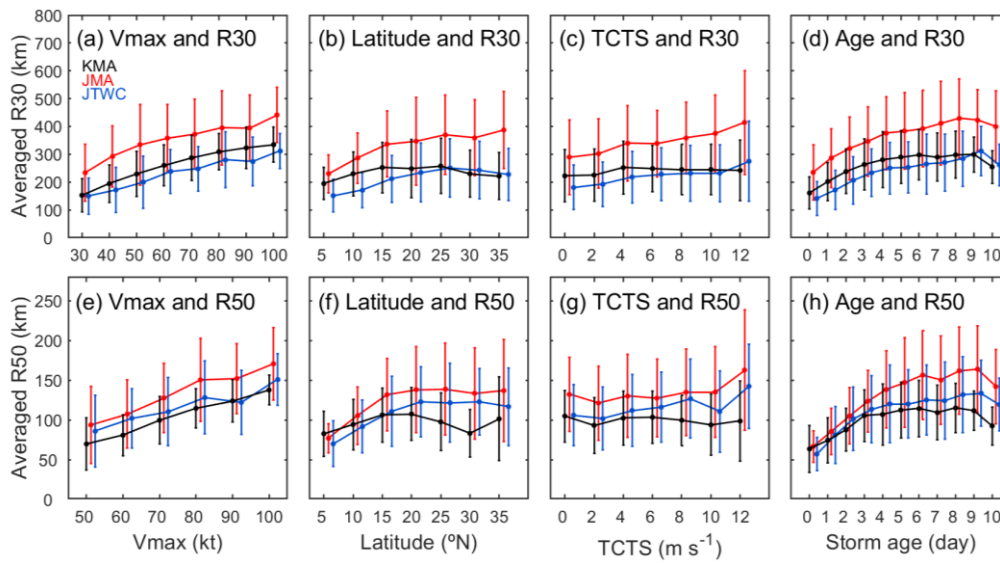


Figure 2.6. Comparison of the mean values (circles) and standard deviations (error bars) in each bin of maximum wind speed (Vmax) (a, e), latitude (b, f), TC translation speed (TCTS) (c, g), and storm age (Age) (d, h) for R30 (top panels) and R50 (bottom panels) estimates of the KMA (black), JMA (red), and JTWC (blue). The bins are divided into intervals of 10 kts, 5°N, 2 m s⁻¹, and 1 day for Vmax, latitude, TCTS, and storm age, respectively.

2.3.3. Asymmetrical characteristics

The asymmetries in wind radii estimated by the three agencies were investigated, and the ways in which they were related to V_{max} , latitude, TCTS, and storm age in each agency's estimations were specifically examined. First, a comparison of the mean R30 asymmetry values between the agencies showed that the KMA had the smallest value (29.7 km), followed by the JTWC (43.6 km) and JMA (48.6 km) (Table 2.3). For the normalized asymmetries, the order was changed—the smallest KMA (0.14) and JMA (0.14), followed by JTWC (0.21). In terms of the spatial distributions of the asymmetries (Figure 2.7a–c), the KMA showed uniform distributions with relatively small values (20–40 km) in most regions, while the JMA and JTWC showed significant regional variations, with large (small) values in the eastern seas of Japan and near the KP (South China seas and tropical seas). The regional differences in the estimated asymmetries between the agencies depended on how each agency considered the factors affecting them. A comparison of the mean R30 asymmetries related to V_{max} , latitude, TCTS, and storm age in each agency's estimations is shown in Figure 2.8a–d. The JMA and JTWC showed a tendency toward increased asymmetries as the latitude and STS increased, whereas the KMA estimates did not depend on the latitude or the TCTS.

Table 2.3. Same as in Table 2.1, but for mean asymmetry of tropical cyclone wind radii. Normalized values are shown in parentheses

Mean Asymmetry	KMA	JMA	JTWC
R30	29.7±10.8 km	48.6±47.3 km	43.6±31.1 km
(Normalized)	(0.14±0.06)	(0.14±0.13)	(0.21±0.15)
R50	11.5±5.7 km	4.7±13.3 km	21.5±15.7 km
(Normalized)	(0.13±0.07)	(0.04±0.09)	(0.19±0.12)

For R50's asymmetry, mean and normalized values were the smallest in the KP (4.7 km and 0.04) and the greatest in the JTWC (21.5 km and 0.19) (Table 2.3). In normalized comparisons, the JTWC estimates show, on average, the greatest asymmetries for both R30 and R50. On the other hand, the KP showed almost zero asymmetries for R50 in most regions, except for the eastern seas of Japan (Figure 2.7b and e), while the KMA and JTWC showed similar patterns in the spatial distributions of R30 and R50 (Figure 2.7a, c, d, and f). This suggests that the KMA and JTWC used similar techniques for R30 and R50 estimations, whereas the JMA seems to have used a different method for each.

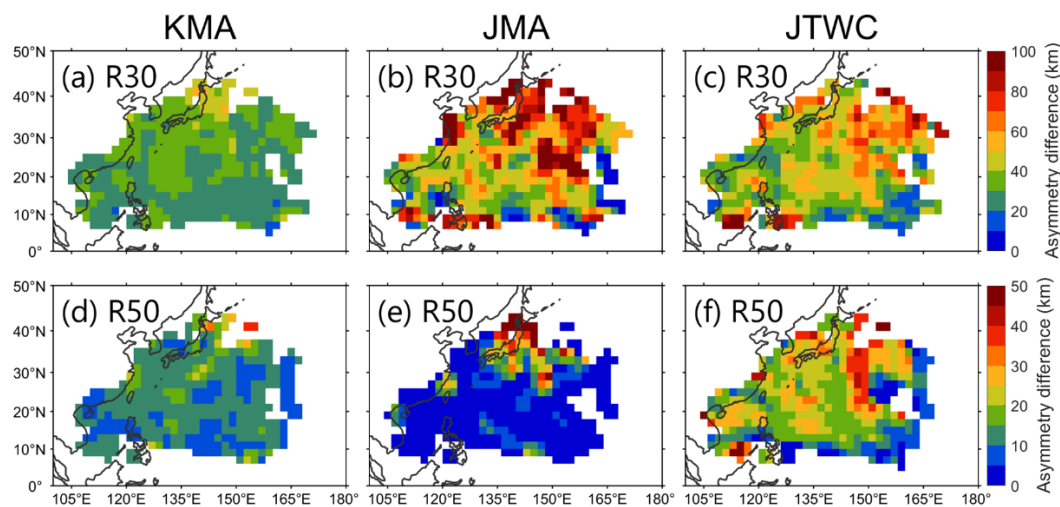


Figure 2.7. Same as in Figure 2.3, but for mean asymmetry values of tropical cyclone wind radii.

In R50, the JTWC heavily relied on the latitude and TCTS, whereas the KMA hardly relied on these variables (Figure 2.8e–h). The JMA showed constant and weak asymmetries at low latitudes (below 20°) and at slow TCTSs (below 6 m s⁻¹), but the asymmetries tended to increase rapidly at higher latitudes and at faster TCTSs (more than 8 m s⁻¹; Figure 2.8f–g). For storm age, the JTWC and JMA showed a similar pattern of asymmetry increasing with storm age up to 8–9 days, but decreasing thereafter, whereas the KMA did not depend on storm age (Figure 2.8e–h). On the other hand, Vmax did not influence the asymmetries for either R30 or R50 in any agency’s estimations (Figure 2.8a and e).

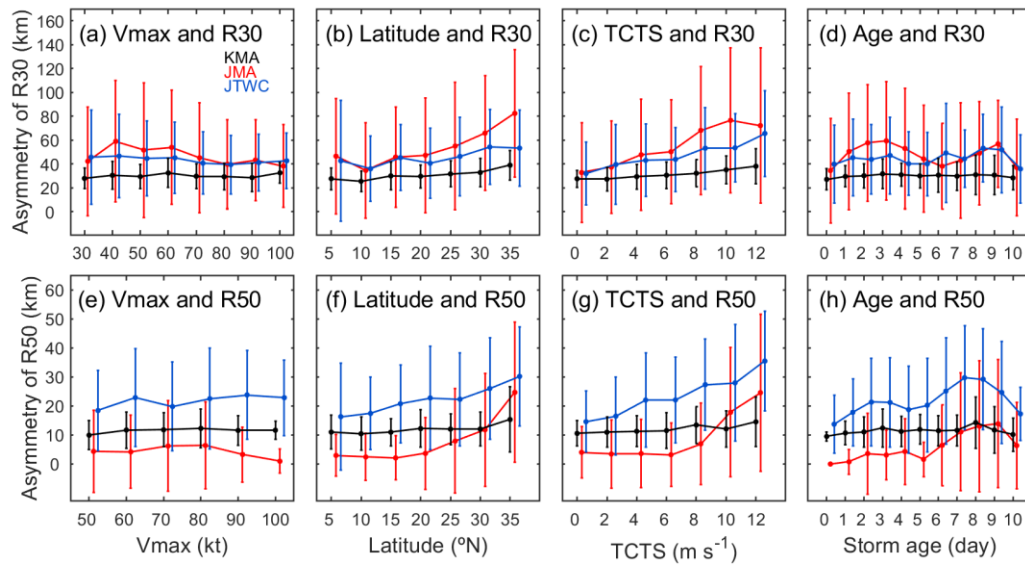


Figure 2.8. Same as in Figure 2.6, but for mean asymmetry values of tropical cyclone wind radii.

2.3.4. Case studies comparing TC wind radius estimates

The TC cases that showed significant differences in mean values and asymmetries in wind radii estimates between the three agencies (reported in the previous section) were selected to investigate the respective wind radius estimation characteristics. The first case was Typhoon Jebi (2018), which showed a large difference in mean R30 between the JMA and the other two agencies (Figures 2.9 and 2.10). Around 00:00 UTC on August 31, when Jebi had the strongest intensity (gray line in Figure 2.9), the mean R30 values of the three agencies were similar. Subsequently, as Jebi weakened, the difference between the JMA and KMA/JTWC gradually increased, reaching over 500 km at the decay stage of the typhoon (12:00 UTC on September 4; red, blue, and green lines in Figure 2.9). Interestingly, the JMA, unlike the KMA and JTWC, estimated a sharp increase in R30 as Jebi rapidly weakened.

To examine why the JMA estimated a significantly larger R30 value than the other two agencies during the rapid weakening stage, we compared the R30 values of the three agencies with a 1000-hPa wind field from the Global Forecast System (GFS) analysis data (Figure 2.10). The model-estimated mean R30 (MM-R30, solid black lines) decreased as Jebi weakened, as in the KMA and JTWC estimates, whereas the model-estimated mean R30 in the top 20% (M20-R30, dashed black line) increased sharply, as in the JMA estimate. In fact, at 18:00 UTC on September 4, when the difference between MM-R30 and M20-R30 was the largest, the radial wind profile of the top 20% was 15 m s^{-1} at two points—A (284 km) and B (786 km) (Figure 2.10). These are candidates that can be estimated to be R30. Interestingly, at this time, KMA and JTWC estimated the value near A as R30 (blue and green dashed line in Figure

2.10) and JMA estimated the value near B as R30 (red dashed line). This suggests that when determining R30, the JMA included a wide area of gale-force winds, far from the TC center, induced by an extratropical transition of the TC, mid-latitude pressure system, and topography.

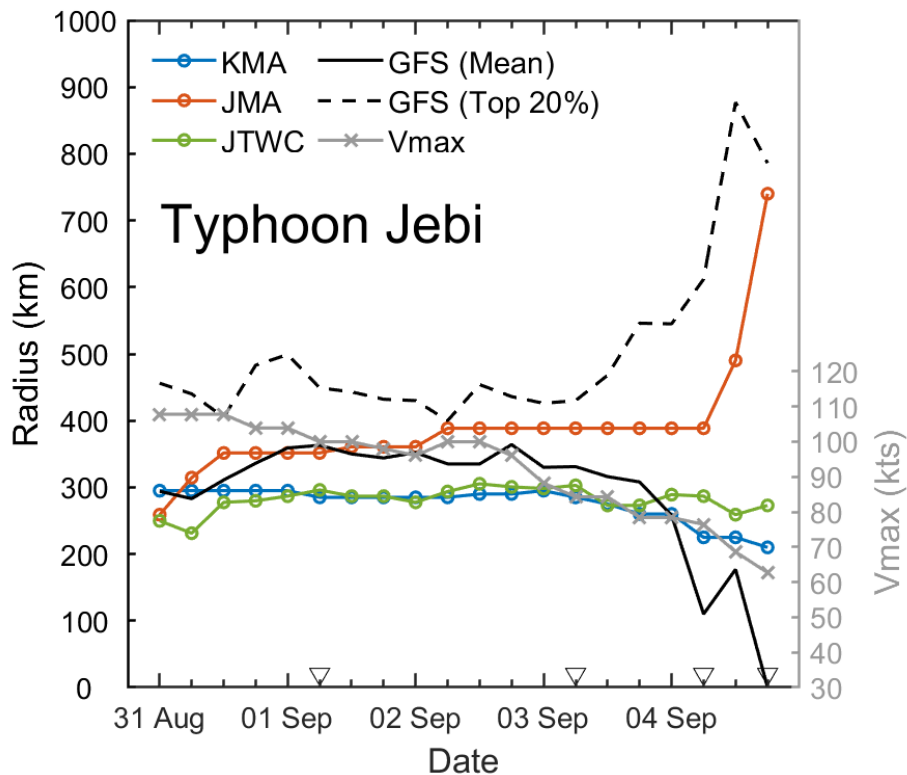


Figure 2.9. Comparison of mean R30 value estimates of the KMA (blue), JMA (red), and JTWC (green) with the mean (solid black line) and top 20% (dashed black line) R30 values estimated from GFS winds at 1000 hPa for Typhoon Jebi (2018) from 00:00 UTC on August 31 to 18:00 UTC on September 12 at 6-h intervals. The solid gray line represents the maximum wind speed (Vmax) estimated by the JMA. The triangles indicate the times of the spatial distributions presented in Figure 2.11.

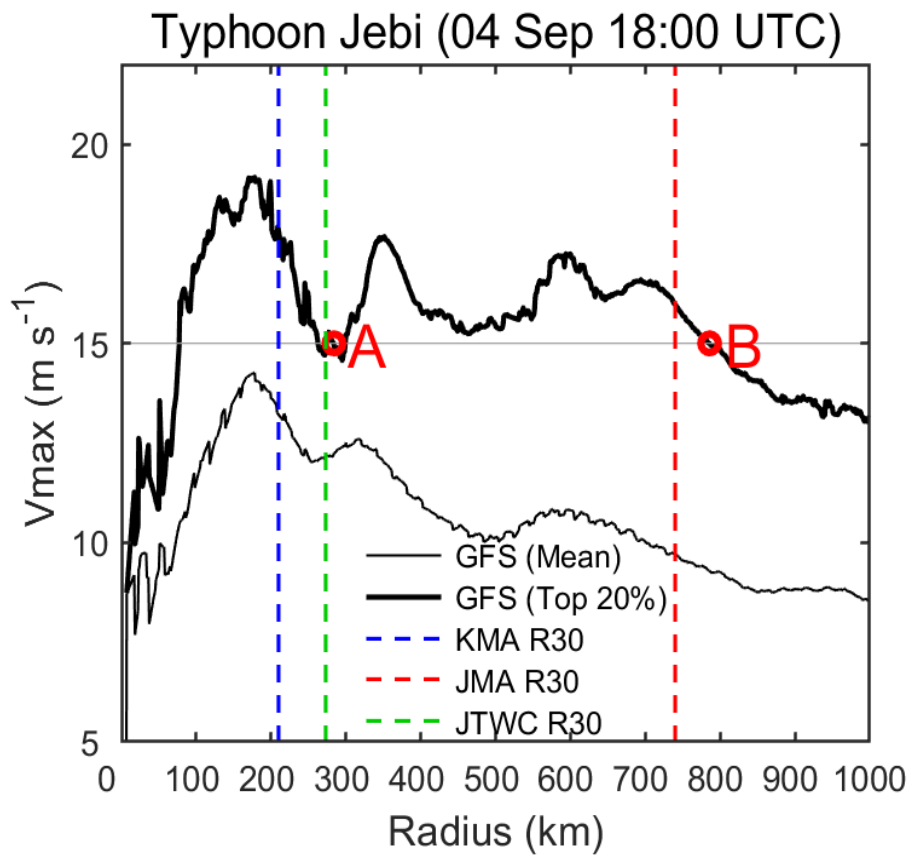


Figure 2.10. Mean radial wind profiles of 1000-hPa GFS wind at 18:00 UTC on September 4 when Typhoon Jebi (2018) rapidly weakened. Thin and thick black lines indicate mean and top-20% mean values, respectively. Blue, red, and green dashed lines indicate R30s estimated from the KMA, JMA, and JTWC, respectively. Points A and B are where V_{\max} is 15 m s^{-1} . At 18:00 UTC on September 4, all mean radial winds (thin black line) were less than 15 m s^{-1} , which explains why the model-estimated mean R30 was zero in Figure 2.9.

This characteristic was evident when the spatial distributions of model winds with R30 were compared between the three agencies (Figure 2.11). At 06:00 UTC on September 1 and 3, when Jebi was in the open ocean, the model's wind field was symmetrical, and the model-estimated R30 was similar to that estimated by the three agencies (Figure 2.11a–b). However, at 06:00 UTC on September 4, when Jebi made landfall in Japan, the strong wind area at the storm center disappeared, and an asymmetrical strong wind region appeared outside the TC, mostly on the ocean side (Figure 2.11c). At 18:00 UTC on September 4, when Jebi weakened further, strong wind regions were distributed from the southern to the northern tip of Japan, far from the TC center (Figure 2.11d), which is related to the low pressures system that existed before Jebi made landfall (Le et al., 2019). At that time, the JMA estimated the R30 to be as large as 740 km, including most of the strong wind region outside the TC, while the KMA and JTWC estimated it to be 210 km and 273 km, respectively, considering only weakened winds near the storm (Figure 2.11d). This is attributed to differences in the three agencies' policies for defining gale–force TC winds. Specifically, the JMA considers the gale–force wind radius to include areas where strong winds occur, even if they are far from the storm's center. On the other hand, the KMA and JTWC seem to determine the gale–force wind radius by focusing on the strong wind area of the TC itself.

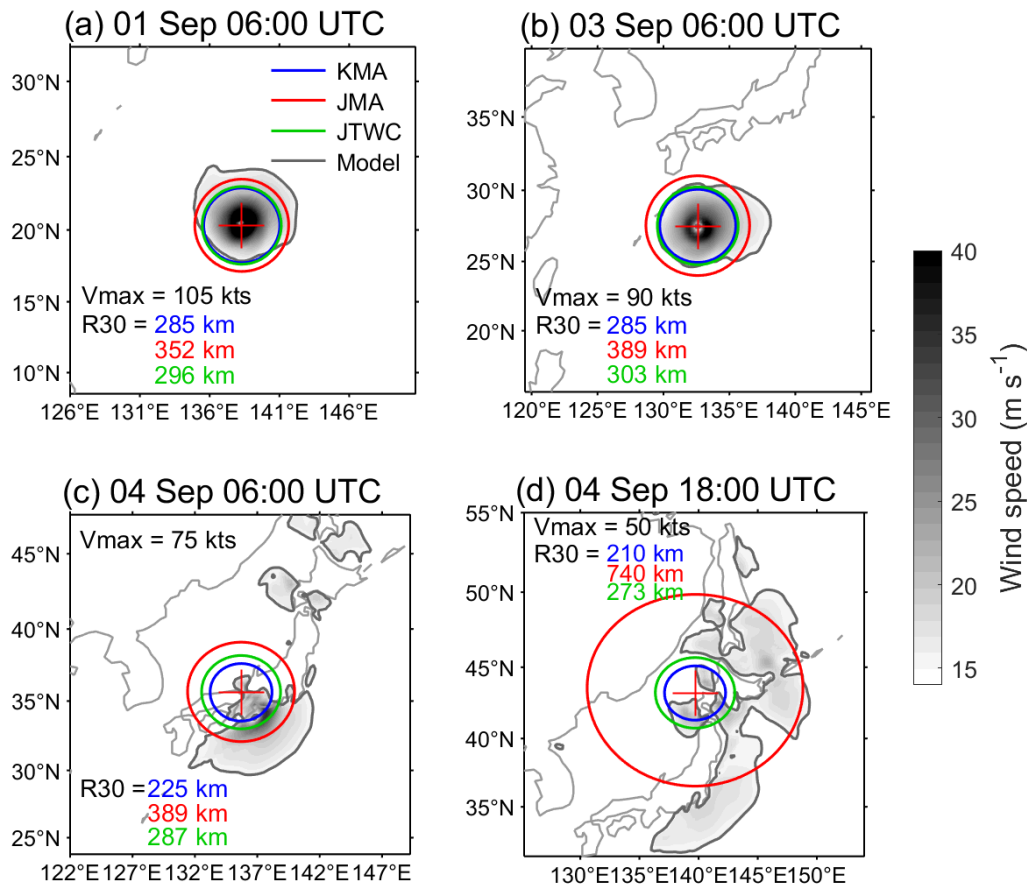


Figure 2.11. Comparison of R30 (gray contour) estimated from the GFS winds (shade) at 1000 hPa with the mean R30 values estimated by the JMA (red circle), KMA (blue circle), and JTWC (green circle) for Typhoon Jebi (2018) at 06:00 UTC on September 1 (a), 06:00 UTC on September 3, 06:00 UTC on September 4 (c), and 18:00 UTC on September 4 (d). The red crosses indicate the tropical cyclone's center. The maximum wind speed (Vmax) estimated by the JMA and the mean R30 values of the three agencies are shown in each panel.

To further explore the characteristics of the asymmetry differences between the three agencies, Typhoon Soulik (2018) was used in another case study. Overall, the KMA showed a small asymmetry (20–40 km) with no significant change over Soulik's lifetime, while the JMA and JTWC showed significant variations (0–83 and 10–90 km,

respectively), similar to the variations in the TCTS (Figure 2.12a and b), with the asymmetry increasing and decreasing as the TCTS increased and decreased. In line with the results obtained from the previously mentioned correlation analysis (Table 2.3; Figure 2.8c), this result suggests that the KMA does not consider the TCTS when estimating wind radii

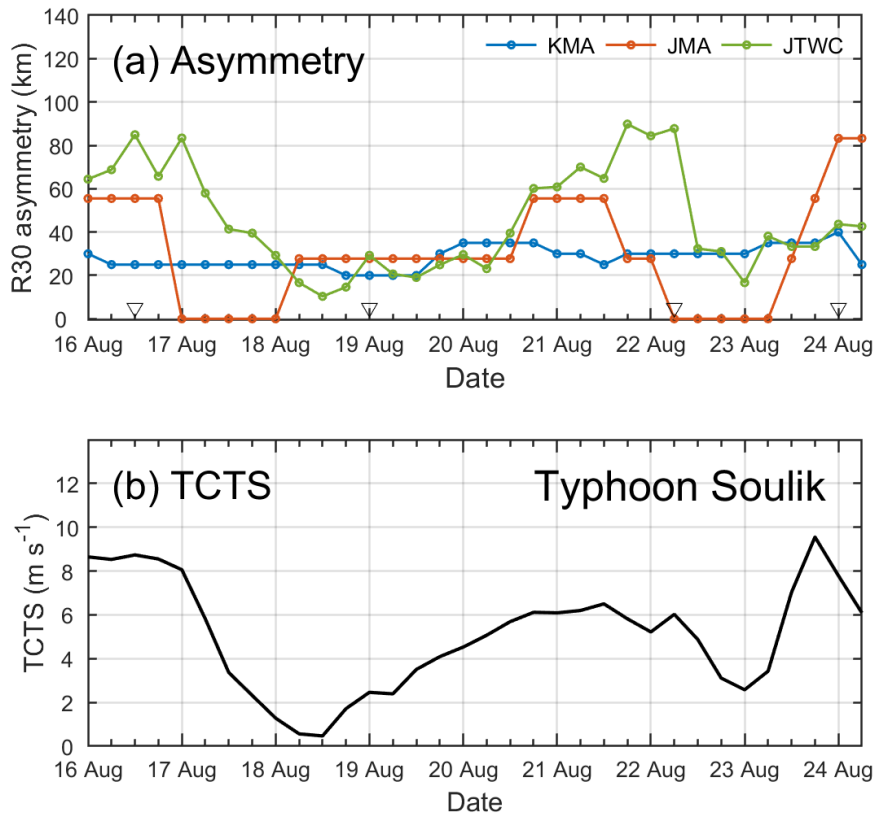


Figure 2.12. Comparison of the R30 asymmetries (a) estimated by the KMA (blue), JMA (red), and JTWC (green) with the TC translation speed (TCTS) (b) for Typhoon Soulik (2018) from 00:00 UTC on August 16 to 06:00 UTC on August 24 at 6-h intervals. The triangles represent the times of the spatial distributions presented in Figure 2.13.

A comparison of the spatial distribution of the model wind with the best-track R30 illustrated the characteristics of the agency-dependent asymmetries (Figure 2.13). First, in the early stages of TC development at 12:00 UTC on August 16 (Figure 2.13a), the model winds showed a clear asymmetrical distribution, which seems to have been related to the relatively fast TCTS (8.7 m s^{-1}). At that time, the JMA and JTWC showed a significant difference between the longest and shortest radii, whereas the KMA showed a relatively small difference (compare the solid and dashed lines or the values in Figure 2.13a). At 00:00 UTC on August 19, when the TC was moving slowly (2.5 m s^{-1}) and increasing in intensity, the model-estimated R30 showed a nearly symmetrical distribution with small differences between the longest and shortest radii in the three agencies' estimates (Figure 2.13b). At 06:00 UTC on August 22, the model wind and JMA's R30 were relatively symmetrical, while those of the KMA and JTWC were asymmetrical (Figure 2.13c). Finally, at 00:00 UTC on August 24, when the TC made landfall over the KP and began to decay, the model wind was particularly asymmetrical (Figure 2.13d), with the gale-force winds more widely distributed outside the northeast than near the TC center. At that time, considering the weakening of the TC, the JTWC and KMA estimated both the longest and shortest radii to be small, while the JMA estimated the longest radius to be very large by including strong wind areas outside the TC, which resulted in a significant asymmetry.

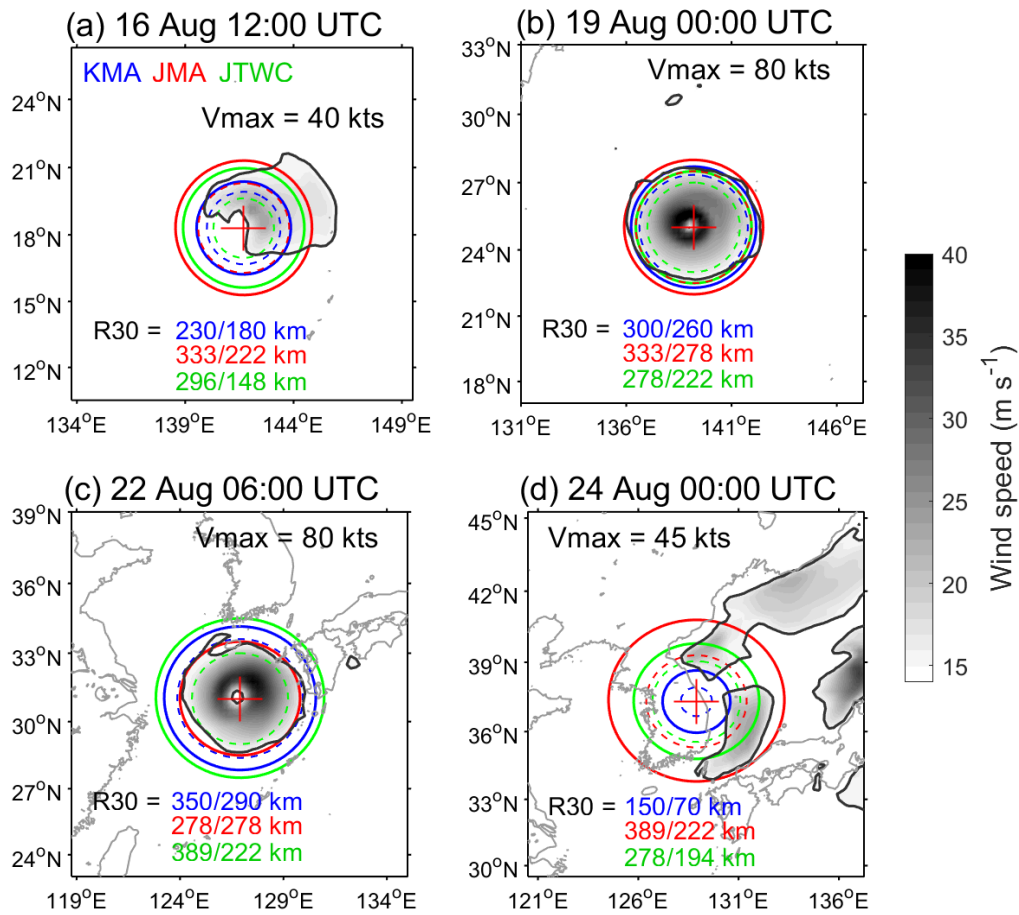


Figure 2.13. Comparison of R30 (gray contours) estimated from the GFS winds (shade) at 1000 hPa with the longest and shortest R30 values estimated by the JMA (red circle), KMA (blue circle), and JTWC (green circle) for Typhoon Soulik (2018) at 12:00 UTC on August 16 (a), 00:00 UTC on August 19 (b), 06:00 UTC on August 22 (c), and 00:00 UTC on August 24 (d). The solid and dashed circles indicate the longest and shortest R30. The red crosses indicate the tropical cyclone's center. The maximum wind speed (V_{max}) estimated by the JMA and the longest and shortest R30 of the three agencies are shown in each panel.

In summary, the KMA considers weak asymmetries—greater than the JMA estimates and smaller than the JTWC estimates—which do not change significantly during the lifetimes of TCs. The JTWC estimates the wind radius, on average, most asymmetrically, with significant variations according to the latitude and TCTS. The JMA tends to estimate the wind radius completely symmetrically before TCs approach higher latitudes (around 20°N) and highly asymmetrically thereafter. Again, this is because the JMA estimates gale-force wind radii, including areas where strong winds occur, even if they are far from the storm's center.

2.4. Summary and discussion

TC wind radii, which constitute some of the most important information for predicting disasters caused by TCs, have been provided by the KMA, JMA, and JTWC since 2015. However, the detailed characteristics of the wind radii estimated by each agency have hitherto not been investigated. This study compared the mean values and asymmetries in the three data sets of TC wind radii (R30 and R50) in the western North Pacific between 2015 and 2018 and explored the factors that each agency mainly considers when estimating wind radii.

First, a comparison between the mean values both R30 and R50 of the three agencies showed that the JMA had the largest mean value—about 91 and 118 km for R30 (about 29 and 17 km for R50) larger than the mean values of the KMA and JTWC, respectively (Table 2.1). The differences increased as the mean wind radii and latitude increased (Figure 2.2; Figure 2.6b and f). A correlation analysis revealed that the KMA considered only V_{max} when estimating TC wind radii, while the JMA and JTWC considered not only V_{max} but also the latitude and TCTS partially (Table 2.2).

Differences in wind radius between the three agencies were also found in the estimated asymmetries, defined as the differences between the longest and shortest wind radii (Table 2.3). The KMA showed the smallest mean asymmetry (29.7 km) for R30, which was uniformly distributed within 20–40 km in most regions. The JMA and JTWC showed greater mean asymmetries (48.6 and 43.6 km, respectively) than the KMA, with considerable regional variations. The mean asymmetry for R50 was smallest in the JMA estimates (4.7 km) and greatest in the JTWC estimates (21.5 km).

The asymmetries in the JMA and JTWC estimates tended to increase with the latitude and TCTS, whereas the KMA did not rely on these parameters, thus estimating locally uniform wind radii.

Through two case studies (Typhoons Jebi and Soulik in 2018), we confirmed the different characteristics of the wind radius estimations of the three agencies. When determining R30, JMA includes a wide area of gale-force winds, far from the TC center, induced by an extratropical transition of the TC, mid-latitude pressure system, and topography. This increases the estimated longest wind radius, especially at higher latitudes (above 20°N), which in turn increases the mean wind radius and asymmetry in the JMA data. On the other hand, the KMA and JTWC generally estimate the TC wind radius by focusing on the strong wind area of the TC itself, which explains why their mean R30 and asymmetries are on average smaller than those of the JMA.

This study provides quantitative information on the characteristics of and differences in gale-force and storm-force wind radii between the three agencies. We found that the wind radii in best track data differ significantly between the three agencies not only in mean values but also in asymmetrical characteristics and spatial distributions. These differences are primarily due to agency-specific policies defining the wind radius and determining whether the estimations should focus on the TC itself or include the wind outside the TC for damage and disaster prevention purposes. At this point, it is impossible to conclude which policy is the best or which wind radius estimation method is the most reliable because each agency's policy has been established for its own purposes. However, it is clear that due to these policy differences, the TC radius data are too uncertain and inconsistent to be used in research,

although previous studies have found that the wind radii in best track data constitute sufficiently reliable information (Knaff et al., 2016; Dolling et al., 2016). Therefore, it is essential for researchers to know in advance the characteristics of the wind radius estimations of each agency and to select and use the data according to each study's purpose. This study provides useful information for making the appropriate selection. The results can also be used as the basis for developing a method for consistent wind radius estimations by various agencies.

3. Tropical cyclone wind radius prediction based on a statistical-dynamical approach and track pattern clustering

3.1. Introduction

Tropical cyclones (TCs) are one of the most devastating natural disasters over the western North Pacific (WNP). To prevent the TC-induced disasters, TC agencies and researchers are making their efforts to improve the TC prediction skill based on available dataset and advanced technologies. Various studies have been conducted so far to improve the accuracy of predicting the TC track and intensity (Powell and Reinhold, 2007; Houston et al., 1999; Irish et al., 2008), but relatively little research has been done on the TC size in terms of the maximum radial extent of strong TC winds, which is an important factor in determining the possible TC-induced damage area (Quiring et al., 2014). In particular, since TC-induced storm surges and ocean waves increase as TCs grow larger (Powell and Reinhold, 2007; Irish et al., 2008; Sampson et al., 2010), the TC sizes is also important information for storm surge and wave forecasting. However, due to the lack of observation data available for estimating the TC size (Dolling et al., 2016), the uncertainty of TC size data is large (Landsea and Franklin, 2013), and even for the same TC, the best-track data show different values depending on the TC agency (Landsea and Franklin, 2013; Song and Klotzbach, 2016; Kim et al., 2022) which makes accurate TC size predictions more difficult (Knaff and Harper, 2010; Cangialosi and Landsea, 2016).

Global TC warning centers routinely publish the TC advisories, including forecast of wind radius of active TCs within their areas of responsibility (Dolling et

al., 2016). For example, U.S TC agencies—the National Hurricane Center (NHC), the Central Pacific Hurricane Center, and the Joint Typhoon Warning Center (JTWC)—provides the forecasts for maximum radial extent of critical wind speed thresholds such as 34-, 50-, and 64-kt winds based on 1-min maximum sustained winds (hereafter referred to as R34, R50, and R64, respectively) in four quadrants (northeast, southeast, southwest, and northwest quadrants) from storm heading. The NHC, which administers the hurricanes over the North Atlantic and Eastern Pacific, started providing 24-h predictions for R50 in 1958, and then began forecasts for R34 and R50 more than the 72-h forecast times since 2001 (Knaff et al., 2021). For the JTWC, which covers the remaining Southern Hemisphere, Indian Ocean, and WNP, the R34, R50, and R64 forecasts have been extended to 120 h after 2016 (Sampson et al., 2018).

Operational skills for TC wind radii prediction have been developed based on available data including satellite-derived winds, numerical weather predictions (NWP), statistical model results, and consensus forecasts. In particular, the statistical-based models have been widely used operational TC centers to overcome the large prediction error of the wind radius, which is common in NWP after a 48-h lead time. Knaff et al. (2007) has been developed a statistical model based on a simple linear regression using three available climatology and persistence predictors (latitude, storm translation speed, and storm maximum winds) for the first time. Recently, the model updated the regression coefficients of predictors used in WNP TCs (Knaff et al., 2018). The updated statistical model showed an initial error of about 20 n mi (1 n mi = 1.85 km), and a prediction error of 26 and 38 n mi at the 24-h and 120-h lead times, respectively, in the WNP. On the other hands, Knaff et al. (2017) developed a global statistical-

dynamical TC wind radii forecast scheme based on TC size proxy estimated from satellite-derived 850-hPa tangential winds and 13 predictors calculated from global NWP model results with a concept similar to the Statistical Hurricane Intensity Prediction Scheme (SHIPS). The statistic-dynamical model used a new consensus technique based on the results of three NWP models, leading to better performance than the general statistical prediction model using individual NWP results (Sampson et al., 2018).

Previous studies have demonstrated that the seasonal TC predictions (Kim et al., 2012) and intensity predictions (Kim et al., 2018) can be improved by using a track pattern clustering method because the factors affecting the TC genesis and intensity differ depending on the TC tracks (Camargo et al., 2007a,b; Chu et al., 2010; Chu and Zhao, 2011; Kim et al., 2011). However, the clustering technique has not been applied for TC size prediction so far. Song et al. (2020) investigated the changes in TC intensity and R30 according to the two TC track types—recurving and straight-moving TCs—in the WNP and found that the interaction between the mid-latitude circulations leading to the baroclinic expansion may increase the size for recurving TCs. This suggests that the TC size may have different characteristics depending on the track pattern, like other TC metrics (genesis frequency and intensity), and that a clustered model may help to improve the performance of TC size prediction.

This study aims to develop an operational scheme for predicting the symmetric R30 and R50 of WNP TCs based on a statistical-dynamical approach using 11 environmental predictors estimated from dynamical results and a track pattern clustering method. In particular, this study examines the effect of track pattern

clustering on TC size prediction by comparing the results of clustered and non-clustered models. Section 3.2 describes the data, predictors, and dependent variable used in this study and how to construct the statistical-dynamical model. Section 3.3 explains the effects of clustering, the characteristics of classified clusters, and selected smart predictors. Section 3.4 indicates the model performance during the training and testing periods, and real-time predictions of developed model and case studies in 2017 and 2018 TCs. Section 3.5 presents model performance for training, testing, and real-time predictions. The final section provides the summary and discussion in this study.

3.2. Data and methods

3.2.1. Data

A total of two types of TC information are used for training the model and real-time prediction. To build the present statistical-dynamical model during the training (2008-2016) and testing periods (2017-2018), the TC size information is obtained from Japan Meteorological Agency (JMA). The data provides latitude, longitude, 10-min maximum sustained surface winds, central pressure, and longest and shortest axis of R30 and R50 at 6-hourly intervals. TC tracks are reconstructed at 5-day intervals, resulting in a total of 3574 (1050) for R30 and 1934 (488) for R50 in training (testing) cases, respectively. For real-time prediction, predicted 5-day track data were obtained from the Korea Meteorological Administration (KMA) during 2017-2018.

Global Forecast System (GFS) analysis datasets are used to calculate the dependent variable and atmospheric potential predictors for training and testing period. The data is provided in six-hourly intervals at $0.5^{\circ} \times 0.5^{\circ}$ horizontal resolutions by the National Centers for Environmental Prediction (NCEP) since 2008. For real-time prediction tests in 2017 and 2018, atmospheric predictors were calculated using GFS forecasts with $0.25^{\circ} \times 0.25^{\circ}$ resolution. Sea surface temperature (SST) is obtained from the Hybrid Coordinate Ocean Model (HyCOM) and Navy Coupled Ocean Data Assimilation (NCODA) nowcast/forecast system with daily 0.08° horizontal resolution and is used for calculating oceanic predictors.

3.2.2. Calculation of dependent variable and predictors

Knaff et al. (2014) have been developed a new proxy for the TC size using the azimuthally averaged 850-hPa tangential wind at the radius of 500 km (V500) instead of the traditional metrics of the radius of the outermost closed isobar (ROCI) or R34. Here, the 5-kt tangential wind at 850 hPa is assumed to be essentially the same as the background flow and defined as R5, which is the radius where the TC wind field is indistinguishable from the background flow in a climatological environment. The climatological R5 used in our model is defined as follows:

$$R5 = \overline{R5} + \alpha \left(\frac{V500 - V500c}{V500c - V1000c} \right) \quad (3.1)$$

where $\alpha = 4.5^\circ$ latitude, $\overline{R5} = 8.6^\circ$ latitude, the climatological values of tangential wind at 500 and 1000km radius is $V500c = 5.05 \text{ m s}^{-1}$ and $V1000c = 2.23 \text{ m s}^{-1}$. The unit of R5 calculated from Equation (3.1) is degrees latitude (1 degrees latitude = 111.11 km). In the present statistical regression model, the dependent variable is defined as the change in R5 ($\Delta R5$) relative to the initial time.

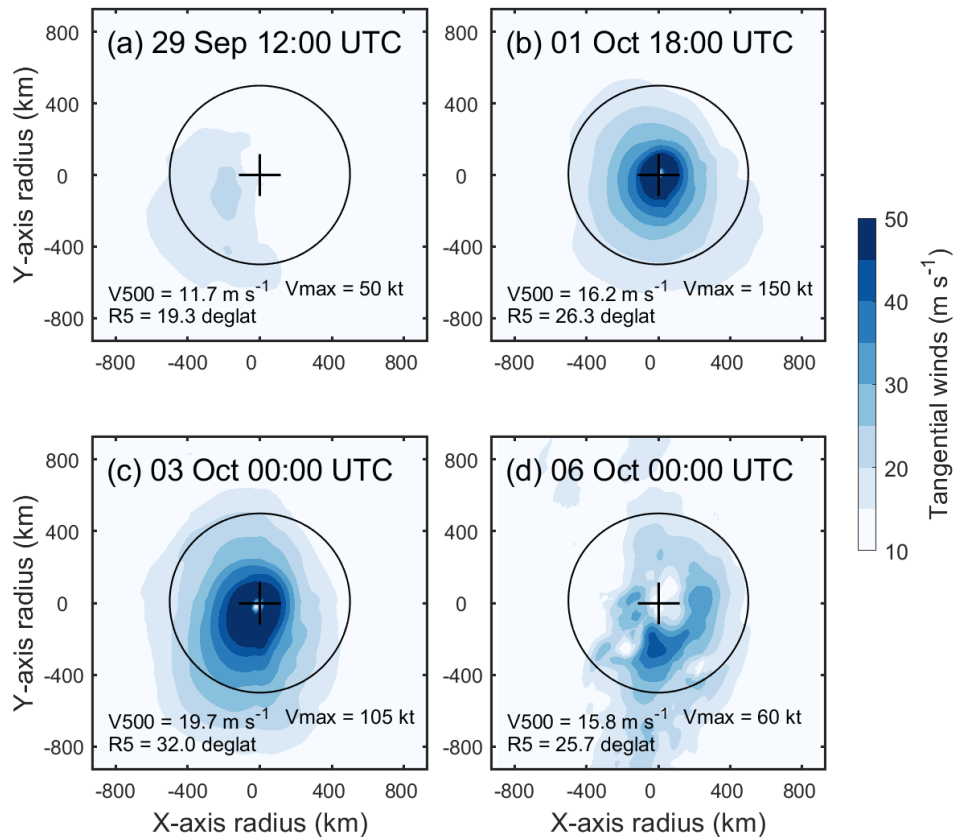


Figure 3.1. Tangential winds estimated from the GFS analysis winds (shade, m s^{-1}) at 850 hPa for Typhoon Trami (2018) at 12:00 UTC on September 29 (a), 18:00 UTC on October 1 (b), 00:00 UTC on October 3 (c), and 00:00 UTC on October 6 (d). The solid circles indicate the 500 km radius from the storm center (black cross) for calculating V500 and R5 (right corner in each panel). The maximum wind speed (Vmax) from JMA best track is shown in the bottom left corner of each panel, respectively.

For example, the tangential wind distributions at the four periods (on September 29 at 12 UTC, on October 1 at 18 UTC, on October 3 at 00 UTC, and on October 6 at 00 UTC) of Typhoon Trami (2018) and their V500 and R5 calculated from Equation (3.1) are shown in Figure 3.1. In general, the calculated V500 and R5 revealed different results depending on the TC structure rather than the Vmax. On October 1 at 18 UTC, which capture an asymmetric structure with relatively strong intensity (105 knots), had

the largest TC size-related parameters, by about 20 m s^{-1} for V500 and 32 degrees latitude for R5 (Figure 3.1c). Meanwhile, the V500 and R5 have similar values in the two periods with different characteristics: the periods with a relatively symmetric structure and strongest Vmax during Trami's lifetime (on October 1 at 18 UTC, Figure 3.1b), the period with the violent asymmetry during the decaying TC stage (on October 6 at 00 UTC, Figure 3.1d). If the TC is weak and accompanied by an incomplete structure, V500 and R5 had significantly smaller values (Figure 3.1a).

Eleven potential predictors are used for the model development (Table 3.1). Most of the potential predictors, including static and environmental variables, were generally selected by Knaff et al. (2017). First, initial R5 (iSIZE) is estimated as Equation (3.1). Three static predictors, such as current intensity (VM), intensity change within 12h (DVMX), and sine latitude of TC (LAT), are extracted from track information. Next, the three oceanic predictors are estimated at the location of the TC's center. Potential intensity (PI) is defined with the SST-based empirical equations (DeMaria and Kaplan, 1994; Whitney and Hobgood; 1997) as introduced in Equation (3.2).

$$PI = A + Be^{(T-T_0)} \quad (3.2)$$

where T and T₀ denote the SST (°C) and specified reference SST (30°C), respectively. Constant coefficients are given by A=19.7 kt, B=88.0 kt, and C=0.1909 in the WNP (Knaff et al., 2017). Relative SST (RSST) is defined as regional SST minus tropical mean SST (30°N-30°S) (Lin et al., 2015). RSST in the tropics is purported to covary closely with local mid-tropospheric environmental relative humidity (RH) (Stephens 1990; Emanuel et al. 1994).

Table 3.1. List of static and synoptic potential predictors used in the present statistical-dynamical model.

Number	Predictors	Description
1	iSIZE	Initial R5 (degree latitudes)
2	VM	Current TC intensity (kt)
3	DVMX	12-h change in intensity
4	LAT	Sine of latitude at the TC location
5	SST	Sea surface temperature at the TC location (°C)
6	RSST	Relative SST at the TC location (Lin et al., 2015)
7	PI	Potential intensity based on empirical equation at the TC location
8	RH	Area-averaged (200-800 km) relative humidity at 500-700 hPa
9	VWS	Area-averaged (0-500 km) 200-850 hPa vertical wind shear
10	D200	Area-averaged (0-1000 km) divergence at 200 hPa
11	RV850	Area-averaged (0-1000 km) relative vorticity at 850 hPa

Four atmospheric predictors are used in the present model: RH in the middle layer (500 and 700 hPa) of the atmosphere, divergence at 200 hPa (D200), relative vorticity at 850 hPa (RV850), and vertical wind shear (VWS) between 200 and 850 hPa (Table 3.1). RH is calculated as an averaged value between 200 and 800km from the storm center, in which doughnut-shape averaging is used to remove the TC effects included in the dataset. D200, RV850, and VWS are calculated as u- and v- component winds and averaged within a 1000-km radius for D200 and RV850 and 500 km for VWS from the storm center.

3.2.3. Clustering method and its effect

Considering the selection of the predictor pool of TCs with locally similar tracks, we carried out track pattern clustering (TPC) and examined the clustering effects on improving the TC size prediction. A fuzzy c -means clustering method (FCM) (Bezdek, 1981) was used to classify TC tracks at 5-day intervals (Kim et al. 2011). The track input used here is uniformly interpolated to 21 latitude and longitude points, respectively.

The FCM is the most popular algorithm in the fuzzy cluster theory, which suggests the possibility that an observation value (x_i) belongs to any group (c_j). This study calculates track membership coefficients (w_{ij}), indicating the possibility that each typhoon (x_i) belongs to a classified cluster (c_j) (Equation (3.3)). The calculation of w_{ij} is determined by the partial derivative of the existing method for the sum of squared error (SSE, Equation (3.4)) in fuzzy clusters given by the following:

$$w_{ij} = \frac{1}{\sum_{k=1}^c \left(\frac{\|x_i - c_j\|}{\|x_i - c_k\|} \right)^{\frac{2}{m-1}}} \quad (3.3)$$

$$SSE = \sum_{i=1}^n \sum_{j=1}^c w_{ij}^m \|x_i - c_j\|^2 \quad (3.4)$$

where $\|x_i - c_j\|^2$ is the distance between each TC track and mean track for each cluster.

Additionally, this study investigates the optimal number of clusters based on three representative measures of scalar validity such as partition coefficient (PC), Xie-Beni index (XB), and the Dunn index (DI) (Figure 3.2). The PC measures the final partitioned cluster using a fuzzy partition matrix, and a larger value indicates the best

partitioning values. (Figure 3.2a). Considering the membership coefficient and the structure of datasets, Xie and Beni proposed the XB index to measure the overall average compactness and separateness, and the smaller its value, the better the partition result (Figure 3.2b). Finally, the DI index has calculated the ratio of inter-cluster and intra-cluster relationships, the larger value means the best number of clusters (Yeh et al., 2013, Figure 3.2c). The PC and XB indices were chosen as a too small or large number of clusters, by 2 and 7 clusters, respectively. We classified the clusters into four groups according to the results of the DI index (Figure 3.2c).

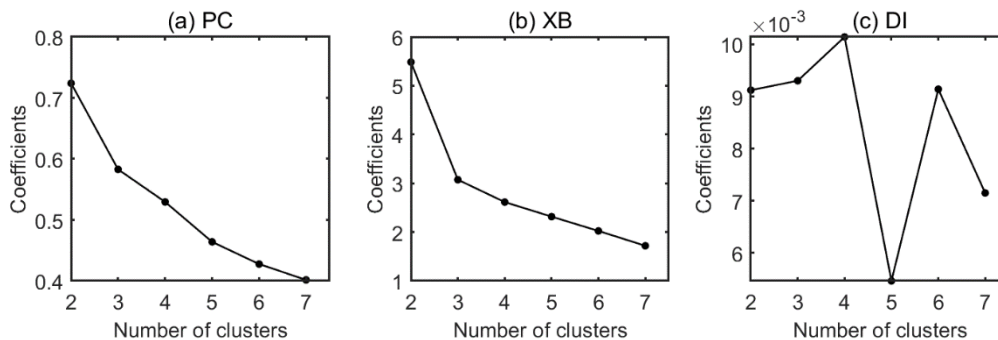


Figure 3.2. Value of three scalar validity measures according to the number of clusters. (a) Partition coefficient (PC), (b) Xie and Beni's index (XB), and (c) alternative Dunn index (DI).

To examine the clustering effect on TC size prediction, we evaluated quantitatively reduction rates of the standard deviation of the $\Delta R5$ before (σ_{all} , Equation (3.5)) and after the use of clustering (σ_c , Equation (3.6)) for each cluster and at 24-, 48-, 72-, 96-, and 120-h lead times. The method is as follows (Kim et al., 2018):

$$\sigma_{all} = \sqrt{\frac{\sum(X_c - \bar{X}_{all})^2}{n_c}} \quad (3.5)$$

$$\sigma_c = \sqrt{\frac{\sum(X_c - \bar{X}_c)^2}{n_c}} \quad (3.6)$$

where, X_c refers to the $\Delta R5$ of an individual storm; \bar{X}_c is the mean $\Delta R5$ for each cluster; \bar{X}_{all} is the mean $\Delta R5$ for the entire sample; and n_c the number of samples for each cluster.

3.2.4. Regression method of statistical-dynamical model

The present statistical–dynamical wind radii prediction scheme is developed based on a perfect-prognosis approach (Kalnay, 2003) and Elastic Net multiple linear regression. Elastic Net is a hybrid regression method that linearly combines the L1 and L2 norm of the least absolute shrinkage and selection operator (LASSO, third term in Equation (3.7)) and Ridge regression (second term in Equation (3.7)). This method has the advantages of both variable selection by shrinking unnecessary coefficients for LASSO regression and prevention of multicollinearity for Ridge regression. The Elastic Net regression equation consists of the sum of the residual sum of squares (RSS, Equation (3.8)) and the penalty term:

$$(\hat{\alpha}, \hat{\beta}) = \text{RSS} + \lambda \sum_{j=1}^p \beta_j^2 + \lambda \sum_{j=1}^p |\beta_j| \quad (3.7)$$

$$\text{RSS} = \frac{1}{n} \sum_{i=1}^n (y_i - \alpha - \sum_{j=1}^p \beta_j x_{ij})^2 \quad (3.8)$$

where, λ is a non-negative regularization parameter and is set to balance the accuracy of the regression equation based on the number of predictors used (Lin et al., 2017). Alpha hyperparameter is a tuning parameter, and as the value increases, more regression coefficients converge to 0. Here, the alpha in this regression equation is set to 0.8. Likewise, the smart predictors and their regression coefficients are selected by performing k -fold 10 cross-validations to avoid the model overfitting. In each model, only predictors whose correlation coefficient with the dependent variable is significant at a 95% confidence level are used for variable selection.

3.2.5. Estimation of symmetric wind radius

For estimation of the R30 and R50 using the predicted $\Delta R5$, the regression equations are composed of the symmetrically averaged wind radii and TC intensity (W) of the best track data and R5 estimated from the model analysis dataset during 2008-2016 (same as the training period) as the method proposed by Knaff et al. (2014). The fitted regression coefficients for R30 (Equation (3.9)) and R50 (Equation (3.10)) are given in the following equations:

$$R30 = -1.86 + 0.51W + 14.5R5 \quad (3.9)$$

$$R50 = -42.8 + 0.88W + 4.60R5 \quad (3.10)$$

Figure 3.3 shows the scatter plots of wind radius estimated from Equations (3.9) and (3.10) compared to the JMA best-track estimates. In the training period, the R30 and R50 have the mean absolute errors (MAEs) of 54.9 km and 22.9 km and correlation coefficients of 0.84 and 0.78, respectively (Figures 3.3a and c). When the same equations apply to 2017 and 2018 TC cases, MAEs increased by about 8 km for R30 compared to the results of the training period but showed a similar error of less than 1 km for R50. Meanwhile, both wind radii have strong correlations (0.83-0.85) but underestimate by about 17 km and 6 km for R30 and R50, respectively, compared to the estimates of the best track. In particular, the fitted R30 and R50 values are estimated smaller, especially for the relatively large wind radius (Figure 3.3b and d). The equations are used for R30 and R50 predictions with the predicted TC intensity and R5 (initial R5 + $\Delta R5$ prediction).

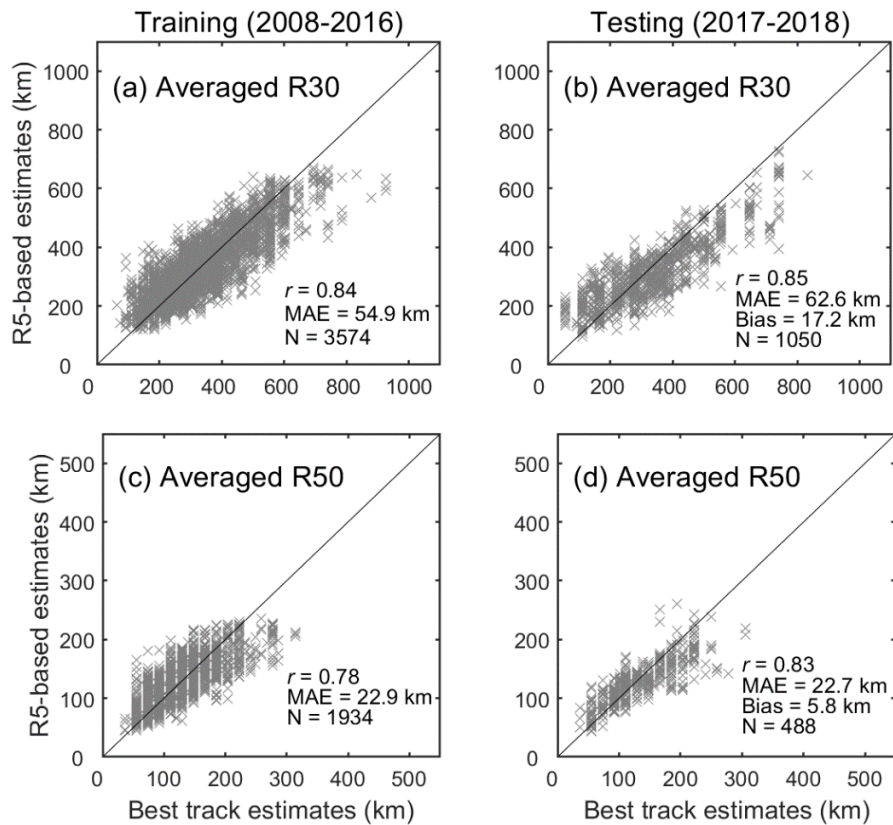


Figure 3.3. Scatter plots of averaged R30 (top panels) and R50s (bottom panels) between estimates from JMA best track data (x-axis) and estimates as a function of the TC intensity and R5 (y-axis, Equation (3.9) and (3.10) for R30 and R50, respectively) during the training (2008-2016, left panels) and testing (2017-2018, right panels) periods. The correlation coefficient (r), mean absolute error (MAE), number of samples (N), and bias (only testing period) are presented in the right bottom corner of each panel.

3.3. Statistical-dynamical TC wind radius prediction scheme

3.3.1. Effect of clustering on dependent variable

This section examined the characteristics of the track pattern and dependent variable ($\Delta R5$) of four clusters classified by the fuzzy c-means clustering method and the effect of clustering on the prediction improvement of $\Delta R5$. Track patterns of the four clusters (C1-C4) are classified as TCs passing the Kuroshio Extension (C1), TCs developing in the open ocean (C2), TCs landfall mainly in the Philippines and South China (C3), and TCs affecting the Korean peninsula (KP), Japan, and East China (C4) (Figure 3.4). The largest number of cases among the four clusters is C3 (1157, 32%), following as C4 (1024, 29%), C2 (720, 20%), C1 (673, 19%).

First, the characteristics of the $\Delta R5$ for each cluster classified over the forecast lead time are compared (Table 3.2). If the dependent variable has unique characteristics, smarter predictors suitable for each cluster can be selected, contributing to better performance for that clustering model. On average, the tendency of $\Delta R5$ increases in most clusters (0.01~3.98) and decreases in C3 (-0.25). In particular, C2 has the most significant increase of $\Delta R5$ tendency compared to other clusters and all TC cases, with the most notable features of growing $R5$ at all prediction times. For C3, $\Delta R5$ became smaller at most lead times, and gradually increased the variability (-0.4~-1.3) and standard deviations (± 6.1 ~ 6.2) of $\Delta R5$, especially after 96-h lead time. Meanwhile, complex and inconsistent increasing and decreasing values of $R5$ at each lead time for C1 and C4 led to insignificant mean values compared to C2 and C3. From this, it can be expected that the use of clustering in C2 and C3 with distinct $R5$ characteristics has

a good possibility of improving the current TC size prediction skill compared to that of C1 and C4.

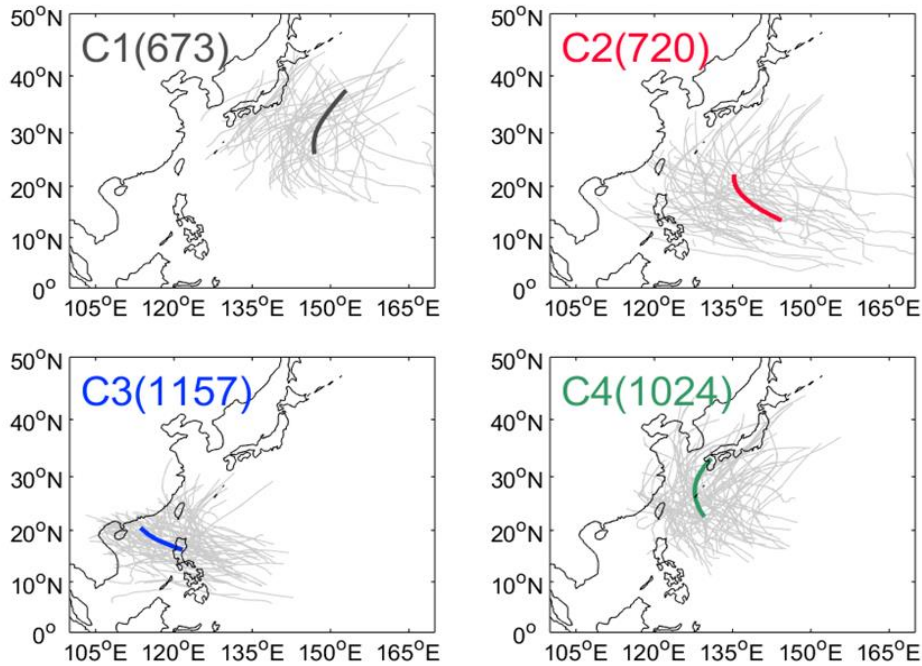


Figure 3.4. TC tracks in the western North Pacific classified using the fuzzy *c*-Means clustering method for the training period from 2008-2016. Each panel represents the TC tracks in classified four clusters (light gray) and their mean track of C1 (dark gray), C2 (red), C3 (blue), and C4 (green) with the number of cases in parentheses. For the classified similar tracks, TC tracks are interpolated equally 21 storm positions with 5-day tracks.

Table 3.2. Comparison of mean values of $\Delta R5$ for four clusters and all TCs at 24-, 48-, 72-, 96-, and 120-h forecast lead times during training period. The standard deviations of mean values are indicated in parentheses. The unit is degrees latitude (in parentheses in the first column).

	Forecast time (h)	Cluster				
		C1	C2	C3	C4	all TCs
$\Delta R5$ (degrees latitude)	24	0.21 (± 3.74)	1.58 (± 2.77)	-0.23 (± 3.70)	0.27 (± 3.73)	0.36 (± 3.61)
	48	-0.03 (± 5.82)	3.11 (± 4.44)	-0.14 (± 5.10)	0.19 (± 5.67)	0.77 (± 5.40)
	72	-0.42 (± 6.86)	4.51 (± 5.91)	0.05 (± 5.84)	0.04 (± 7.15)	1.35 (± 6.71)
	96	0.27 (± 5.97)	5.56 (± 6.91)	-0.39 (± 6.11)	-0.50 (± 8.08)	1.94 (± 7.54)
	120	1.47 (± 5.82)	6.07 (± 7.59)	-1.29 (± 6.23)	-0.84 (± 8.74)	2.49 (± 8.28)
	Mean	0.09 (± 5.29)	3.98 (± 5.84)	-0.25 (± 5.05)	0.01 (± 6.15)	1.01 (± 5.92)

As seen in Table 3.2, the classified clusters showed unique characteristics in terms of the tendency of $\Delta R5$ change. We further examined the effect of the use of clustering through the comparison of the standard deviations of each cluster before (σ_{all} , Equation (3.5)) and after clustering (σ_c , Equation (3.6)) at each lead time (Table 3.3). This result can be determined the possibility of model improvement depending on how much the $\Delta R5$ variability decreases when the clustering is applied compared to all TC cases. Overall, the σ_c decreased by about 1.7~10.3% at all prediction times compared to σ_{all} , and the reduction rate increased at relatively late prediction time. For the reduction rate of standard deviation for each cluster, C2 had the largest decrease in the range of 9 to 13% of σ_c . This result suggests that in C2, which has the highest variability of $\Delta R5$ in Table 3.2, the use of clustering is highly likely to significantly reduce variability in $\Delta R5$ and improve TC size prediction in the present statistical-dynamical model (Table 3.3). Likewise, C3 shows a significant decrease in the σ_c at most forecast lead times following that of C2 (maximum 17%) (Table 3.3). Meanwhile, C1 and C4 showed a slight improvement compared to those of C2 and C3, although the σ_c decreased from less than 7% in most prediction times (Table 3.3). That is related to the unclear $\Delta R5$ variability shown in C1 and C4 (Table 3.2). On the other hand, for C2 and C3, which showed a district variability of $\Delta R5$ by each forecast lead time (Table 3.2), the clustering effect in both clusters is expected to have a significant impact on the improvement of $\Delta R5$ prediction in the present TPC-based model (Table 3.3).

Table 3.3. Comparisons of standard deviations (σ_{all} and σ_c) of $\Delta R5$ using their mean value for each cluster and at each forecast lead time. The reduction rates of σ_c relative to σ_{all} are indicated in parentheses with bold text.

Forecast time (h)		Cluster				
		C1	C2	C3	C4	All
24	σ_{all}	3.43	2.96	3.70	3.60	3.48
	σ_c	3.42 (0.1%)	2.71 (9.3%)	3.65 (1.3%)	3.60 (0.0%)	3.42 (1.7%)
48	σ_{all}	5.28	4.91	5.13	5.50	5.21
	σ_c	5.23 (0.9%)	4.34 (13.1%)	5.75 (1.6%)	5.47 (0.5%)	5.05 (3.2%)
72	σ_{all}	6.12	6.57	5.89	6.99	6.45
	σ_c	5.92 (3.3%)	5.79 (13.4%)	5.75 (2.5%)	6.87 (1.7%)	6.13 (5.3%)
96	σ_{all}	4.99	7.63	6.42	8.07	7.21
	σ_c	4.80 (3.9%)	6.75 (13.0%)	6.01 (7.0%)	7.73 (4.5%)	6.66 (8.2%)
120	σ_{all}	4.4	8.10	7.18	9.03	7.90
	σ_c	4.3 (1.6%)	7.32 (10.6%)	6.14 (17.0%)	8.44 (7.0%)	7.16 (10.3%)

3.3.2. Characteristic and selection of predictor

To examine how the unique differences of $\Delta R5$ by cluster presented in the previous section affect the selection of predictors, we compared the correlation coefficients between $\Delta R5$ and static, atmospheric, and oceanic predictors for each cluster over the forecast lead times (Figure 3.5).

Among the four static predictors, iSIZE is found in a strong negative correlation with $\Delta R5$ (Figure 3.5a) and chosen as one of the smart predictors in most of the clusters and all TC cases, except for C2 at 24 and 48-h lead times (Figure 3.6). In particular, TCs in C2 shows a weak correlation with $\Delta R5$ rather than other clusters and non-clustering cases, since the TCs have a relatively little value and standard deviation of iSIZE (19.3 ± 5.2 degrees latitude, Table 3.4) compared to significant variations in $\Delta R5$ (red circle lines with Figure 3.5a).

For the other three static predictors, VM and DVMX have the tendency of similar correlation coefficients among clusters (Figures 3.5b and c), while LAT has different characteristics for each cluster (Figure 3.5d). In the two predictors related to TC intensity, DVMX has a stronger relationship than VM in some predictors (Figures 3.5b and c), but VM is found to be selected as a more key predictor than DVMX (Figure 3.6). Among the clusters, C4 shows the strongest positive and negative correlations in VM and LAT, respectively (green lines in Figures 3.5b and d). This may be because the variations for weakening intensity (decrease from 67.7 to 57.7) as the TC moves poleward (increase from 0.43 to 0.52) have a great effect on $\Delta R5$ in C4, especially at 96- and 120-h prediction times (Table 3.4).

For C1, VM and LAT have a clear positive correlation at 120-h forecast time, at

which $\Delta R5$ increases significantly (1.5 ± 5.8) (gray lines in Figures 3.5b and d, Table 3.2). Meanwhile, TCs in C3 are located at a relatively lower latitude with a small value of standard deviation (0.32 ± 0.06) (Table 3.4) compared to the variability of $\Delta R5$, leading to a low correlation coefficient for LAT predictor at all prediction times (blue line in Figure 3.5d). Results from most clusters are consistent with the previous findings that TCs located at high latitudes can promote the growth of TC size (Merrill, 1984).

Table 3.4. Same as Table 3.2, but a comparison of the three static predictors, iSIZE, VM, and LAT. Only the standard deviations of the overall mean value for each cluster and all TCs are shown in parentheses.

	Forecast time (h)	Cluster				
		C1	C2	C3	C4	all TCs
iSIZE (degrees latitude)	24	22.1	19.2	18.4	24.4	20.9
	48	22.5	19.4	18.7	24.9	21.3
	72	23.0	19.4	18.5	25.1	21.3
	96	23.6	19.3	18.6	25.1	21.1
	120	24.0	19.2	18.8	25.1	20.8
	Mean	22.6 (±8.7)	19.3 (±5.2)	18.6 (±5.3)	24.8 (±7.6)	21.1 (±7.0)
VM (kt)	24	57.6	69.3	60.9	67.7	63.9
	48	57.4	78.7	62.5	67.2	66.9
	72	56.0	82.2	60.8	65.4	67.7
	96	54.7	81.2	57.1	61.7	67.0
	120	54.2	76.6	54.0	57.7	65.5
	Mean	56.8 (±15.9)	77.3 (±20.5)	60.3 (±20.5)	65.5 (±18.5)	66.0 (±20.7)
LAT	24	0.49	0.26	0.30	0.43	0.36
	48	0.51	0.28	0.31	0.45	0.38
	72	0.53	0.31	0.33	0.48	0.39
	96	0.54	0.34	0.34	0.50	0.40
	120	0.56	0.37	0.36	0.52	0.42
	Mean	0.51 (±0.08)	0.31 (±0.09)	0.32 (±0.06)	0.46 (±0.08)	0.38 (±0.11)

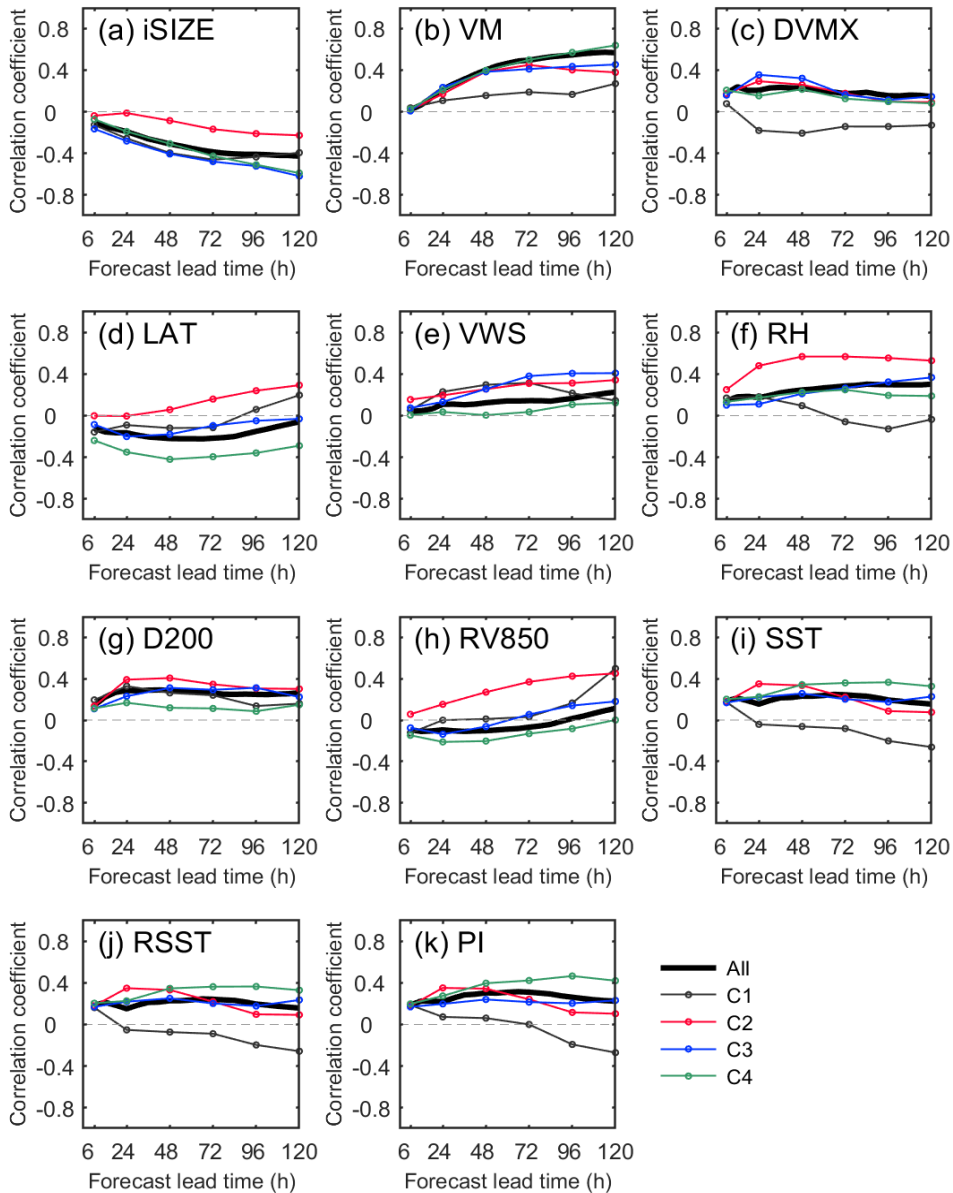


Figure 3.5. Correlation coefficients between eleven predictors, (a) iSIZE, (b) VM, (c) DVMX, (d) LAT, (e) VWS, (f) RH, (g) D200, (h) RV850, (i) SST, (j) RSST, and (k) PI and the change in TC size ($\Delta R5$) for four clusters of C1-C4 (gray, red, blue, and green circle lines) and all TC cases (black and bold lines) using all TCs at 6-, 24-, 48-, 72-, 96-, and 120-h forecast lead times during the training period (2008-2016).

The correlation coefficients between the $\Delta R5$ and four atmospheric predictors, such as VWS, RH, D200, and RV850 are compared in Figure 3.5e-h. Results showed that most of the atmospheric predictors have stronger correlations in most clusters rather than non-clustering cases. Particularly in C2, which had the most distinct variability with increasing $\Delta R5$, the largest effect on clustering is clearly shown in atmospheric predictors with the strongest positive correlations (red lines with circle in Figure 3.5e-h). According to previous studies, strong VWS and high RH and D200s are related to the extension of TC size (Hill and Lackmann, 2009; Xu and Wang, 2010; Knaff et al, 2017). In addition, RV850 is associated with the growth of TC, which is often formed in the northern monsoon trough environment (Chan and Chan, 2013 & 2015), and is consistent with a strong relationship for C2 (Figure 3.5h).

For three oceanic predictors, correlation coefficients are similar to each other, but showed a higher correlation in PI compared to SST and RSST, especially for C1 and C4 (Figure 3.5i-k). The TCs in C1 and C4 reacted more sensitively than other clusters in the oceanic environment because TC experiences a large variation in SST as it moves to high latitudes. C2 shows a relatively strong correlation before the 72-h forecast lead time, suggesting that TC intensification in the favorable environment (warm SST) for TC development may have influenced the variation in $\Delta R5$ (Table 3.4, red lines with circle in Figure 3.5i-k).

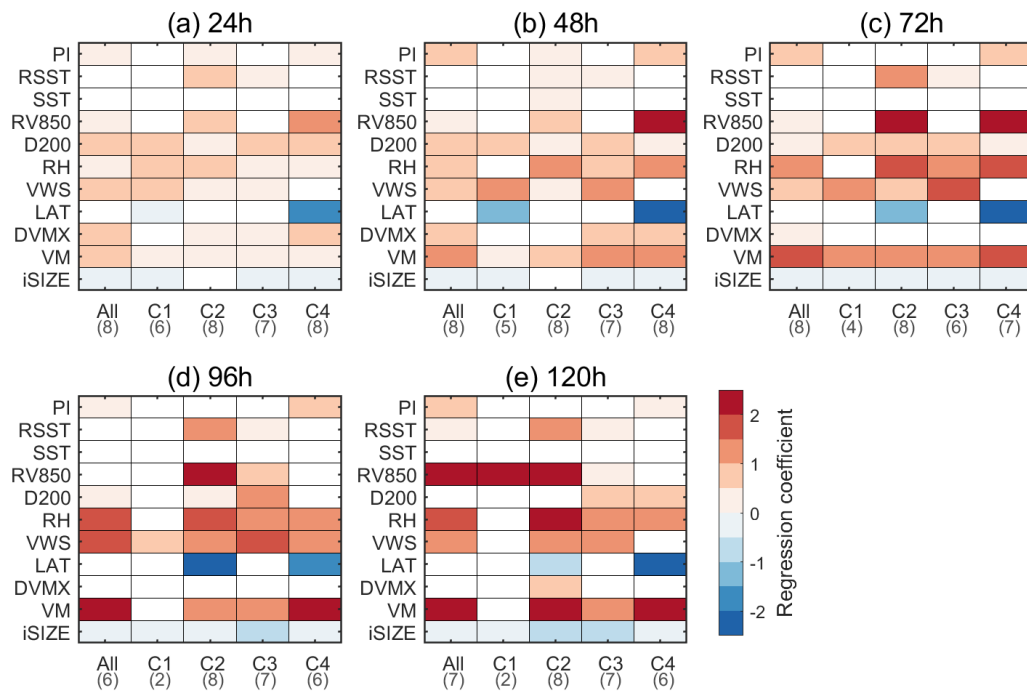


Figure 3.6. Maps of regression coefficients (shade) of final selected predictors (y-axis) for All TC cases and four clusters of C1-C4 (x-axis) using Elastic Net multiple linear regression at 24- (a), 48- (b), 72- (c), 96- (d), and 120-h (e) forecast lead times during the training years of 2008-2016. Number of selected predictors are indicated in parentheses with gray text (ranging 2-8 predictors).

Based on the Elastic Net regression method, the smart predictors are selected for each cluster and each forecast time. In general, the predictors are chosen within the range of 2~8 numbers according to each model (Figure 3.6). Among the clusters, C1 has the smallest number of selected predictors (ranging from 2~6) in all prediction times compared to other models. Even when compared with the predictors in all TCs, C1 has very few unique and smart predictors in most prediction times and weak regression coefficients, in which is likely to significantly effect on reduction of the model performance. On the other hand, the C2 model uses the most eight predictors at all prediction times, including the smart predictors with relatively high regression coefficients compared to other clusters.

Although most static predictors are chosen as one of the predictor pools in four clusters and all TCs, only VM and LAT are used as important factors for some models and forecast lead times. VM is chosen as one of the key predictors, especially in all TCs, C2, and C4 after 72-h predictions (Figure 3.6c-e). Likewise, LAT has a strong negative regression coefficient, especially at all prediction times in C4 (Figure 3.6a-e), and at 96-h lead times in C2 (Figure 3.6d). For atmospheric predictors, RV850 is chosen as one of the powerful predictors that can make a huge contribution to the model performance, except for C3. In particular, the RV850 generally shows the strongest regression coefficients in C2 after 72-h prediction times (Figure 3.6d-e). The oceanic predictors are lower regression coefficients than other predictors. Each model set as selected predictors will be verified in the following section.

3.4. Comparison of model performances

3.4.1. Training and testing periods

The performance of current statistical-dynamical models based on the perfect-prognosis approach is evaluated by comparing non-clustering (use of all TCs) and four clustering results during the training (2008-2016) and testing (2017-2018) periods using the JMA best-track, GFS analysis, and HyCOM–NCODA reanalysis datasets. Figure 3.7 shows the comparison between clustering and non-clustering results for $\Delta R5$ from two statistic techniques, such as mean absolute error (MAE) and coefficient determination (R^2), which can explain the model performance, during the training period. The result showed that the clustering model has been improved in both the MAE and R^2 compared to the non-clustering model in most prediction times. On average, the clustering model (327 ± 93 km) revealed an about 44 km decrease in MAE compared to the non-clustering model (371 ± 114 km) (Figure 3.7a).

The relative error reductions of MAEs between the non-clustering and four clustering models at 24-, 48- 72-, 96-, and 120-h forecast lead times are shown in Table 3.5. Overall, the MAEs in the clustering model are reduced in the range of about 3~24% at all prediction times. In each prediction time of clusters, the model performance has been improved significantly after 72-h forecast time, by up to 3% for C1 (72-h), 43% for C2 (96-h), 28% for C3 (120-h), and 24% for C4 (72- and 96-h). Among the clusters, C4 shows the greatest error reduction rate (6~19% improvements) compared to other clusters, prior to the 48-h forecast time. On the other hand, C1 shows a slight improvement in the clustering model and relatively small error reduction at all forecast

lead times compared to other clusters. The performance in C1 may be due to the limited selection for smart predictors, with weak correlations between $\Delta R5$ and most of the predictors (less than six numbers) (Figure 3.6). Overall, the R^2 of $\Delta R5$ shows 0.62-0.71 for the clustering model and 0.49-0.60 for the non-clustering model at 72-120-h prediction times, indicating that the use of clustering can improve the performance of $\Delta R5$ prediction (Figure 3.7b).

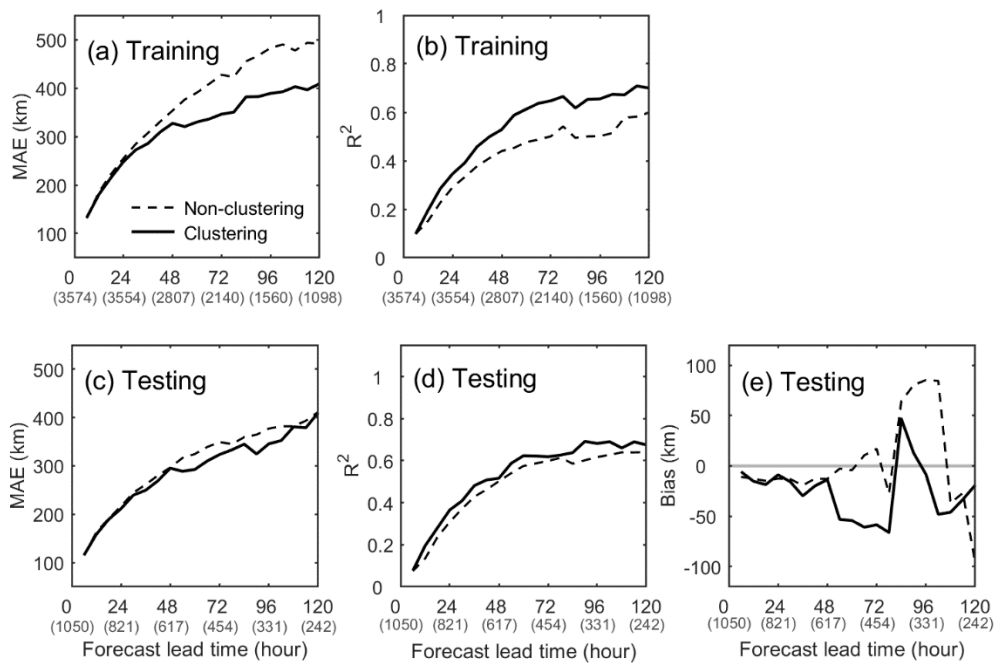


Figure 3.7. Comparisons of MAEs (a, c), R^2 (b, d), and bias (only testing, e) for $\Delta R5$ predictions between the clustering (four clusters, black and solid lines) and non-clustering cases (all TCs, black dashed lines) at each lead time during the training (2008-2016, a-b) and testing periods (2017-2018, c-e). The unit of $\Delta R5$ is km (1 degrees latitude = 111.11km). Sample sizes are indicated in parentheses at bottom of each panel for 0-, 24-, 48-, 72-, 96-, and 120-h forecast lead times.

Table 3.5. Comparison of relative error reduction of $\Delta R5$ predictions for four clusters (C1-C4) compared to all TCs during training and testing periods at 24-, 48-, 72-, 96-, and 120-h forecasting times. Negative values in bold here indicate that the clustering model has improved by that result. The sample sizes are shown in parentheses at the bottom of each relative error reduction.

	Forecast time (h)	Cluster				
		C1	C2	C3	C4	Mean
Training (2008-2016)	24	1.81% (673)	-4.18% (716)	-2.29% (1148)	-5.44% (1017)	-2.77% (3554)
	48	0.48% (469)	-0.98% (669)	-8.34% (851)	-19.1% (818)	-8.01% (2807)
	72	-3.23% (307)	-36.3% (624)	-12.3% (603)	-32.1% (606)	-23.5% (2140)
	96	0.57% (176)	-43.0% (577)	-21.7% (393)	-10.9% (414)	-24.1% (1560)
	120	-2.67% (91)	-23.7% (515)	-27.6% (239)	-12.4% (253)	-20.1% (1098)
Testing (2017-2018)	24	-0.06% (236)	1.42% (127)	-2.25% (203)	-8.29% (255)	-2.44% (821)
	48	1.07% (159)	4.65% (121)	0.19% (120)	-5.50% (217)	-0.47% (617)
	72	3.56% (100)	-70.6% (115)	5.37% (62)	9.18% (177)	-7.95% (454)
	96	8.11% (61)	-66.2% (107)	-11.7% (28)	21.2% (135)	-9.10% (331)
	120	11.8% (46)	-4.56% (97)	-22.5% (17)	2.13% (82)	-0.33% (242)

Similarly, Figure 3.7c-e shows a comparison of $\Delta R5$ performance (MAE, R^2 , and bias) of clustering and non-clustering models for testing cases in 2017 and 2018 TCs based on the best track and model analysis datasets. The analysis shows that the use of clustering models still contributes to the improvement of $\Delta R5$ prediction in both MAE and R^2 compared to non-clustering models (Figure 3.7c-d). Although the error reduction has not improved as much as the result of the training period, the use of clustering showed an average reduction of about 15 km of MAE and an improvement of up to 9% (at 96-h prediction time) during the testing period (Figure 3.7c, Table 3.5). Likewise, the R^2 showed the improvement of the clustering model during the testing period, which seems to have been mainly influenced by the C4 and C2 results before and after 48-h prediction times, respectively (Figure 3.7d). The biases of $\Delta R5$ show different results between the clustering and non-clustering models before and after the 48-hour prediction time (Figure 3.7e). Before 48-h prediction time, both models showed near-zero or slightly over-predicted results compared to $\Delta R5$ estimates. However, after 48-h forecast lead time, the $\Delta R5$ generally underestimated in the clustering model and overestimated in non-clustering model, respectively.

For each cluster, the relative error reduction of MAEs shows different characteristics by forecast lead time during the testing period (Table 3.5). Among the clusters, C2 has the greatest improvement of MAEs, by 5-71% at 72-120-h prediction times. The most distinct characteristics in terms of the $\Delta R5$ tendency in C2, as well as reduced variability in clustering (σ_c) (Tables 3.2 and 3.3) would have led to a better improvement in the TC size prediction. In addition, the use of smarter predictors after 72-h forecast time would also have helped the error reduction in C2 along with σ_c

decrease (Figure 3.6). In contrast, C4 showed a 6~8% decrease in MAEs only in some prediction times before 48-h during the testing period, unlike significant improvements in the clustering model that appeared at all prediction times during the training period (Table 3.5). We further explore the $\Delta R5$ prediction for C2 and C4 with different improvements in training and testing periods when using the clustering model after the 72-h prediction time.

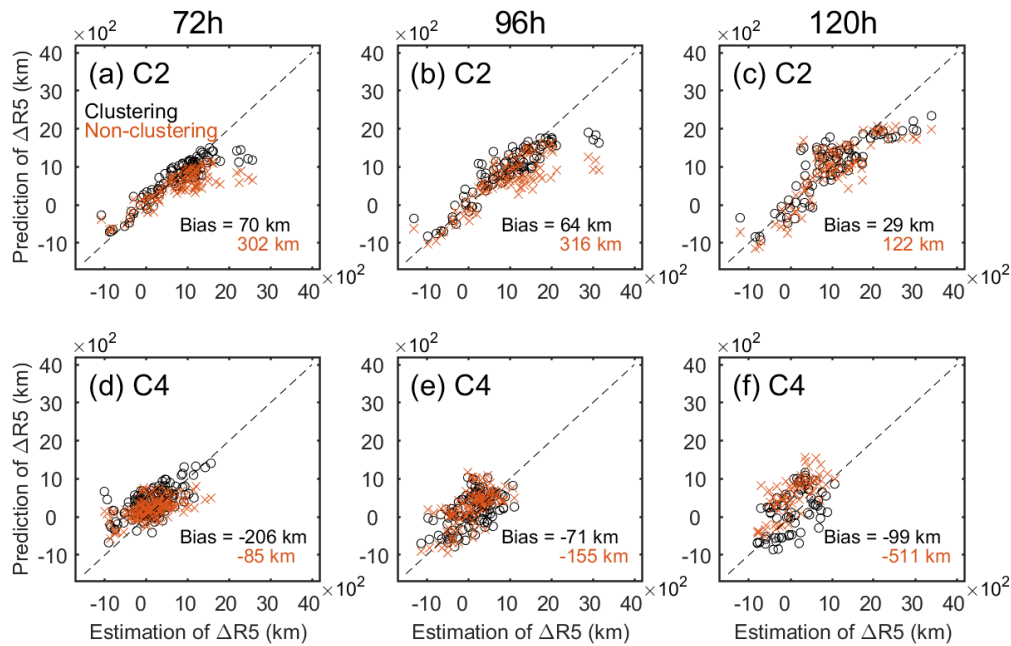


Figure 3.8. Scatter plots of $\Delta R5$ predictions using a clustering (black circle) and non-clustering model (orange cross) compared with $\Delta R5$ estimates (x-axis) at 72-h (a, d), 96-h (b, e), and 120-h (c, f) forecast lead times for C1 (a-c) and C4 (d-f) during the testing period (2017-2018). The bias of the results is indicated in the bottom right corner of each panel by clustering (black text) and non-clustering model (orange text). The unit of $\Delta R5$ is km.

Figure 3.8 shows a comparison of the $\Delta R5$ predictions after 72-h prediction time when using clustering models for C2 and C4 and non-clustering models. For C2, the $\Delta R5$ predictions using the clustering model generally showed a much smaller bias compared to the non-clustering model, by 93~152 km differences, especially in the increasing $\Delta R5$ (more than 2000 km) at 72-h and 96-h prediction times (Figure 3.8a-c). In general, C4 seems to have a greater spread of the $\Delta R5$ prediction in the clustering model than in the non-clustering model and appears overestimated results by 85~206 km in both models (Figure 3.8d-f). In particular, at the 72-h prediction time of C4, the clustering model showed an overprediction of $\Delta R5$ at a large negative value (near -1000 km) compared to the non-clustering model, but showed better performance as $\Delta R5$ increased to a positive value (Figure 3.8d). We found that the clustering model can lead to improvements in $\Delta R5$ predictions at some forecast times in both clusters as $\Delta R5$ increases significantly. However, the relatively large outlier and spreads in the $\Delta R5$ predictions of the C4 model compared to the non-clustering model still need to be further investigated.

3.4.2. Real-time predictions of dependent variable, R30, and R50

According to the procedure shown in Figure 3.9, the current TPC-based statistical-dynamical scheme for predicting real-time R30 and R50 is constructed as follows: (i) the 5-day KMA forecast tracks, the 6-hourly GFS atmospheric forecast data, and the daily real-time HyCOM/NCODA ocean surface data are collected, (ii) the dependent variable and eleven predictors are calculated for each forecast lead time, (iii) a cluster is found for the current TC forecast track using FCM, and then the model is performed, (iv) finally, the outputs of the symmetric R30 and R50 are calculated from Equations (3.8) and (3.9) using the predicted dependent variable ($\Delta R5$), the initial R5 estimated from the GFS analysis dataset, and the current intensity from the TC forecast track.

This section verifies the performances of real-time $\Delta R5$, R30, and R50 predictions for 2017 and 2018 TCs. Firstly, the performances of the predicted $\Delta R5$ in real-time using the clustering and non-clustering models are statistically examined (Figure 3.10). Overall, the MAE and bias of the clustering model reduced significantly in most prediction times (Figures 3.10a and c), but R^2 showed poor performances compared to the non-clustering model (Figure 3.10b).

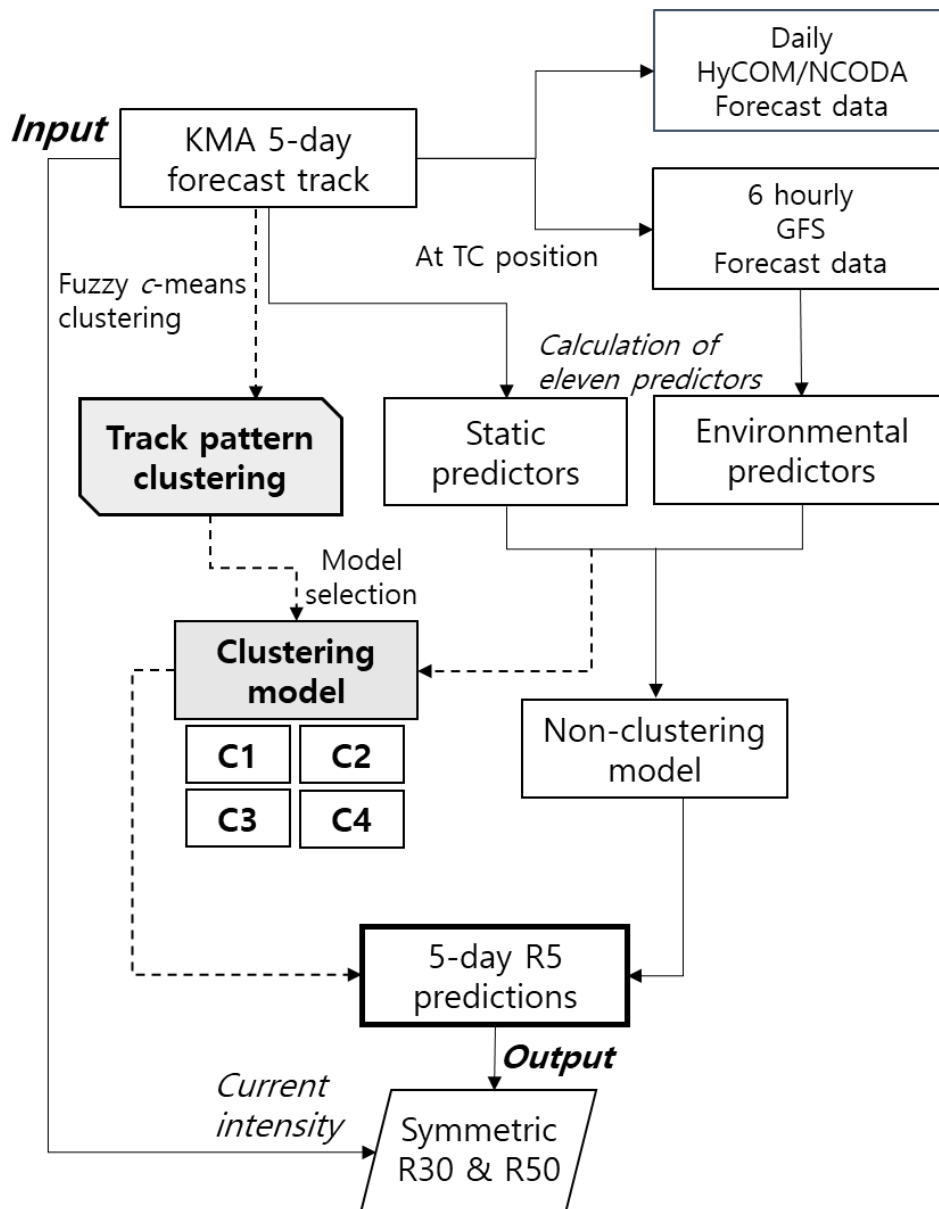


Figure 3.9. Schematic diagram of the present statistical-dynamical model for real-time R30 and R50 predictions.

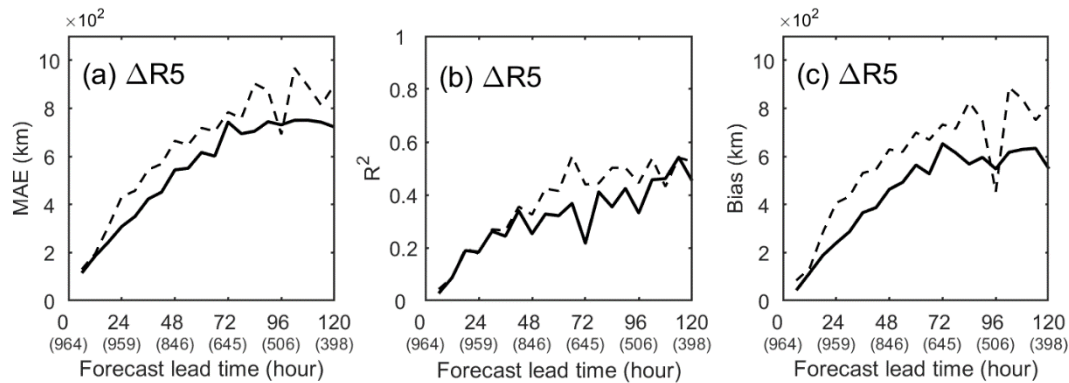


Figure 3.10. The same as Figure 3.7, but for MAEs (a), R^2 (b), and bias (c) of real-time predictions of $\Delta R5$.

To identify the cause of the large errors and biases and low R^2 of the real-time cases compared to testing cases in Figure 3.7c-e, we examined the $\Delta R5$ predictions in 2017 and 2018 TCs at five forecast lead times (Figure 3.10). First, when compared with $\Delta R5$ estimates, the real-time predictions have been shown to underpredict in both clustering and non-clustering model over forecast lead time (black and orange cross in Figure 3.11). One reason for the overall underprediction in real-time $\Delta R5$ is the difference in predictor values which can occur by using forecast track and model datasets. At 96-h prediction time, where a clear large bias is clear compared to the testing case (Figure 3.11d), we found that the VM and wind fields shown in the forecast data sets (track and model) are relatively weaker predicted compared to the best track and analysis fields. Here, VM is weaker, by 4 knots on average (maximum 85 knots) in the KMA track. In addition, relative vorticity, which is used as the key predictor in the current statistical regression model, is predicted to be weaker by about $1.3 \times 10^{-6} \text{ s}^{-1}$ compared with the analysis dataset.

Additionally, we examined why the use of the clustering model in real-time prediction has poor performance compared to the non-clustering model. A significant number of predicted outliers in the clustering model are most pronounced, especially at the 72-hour forecast time (black cross in Figure 3.11c), which contributed to the lowest R^2 (black cross in Figure 3.10b). The large errors are mainly observed in five TCs: Lan (2017), Jebi (2018), Mankhut (2018), Trami (2018), and Kong-rey (2018). The track pattern of most TCs corresponded to C4, and key predictors such as RV850, RH, LAT, and VM are used for $\Delta R5$ predictions at 72-h forecast time (Figure 3.6c). We found that the RV850 and LAT predictors, which were not used in the non-clustering model, were affecting large errors and outliers. Analysis showed that the predicted RV850s were smaller by $-1.7 \cdot 10^{-6} \text{ s}^{-1}$ for all cases and $-2.3 \cdot 10^{-6} \text{ s}^{-1}$ for C4 compared to the model analysis dataset, leading to small $\Delta R5$ predictions and large errors. Meanwhile, the predicted LAT is on average about 1°N higher than the best track. Since the regression coefficient of the LAT predictor has a negative value in Figure 3.6c, the higher LAT shows a larger negative result. That is, this implies that relatively high latitude in the forecast track may have contributed to the small $\Delta R5$ predictions.

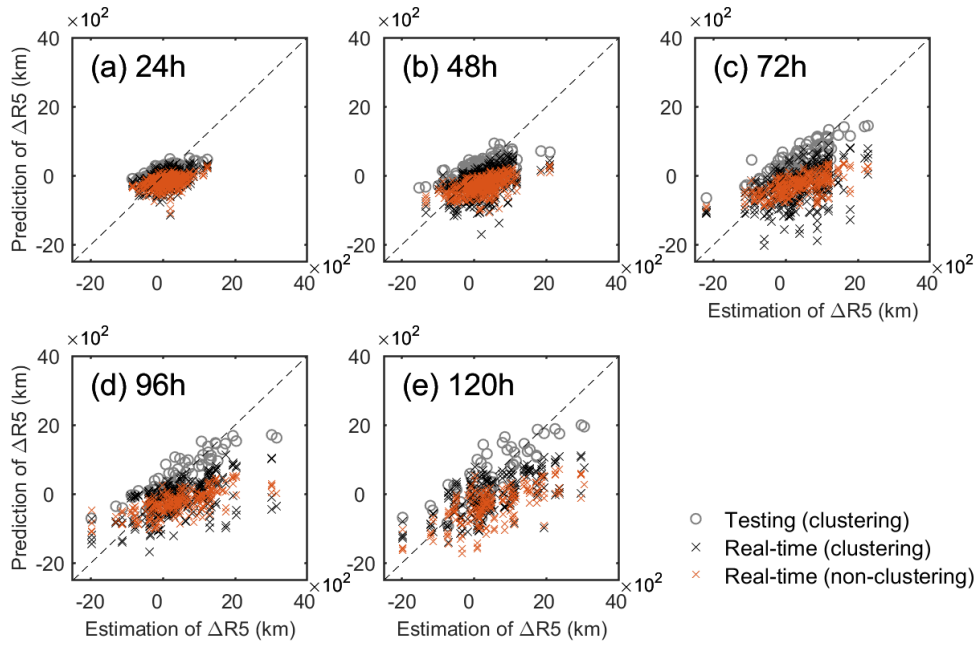


Figure 3.11. Scatter plots of $\Delta R5$ predictions using a clustering (black cross) and non-clustering models (orange cross) of real-time cases and clustering model of testing cases (gray circles) compared with $\Delta R5$ estimates (x-axis) at 24-h (a), 48-h (b), 72-h (c), 96-h (d), and 120-h (e) forecast lead times for all TC cases in 2017 and 2018. The unit of $\Delta R5$ is km.

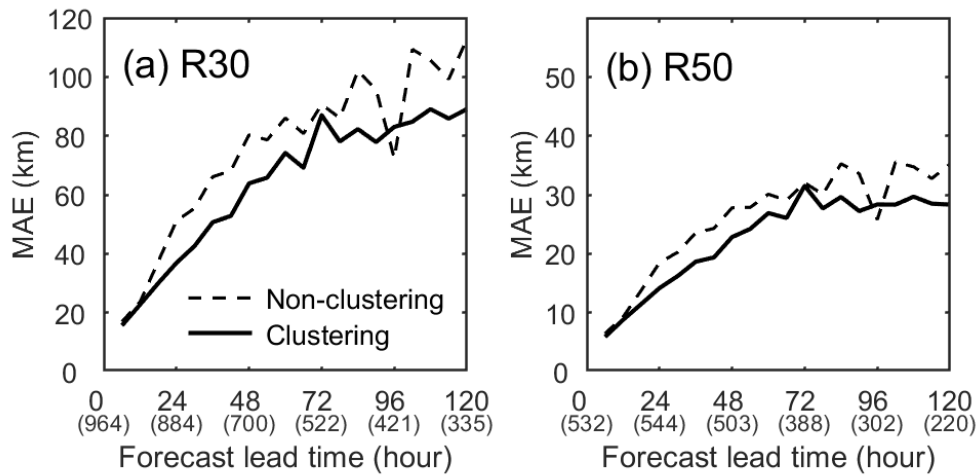


Figure 3.12. Comparisons of MAEs for real-time R30 (a) and R50 (b) predictions between the clustering (four clusters, black solid lines) and non-clustering cases (all TCs, black dashed lines) at each lead time. The unit of MAE is km.

The MAEs of real-time R30 and R50 predictions mostly increased over the forecast lead time. When averaged the errors in all prediction times, the MAEs are 61 ± 27 (72 ± 31) km for R30 and 21 ± 9 (25 ± 10) km for R50 in the clustering model (non-clustering model) (Figure 3.12, Table 3.6). Comparing the real-time prediction errors for both models in terms of MAE and normalized MAE (NMAE) by each cluster, both MAE and NMAE of the clustering model are reduced in most clusters, except C3. For C2, although the absolute value of the error is the largest compared to other clusters, both MAE and NMAE have been significantly reduced in the clustering model, by about 14 (5) km and 0.04 (0.03) km for R30 (R50), respectively (Table 3.6).

Table 3.6. Comparison of averaged MAE and NMAEs of real-time R30 and R50 predictions using the clustering and non-clustering models for four clusters.

		Cluster				
		C1	C2	C3	C4	Mean
R30	Clustering	47±19 (0.15±0.06)	77±39 (0.20±0.08)	63±39 (0.21±0.08)	50±21 (0.13±0.05)	61±27 (0.17±0.07)
	Non-clustering	58±23 (0.17±0.07)	91±43 (0.24±0.10)	62±29 (0.21±0.10)	66±26 (0.17±0.07)	72±31 (0.20±0.08)
R50	Clustering	16±6 (0.15±0.06)	29±13 (0.20±0.08)	23±8 (0.22±0.10)	16±6 (0.11±0.10)	21±9 (0.16±0.07)
	Non-clustering	19±7 (0.18±0.07)	33±15 (0.23±0.09)	21±7 (0.19±0.08)	20±8 (0.15±0.06)	25±10 (0.19±0.08)

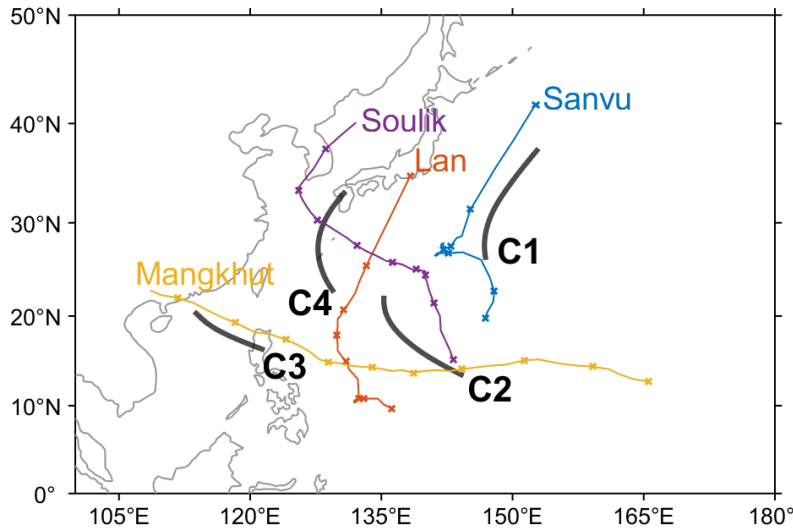


Figure 3.13. TC tracks of Typhoon Sanvu (blue line) and Lan (red line) in 2017, and Typhoon Mangkhut (yellow line) and Soulik (purple line) in 2018. The thick black lines in map represent the mean track for four clusters.

To further explore the real-time R30 predictions, representative four TCs are chosen for the following case study: Sanvu (2017) for C1, Lan (2017) for C1, C2, and C4, Mangkhut (2018) for C2 and C3, and Soulik (2018) for C2 and C4 (Figure 3.13). Regarding each TC case, the R30 predictions are examined in association with TC intensity and the membership coefficients along with the mean tracks for each cluster, as well as comparisons with the R30 estimates (Figure 3.14).

Typhoon Sanvu, which belongs to C1 during the TC's lifetimes, shows relatively high membership coefficients between each predicted track and their mean track ranging from 0.67 to 0.93 (blue lines in Figure 3.14e and blue track in Figure 3.13). However, Sanvu's R30 predictions show significant differences from the R30 estimates during the TC's lifetime (black and gray solid lines in Figure 3.14a). This may be associated with the unpredictable variability of R30 that appears regardless of

the TC intensity and locations (red line in Figure 3.14e), which leads to difficulties in R30 predictions. Both the R30 estimate and their predictions are relatively smaller than estimates from JMA best track, by about 296 km, supporting that estimation of Sanvu's wind radius during the TC lifetime was quite difficult (Figure 3.14a).

In the case of the other three typhoons, Lan, Mangkhut, and Soulik, they have undergone cluster changes more than two times during their TC lifetime and had mostly similar R30 estimates between the model and best track datasets commonly (Figure 3.14b-d). In three TCs, we found that the relatively low track membership coefficients that appeared mostly when the clusters changed affected the increase in the R30 prediction error in the present TPC-based model, for Lan (on Day2), Mangkhut (on Day 4), and Soulik (on Day 1), respectively (gray lines in Figure 3.14b-d and blue lines in Figure 3.14f-h).

Typhoon Lan experienced large and abrupt changes in R30 estimates from 200 to 600 km during the C2 (before Day 2), resulting in poor performance as the R30 predictions did not keep up with these changes (Figure 3.14b). Likewise, R30 showed a large prediction error on Days 3-5 in C4, because the large intensity error between the actual and forecast track (up to 17 knots) caused by the rapid intensification of Lan contributed significantly (Figure 3.14b and red line in Figure 3.14f). For Typhoon Mangkhut, except for Day 4, which undergoes a cluster change from C2 to C3, the R30 predictions showed the most ideal result that relatively well followed the results of TC intensity and R30 estimates during the storm's lifetime (Figures 3.14c and g). Finally, the predictions of Typhoon Soulik are most similar to R30 estimates during Days 2~6 (Figure 3.14d). However, after Day 7, the performance of the R30 prediction

3.5. Summary and discussion

A statistical-dynamical model used for the symmetric R30 and R50 predictions in the WNP was developed using the Elastic Net regression methods, track pattern clustering, and eleven static/synoptic potential predictors. This study was defined the TC size proxy as R5 calculated from 850-hPa tangential winds and focused on predictions of change in R5 ($\Delta R5$) relative to initial time. By using the fuzzy *c*-means clustering method, the tracks of TCs were classified into four clusters, and the specific characteristics of each cluster and effects of using clustering were examined.

In general, the final smart predictors were chosen within the range of 2~8 numbers for each cluster and each forecast time. Among the predictors, VM, LAT, and atmospheric predictors were used as important variables for most of models and forecast lead times. To examine the effects of using clustering in $\Delta R5$ prediction, the performance was evaluated by training (2008-2016) and testing periods (2017-2018) based on the model analysis and best track datasets. Analysis showed that use of clustering significantly reduced the MAEs in training period (3-24% improvements at 24-120-h lead times) compared to non-clustering cases, but slightly reduced in testing period (maximum 8-9% at 72-96-h lead time). Among the clusters, C2 had greatest improvement of MAEs in both periods similarly, by about 24-43% for training period and 5-71% for testing period at 72-120-h lead times. We found that C2 had the most distinct characteristics in terms of the tendency to $\Delta R5$ as well as to reduce of variability in clustering (σ_c), leading to a better improvement in the forecast of TC size. Meanwhile, for the other three clusters, the clustering model showed performance

improvement only at some lead times (C3-C4) or no improvement at all (C1), during the testing period. It seems that the models were not significantly improved because the unique predictors was not chosen for each cluster due to the relatively low σ_c of $\Delta R5$, unlike C2.

The current system based on statistical-dynamical approach and track pattern clustering was verified through the real-time performances of $\Delta R5$, R30, and R50 predictions and case studies using the KMA forecast track and model forecast datasets for 2017 and 2018 TCs. Overall, the errors of the clustering model reduced at most prediction times significantly, but model variance showed similarly (prior to 48-h lead time) or poorly performances (after 72-h lead time) compared to the non-clustering model. Although the use of clustering still helps to improve TC size prediction in real-time, some large outliers posed by forecast errors of the TC intensity and R5 were affecting the model performance. However, through a representative case study, we found that errors of R30 predicted in corresponding cluster are significantly influenced by track membership coefficients.

A present scheme for TC wind radius prediction has a limitation in that the asymmetries of R30 and R50s have yet to be considered. Global TC agencies such as JTWC and NHC uses a parametric model, namely the modified Rankine Vortex based on climatological estimates in TC translation speed, latitude, and intensity for estimating and predicting the asymmetry. However, because the method is climatological motion-relative asymmetries, considering asymmetry in actual TC structure remains a challenge and further understanding the causes of convective and wind field asymmetries and extratropical transitioning and stages of TCs required

(Knaff et al., 2017). Also, the benefits of the partially existing clustering models remain for further improvement. If the sample size increases in the future as more TC data are collected, it is expected to improve the model skill for wind radii predictions. Additionally, efforts are still needed to improve the R30 predictions of TC, such as Typhoon Lan (2017), which experience a rapid change of TC size regardless of the TC intensity and track patterns (Figure 3.14b).

The process for wind radii prediction had many limitations for model development, such as relatively short-time of best-tracks, subjective estimates among agencies, and dependence on satellite-derived data and TC intensity compared to other TC factors. Nevertheless, this study suggests the possibility of real-time operational guidance in the objectively values of R30 and R50s estimated based on the R5 and TC size-related predictors applied track pattern clustering.

4. Prediction of the gale wind radius in western North Pacific based on Global Forecast System

4.1. Introduction

Estimating and predicting the structure of the tropical cyclone (TC) wind field is a critical part of the forecast process in global TC warning centers. The real-time wind radii estimates are used to initialize numerical weather forecasting (NWP) models (Tallapragada et al. 2015; Kurihara et al. 1993; Bender et al. 2017) and have been found that the helped improve TC track (Kunii; 2015, Tang et al., 2020) and intensity forecasts (Marchok et al., 2012; Pun et al., 2018) and, evolution of TC structure during vortex initialization (Wu et al., 2010). Furthermore, such real-time estimates are used as important information in the TC-induced storm surge/wave forecast modeling for use in disaster prevention near coastal lines (Powell and Reinhold 2007; Sampson et al., 2010; Quiring et al., 2014).

Gale-force wind radii are the outermost TC size in terms of winds officially provided by global TC agencies, and defined as the maximum extents of the 34-kt (17 m s^{-1} , R34) and 30-kt winds (15 m s^{-1} , R30). However, accurate estimations of R30 and R34 are difficult because the incomplete or asymmetric structure of the TC appears frequently under the influence of synoptic background flow surrounding the TC, especially at higher latitude with fast storm translation speed (see Figure 2.11d and 2.13d in Section 2). In addition, for TCs embedded in a monsoon trough, it is more difficult to estimate because boundary between the monsoon westerlies or trade easterlies and the TC location where the TC circulation begins is ambiguous (Weber

et al., 2014). This cause contributes to the difficulty in estimating the objective TC sizes that can be derived from various datasets.

A more accurate real-time wind radius estimation and prediction depends on the quality of the available dataset and which method is used. The observational sources such as aircraft reconnaissance, ship, and satellite-derived scatter-meters are not routinely offered (Sampson et al., 2017), and therefore only available in a few storm cases when they are near or passing over a TC. Several real-time objective techniques have been reported to estimate the satellite-based wind radius. The Advanced Microwave Sounding Unit (AMSU), which covers of the polar-orbiting satellite swath over the TC mostly and has a resolution of approximately 48 km, is one of the frequently utilized satellite data sources for estimating the wind radii in many studies. Demuth et al. (2004) are first suggested statistical procedure for azimuthally averaged radii of 34-, 50-, and 64-kt winds (R34, R50, and R64) estimation that uses the AMSU-derived potential parameters. This statistical regression method has been further updated to use more environmental parameters (Demuth et al., 2006), and to consider the asymmetries of wind radius (Dolling et al., 2016). However, satellite-based real-time estimates are mostly employed indirectly methods in which multiple regression models with various environmental parameters are applied.

A gridded datasets with a long period and uniform spatiotemporal spacing partially compensate for the deficiencies in the observations of TC. Many studies suggest that errors in TC location and intensity are significantly reduced when used the reanalysis datasets (Schenkel and Hart 2012; Hodges et al. 2017) due to increased horizontal resolution of advanced NWP and the application of optimized assimilation and bias

correction systems (Schenkel and Hart 2012; Hodges et al. 2017; Lei and Whitaker 2017). In terms of wind radii, the combination of improved NWP model techniques, more satellite-based estimates, and tools to efficiently reconnaissance these estimates can generate high-accuracy estimates of R30 or R34 for use by the JTWC and other agencies (Sampson et al., 2017).

For real-time prediction, the NWP data sets are currently limited to the Global Forecast System (GFS) model, the Hurricane Weather Research and Forecasting Model, and the Geophysical Fluid Dynamics Laboratory Hurricane model in U.S TC warning centers. In JTWC, to form our objective estimates of initial wind radii, satellite-based and model-based estimates are combined using an equally weighted average, allowed to vary between one and six, depending on their availability (Sampson et al., 2018). So far, forecasts of wind radii have been improving as well, and skill has been found in individual forecast models (Tallapragada et al. 2014; Cangialosi and Landsea 2016; Knaff et al. 2017), consensus forecasts, and forecasts from the operational centers (Knaff and Sampson 2015).

This study aims to propose an objective procedure for directly and spatially estimation of the asymmetric axes of R30 from available real-time NWP model data sets, which has a high-resolution. We also are verified the performance of wind radius predictions using current system, applying the model forecast wind fields. The remainder of this paper is organized as follows. Section 4.2 introduces the data and methods. Section 4.3 compares the R30 objectively extracted from the model data sets from analysis and forecast wind fields by experiment. Finally, a summary and discussions are given in Section 4.4.

4.2. Data and methods

4.2.1. Information of TC and model input

The best track data is obtained from the Korea Meteorological Administration (KMA), which contains six-hourly estimates of the latitude, longitude, 10-min maximum sustained surface winds, central pressure, longest and shortest axes of the radial extent of 30- and 50-kt winds, and direction of shortest axis in ranges of 0 to 360° at 22.5° intervals, during 2015-2019. In this study, the track data is reconstructed into 5-day dataset at 6-hourly intervals by each TC. For the 5-year period, we used total of 2477 cases in WNP TCs and 1852, 1427, 1066, 770, and 540 cases at 24-, 48-, 72-, 96-, and 120-h forecast times, respectively.

The gridded data of the model were obtained from the six-hourly National Centers for Environmental Prediction (NCEP)/Global Forecast System (GFS) with 0.25° × 0.25° horizontal resolutions. The GFS data has been provided operationally available in the form of analysis and 5-days forecast datasets since 2014. For estimation of TC wind radius from the model dataset, basic wind fields are generated from u- and v-wind components at 1000 and 850 hPa, respectively. A wind field at 1000 hPa is a near-surface wind dataset frequently used in the model data to capture the wind structure of TC. However, the TC wind field near the surface is exposed to an environment where the structure is easily damaged by external factors, making it difficult to estimate the TC wind radii. We consider the use of higher-level wind fields to better capture the structure of the TC. Instead of using near-surface wind field observations, Knaff et al. (2014) used 850 hPa tangential winds of the infrared satellite

data for estimating the objective wind radii. We further tested R30 extracted from the 850 hPa wind field in the model dataset and compared the results with 1000 hPa.

Considering the differences in TC position between model forecast and best track datasets, the method suggested by Bian et al. (2021) is used to determine the storm location from the model dataset. Here, the TC positions in the best track are used as approximate locations to iteratively determine the storm centers from the six environmental variables (925-hPa, 850-hPa, and 700-hPa relative vorticities; 850-hPa and 700-hPa geopotential heights; and mean sea-level pressure) in forecasting data during 6~120-h prediction times. The final center of TC is defined as the average value of the six positions estimated from each environmental variable.

4.2.2. Preprocessing of TC wind field

Even though the TC structure is better captured using wind fields at a higher level (850 hPa) than near-surface (1000 hPa), the complex large-scale system surrounding the TC still makes it difficult to the objective estimation of the R30. To overcome the difficulty of estimating R30 due to the large asymmetry that occurs effect of the large-scale environment surrounding the TC, the simple vortex filtering technique suggested by Kurihara (1993) is applied to remove the influence of the environmental wind fields. The filtering technique is introduced in Equations (4.1) and (4.2).

$$\bar{h}_{\lambda,\varphi} = h_{\lambda,\varphi} + K(h_{\lambda-1,\varphi} + h_{\lambda+1,\varphi} - 2h_{\lambda,\varphi}) \quad (4.1)$$

$$K = \frac{1}{2}(1 - \cos \frac{2\pi}{m})^{-1} \quad (4.2)$$

In Equation (4.1), the wind gridded data sets at u- and v-components interpolated with a horizontal resolution at $1^\circ \times 1^\circ$ are finally removed as the vortex is smoothed by the variable coefficient “K” through eleven steps ($m = 2, 3, 4, 2, 5, 6, 7, 2, 8, 9$) shown in Equation (4.2). Finally, the wind field in which most of the vortex is extracted but only remains the background flows in the final step is removed from the existing wind fields at 1000 hPa and 850 hPa, respectively.

Table 4.1. The brief names and descriptions of four sensitivity experiments.

Experiment	Definition
CTRL1000	Estimation of longest axes, shortest axes, and directions for R30 from a basic wind field at 1000 hPa
CTRL850	Same as CTRL1000 but for use of 850 hPa wind fields
KF1000	Estimation of longest axes, shortest axes, and their directions for R30 from a wind field that removed the background flows surrounding the TC using Kurihara filtering at 1000 hPa
KF850	Same as KF1000 but for use of 850 hPa wind fields

Based on the wind fields introduced above, we performed four sensitivity experiments for estimating the objective R30 from the model dataset presented in Table 4.1. Two CTRL experiments are suggested as general estimation methods of R30 from the model wind fields at 1000-hPa (CTRL1000) and 850-hPa (CTRL850) in the raw dataset before the removal of background flow. Since these experiments use the wind field of the model itself to account for a significant amount of TC asymmetry, it will be possible to estimate the gale wind radius more realistically. Two experiments with Kurihara filtering (KF) at 1000 and 850 hPa wind fields are also compared to CTRL experiments, and defined as KF1000 and KF850, respectively. These KF experiments are expected to be advantageous for objective estimating the TC wind radius by extracting the wind field of the typhoon itself and producing a clear TC wind field structure. The results of the longest and shortest axes of R30 from the four experiments are compared with the R30 estimates of KMA best track data.

For example, the wind distributions for the four experiments are compared in Figure 4.1 at 00:00 UTC on July 24 of Typhoon Wukong (2018). Wukong had a relatively weak intensity (41 knots) and far and wide TC wind areas with an asymmetric structure, making it difficult to objectively estimate the R30 in both CTRL

wind fields (black solid line in Figures 4.1a and c). Meanwhile, the wind fields with KF showed a relatively symmetrical TC structure compared to CTRL (black solid lines in Figures 4.1b and d), and the R30 estimates are similar to the KMA best track (red and blue dashed circles in Figures 4.1b and d).

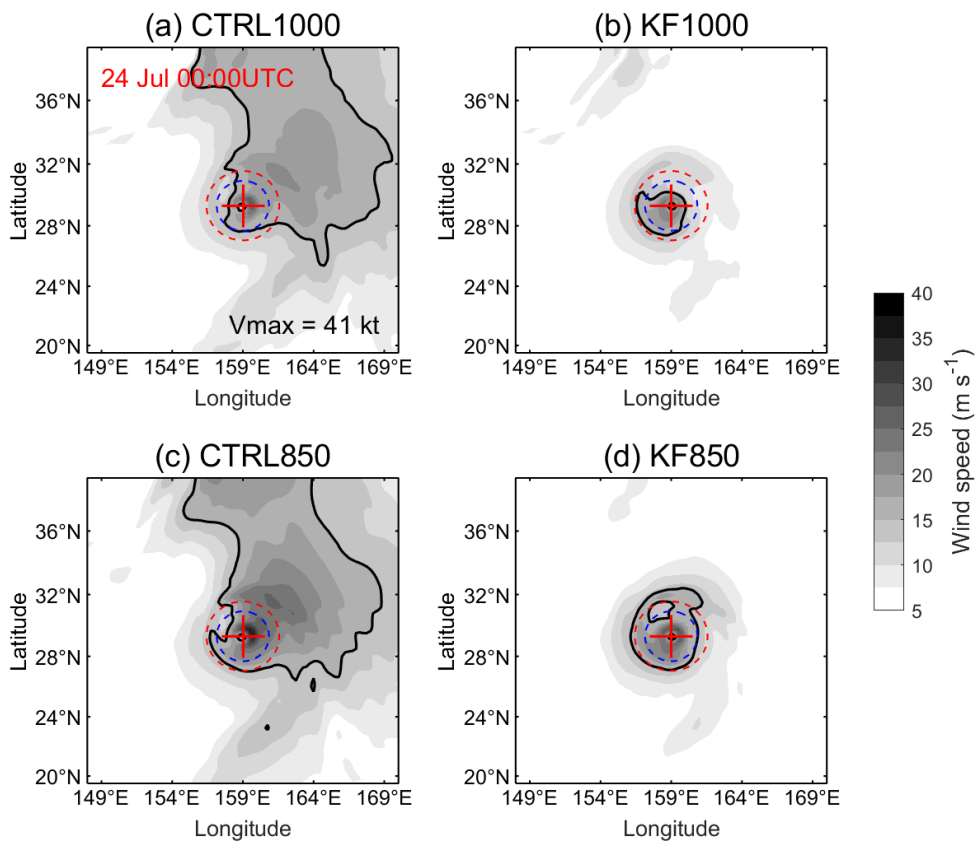


Figure 4.1. Comparison of the spatial wind fields (shade) from GFS model analysis for using the four experiments, CTRL1000 (a), KF1000 (b), CTRL850 (c), and KF850 (d), and the R30 (black and solid contours) for Typhoon Wukong (2018) at 00:00 UTC on July 24 (upper-left corner in (a) with red text). Red plus symbols indicate the tropical cyclone's center. Red and blue dashed circles indicate the longest and shortest axes of R30 from the KMA best track. The maximum wind speed (V_{max}) from KMA is shown in (a).

4.2.3. Estimation of gale wind radius of TC

To objectively extracted the longest and shortest R30s from the wind fields in four experiments, we first produced radial wind profiles in each wind field in sixteen directions (ranging from 0-337.5° at 22.5° intervals) from the storm heading. The profiles are created at 5° intervals and averaged within the corresponding range in 16 directions, resulting in 16 averaged profiles.

Using the generated 16 radial wind profiles by each experiment, our system is automated by imposing several conditions for estimating the longest axis and short axis of R30. First, we empirically calculate the maximum wind speed radius (RMW) using the current TC intensity and latitude (Knaff et al., 2017) by each TC and find 16 gale wind radii in an outer radius greater than the estimated RMW. The reason for using empirical estimates of RMW in our system is to minimize the production of erroneous RMWs in wind profiles other than typical TC structures. Second, to avoid the extraction of an exceptionally large radius in our automated system, we set the threshold of the outer wind radius for each profile. The threshold of the outer radius is defined as the endpoint in which the wind gradient gradually decreases from the RMW to the outer radius of 1500 km with less than 15 m s^{-1} .

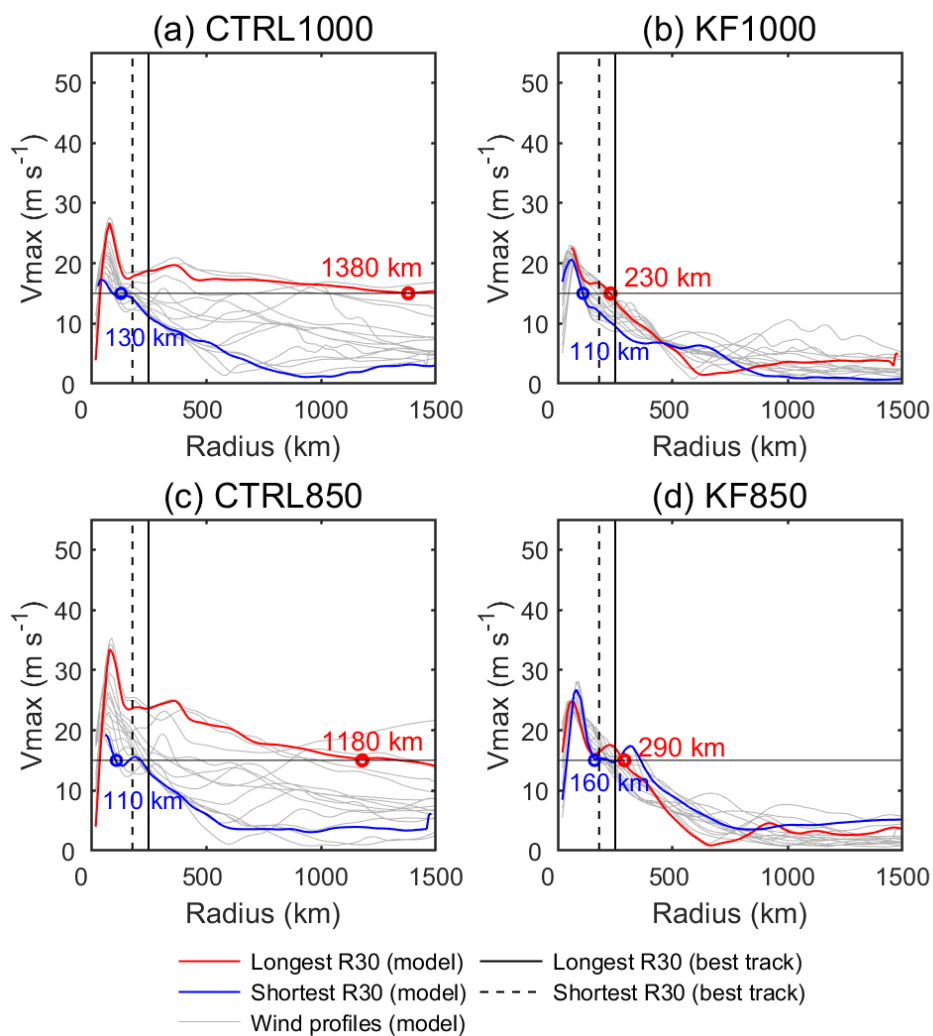


Figure 4.2. Comparison of radial wind profiles as the same case in Figure 4.1 for four experiments, CTRL1000 (a), KF1000 (b), CTRL850 (c), and KF850 (d) and longest (red profiles and values) and shortest (blue profiles and values) axes of R30 extracted from the sixteen profiles (gray) in the current system. Black solid and dashed lines indicate the longest axis and shortest axis of R30 from the KMA best track, by 250 km and 180 km, respectively.

Along with the conditions applied to the system, we extracted the largest value in the radius reaching 15 m s^{-1} from each profile and found the longest axis and shortest axis in the estimated 16 wind radii. For example, the 16 radial profiles estimated from Typhoon Wukong's wind fields for the four experiments (see Figure 4.1) and the longest and shortest axes of R30 found in our system are shown in Figure 4.2. The most notable results are the changes in the longest axes between the CTRL and KF experiments (red profiles and values in Figure 4.2). In both KF experiments, the longest axis of R30 is significantly similar to the KMA (black and solid line) compared to the CTRL experiments, which had a large radius of more than 1000 km. Similar results were also confirmed in the spatial distributions of the wind fields in Figure 4.1. The extension of gale winds in the KF experiment was almost identical to the longest R30 of the KMA (red and dashed circles in Figures 4.1b and d).

Meanwhile, the shortest axis yields similar R30 estimates in the four sensitivity experiments ranging from 110-160 km (blue profiles and values in Figure 4.2). Interestingly, the shortest R30 estimates in KF850 had 50 km larger than that of CTRL850 (blue profiles and values in Figures 4.2c and d), which implies that the use of an 850 hPa wind field with KF captured a most symmetrical TC structure rather than other experiments (Figures 4.1c and d).

4.3. Results

4.3.1. Comparison of R30 estimates in four experiments

According to the procedure described in section 4.2, we estimated the R30 from the four experiments based on the model analysis dataset. The R30s estimated objectively in each experiment are compared statistically with the estimates of KMA in Table 4.2. In general, KF experiments show lower mean absolute error (MAE) and higher correlation coefficient (r) compared to CTRL experiments on both the longest axis and the shortest axis of R30. In particular, the longest R30s showed relatively larger MAE reductions of about 183 km (73%) and 335 km (77%) in the KF1000 and KF850, respectively, compared to the CTRL experiments. Likewise, stronger correlation coefficients with the KMA's longest R30s are revealed in KF experiments ($r = 0.73\sim 0.75$) rather than CTRL experiments ($r = 0.57\sim 0.59$). The shortest axis of R30 showed that the use of 850 hPa wind fields is affecting the improvement of MAE and correlation coefficients. In particular, the shortest R30 estimates in the KF850 experiment had better performances compared to other experiments, with a correlation coefficient of 0.73 and MAE of 51.7 km.

The R30 biases are shown in all experiments except for the shortest R30 estimates in KF850 (Table 4.2). As expected, CTRL experiments showed significant negative bias values (about 244~436 km) in the longest R30 estimates. The longest R30s in the KF experiments are 51 km smaller and 96 km larger than estimates of KMA, respectively, for the KF1000 and KF850. For the shortest axis, the KF1000 experiment

showed a larger bias than the CTRL1000, which implies that the filtering method has no improvement in the 1000 hPa wind fields when estimating the shortest R30.

Table 4.2. Mean absolute error (MAE), correlation coefficient (r), and R30 bias between the longest and shortest axes of R30s estimated from four sensitivity experiments (see Table 4.1) and KMA best track data. Units for R30 bias and MAE are km.

R30	Experiment	MAE (km)	r	R30 bias (km)
Longest axes	CTRL1000	249.0	0.59	-244.0
	KF1000	66.0	0.73	51.2
	CTRL850	435.9	0.57	-435.7
	KF850	101.3	0.75	-96.2
Shortest axes	CTRL1000	63.6	0.63	25.3
	KF1000	65.2	0.65	51.7
	CTRL850	75.1	0.69	-28.3
	KF850	51.7	0.73	-0.1

Table 4.3. The equations for bias correction (slope and y-intercept) and the mean absolute errors (MAEs) of fitted R30 estimates in four experiments. The unit of MAE is km.

R30	Experiment	Fitted equation for bias correction		After bias correction
		slope	y-intercept	MAE (km)
Longest axes	CTRL1000	0.22	158.6	59.3
	KF1000	0.80	59.7	49.7
	CTRL850	0.19	141.3	61.7
	KF850	0.61	45.1	48.6
Shortest axes	CTRL1000	0.56	107.5	52.3
	KF1000	0.82	81.9	50.4
	CTRL850	0.45	101.7	49.7
	KF850	0.67	69.2	45.8

The wind radii are bias-corrected so that the initial wind radii match the current R30 estimates in each experiment. Table 4.3 shows the fitting equation for bias correction by each experiment, and MAEs of R30 estimates after applying the bias correction. When compared with the MAEs of R30 before the bias correction, the overall errors are significantly improved after applying the fitting equation for each experiment (Table 4.3). The bias-corrected R30s in KF experiments showed the lower MAEs than CTRL experiments, by approximately 10~13 km (2~4 km) for longest axis (shortest axis). In particular, the KF850 experiment had the smallest error in both the longest and shortest R30s, with MAE of about 49 km and 46 km, respectively (Table 4.3). In the automated system for estimating the TC wind radii, we emphasize that the KF experiments yield undoubtedly more effective and objective R30 estimates compared to the CTRL experiments.

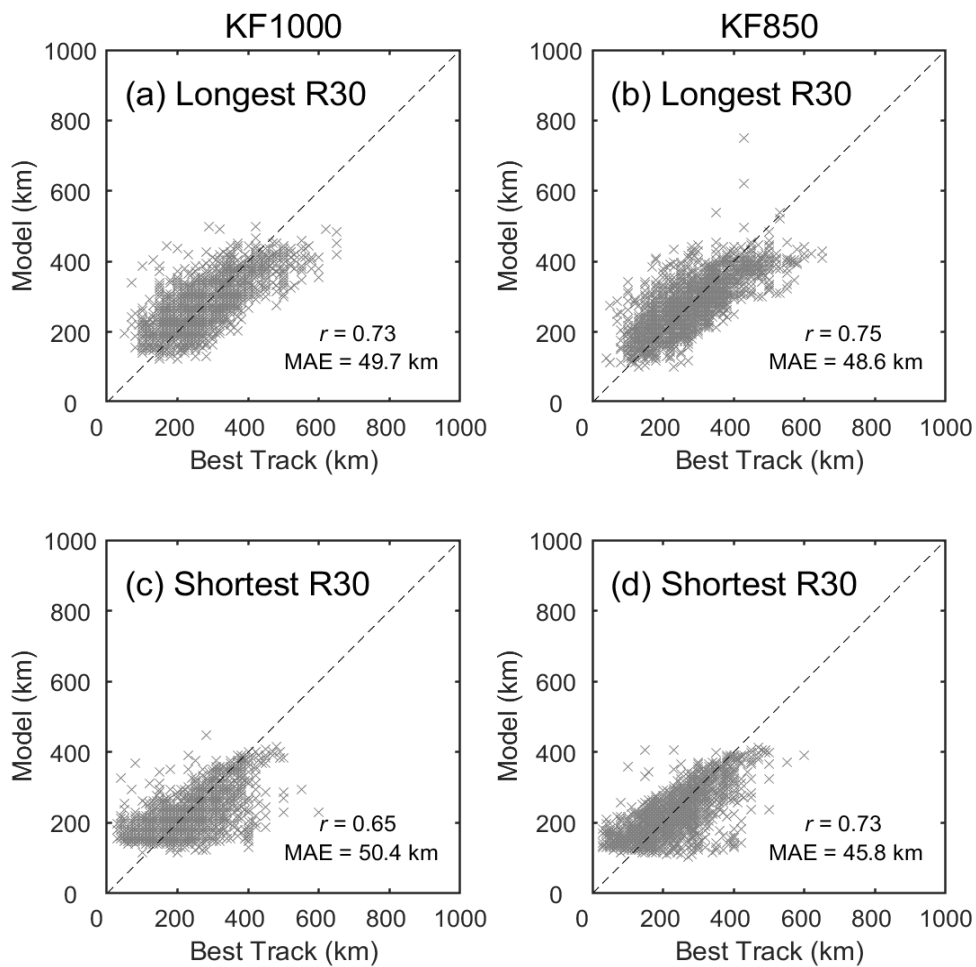


Figure 4.3. Comparison of estimates of longest (a-b) and shortest R30 (c-d) after bias correction from KF1000 (a, c) and KF850 (b, e), compared with KMA best track data during 2015-2019. Correlation coefficients (r) and mean absolute errors (MAE) are indicated in the bottom right corner of each panel. The unit in MAE is km.

In addition, overall distributions of bias-corrected R30 are further examined through the scatter plots of the longest axis and the shortest axis between the KMA best track and two KF experiments (Figure 4.3). In general, the longest R30 estimates in both KF experiments show a similar distribution overall, but tend to be smaller than the KMA best track at relatively large R30s (range of about 500~700 km) (Figures 4.3a and b). Meanwhile, the shortest axis shows relatively incomplete R30 distributions relative to the longest axis, especially in the small R30 estimates from KMA (less than 400 km) (Figures 4.3c and d). We find that the shortest axis is more difficult to objectively estimate the wind radii at a relatively small R30, which is more evident on the KF1000 using wind fields closer to the surface than KF850. This result once again showed that the wind field at 850 hPa is more suitable for reducing the errors in the objective and effective real-time estimation of the shortest R30 with the KF technique.

4.3.2. Predictions of longest and shortest R30

Based on the results in the previous section, final system for objectively calculating R30 is set to be applied to the model forecast winds in the following procedure (Figure 4.4). First, the u- and v- wind components used for estimating the wind radius and environmental variables for recalculating the storm center from the five-day GFS forecast fields with 6-hour intervals at the corresponding TC information, including the date and location are collected. Second, we produce wind data sets in which the background flow surrounding the TC is removed by TC wind fields at 1000 hPa and 850 hPa from the model's storm position, for each forecast time. Third, the filtered wind fields are changed as an azimuthally averaged radial profiles of 16 directions from the storm heading calculated from the TC information for each forecast time and wind field type, and the longest axis and the shortest axis for R30 are found in the radius values calculated from the sixteen profiles. Finally, bias correction is applied equally throughout the entire forecast of longest axis and shortest axis of R30 for 1000 hPa and 850 hPa, respectively. The final outputs calculated by this procedure are compared with CTRL experiments for all forecast lead times.

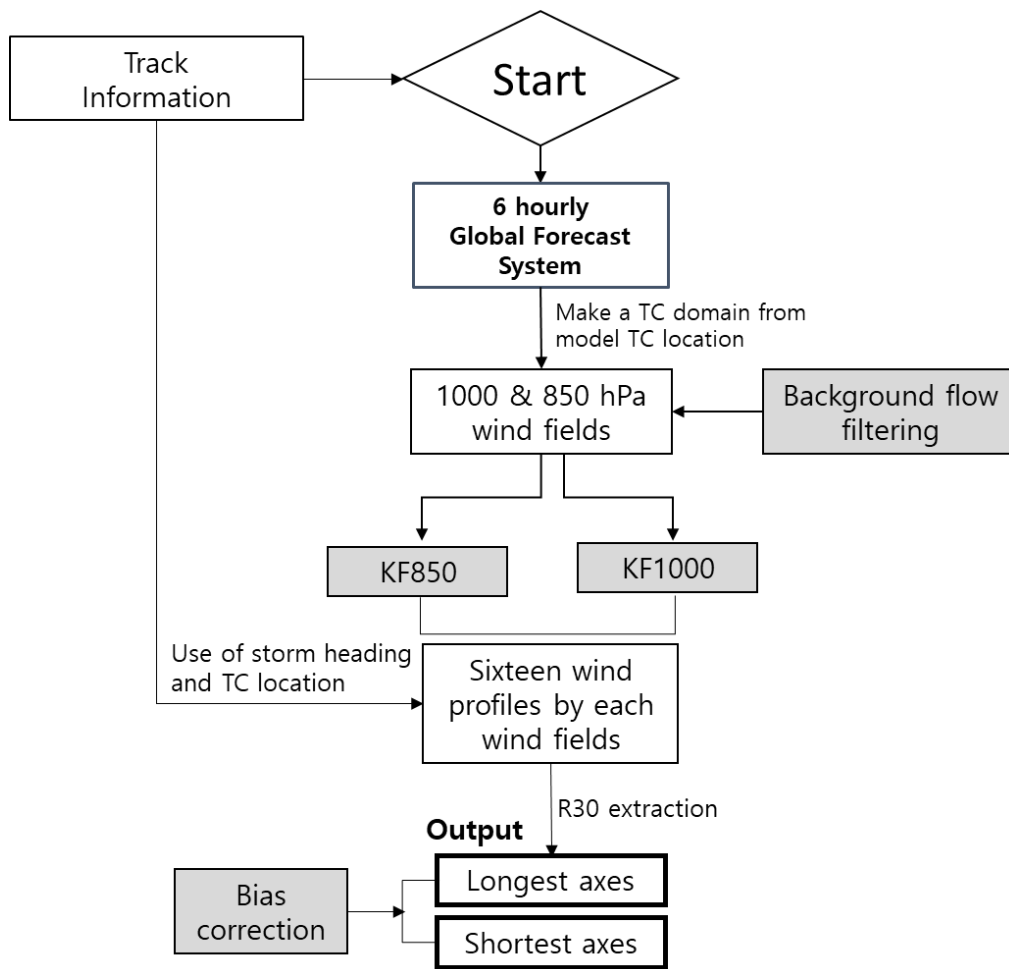


Figure 4.4. Schematic procedure for predicting the longest and shortest axes of R30 in this system.

Figure 4.5 shows the performances (MAE, R^2 and biases) of longest and shortest R30 outputs in final system (KF experiments) and in CTRL experiments for each forecast lead time, compared with estimates of KMA best track. For longest R30, the MAEs of the two KF experiments is relatively similar and increases gradually over prediction time (black and red solid lines in Figure 4.5a). When compared to CTRL experiments, the outputs of longest axis in the KF experiment showed a lower error before 48-h forecast lead times, by up to 8 km for KF1000 and 11 km for KF850, but had a larger error after 96-h prediction time with a large negative bias (ranging -20~40 km) and poorly R^2 (variance explained) results (below about 0.2) (Figure 4.5a-c).

These results can identify the problem from two perspectives of performance shown in KF experiments after 72-h prediction times. The first is the under-predictability of the wind fields in forecast data set. This is because the large negative bias means that the KF experiments greatly overpredicted the longest R30 compared to KMA. However, this issue is not considered a key factor in current performance, as the use of wind fields in CTRL experiments before removing the background flows was estimated to be smaller than the best track R30 estimates. Then, the second problem could be effect of bias correction applied equally to all prediction times. Sampson and Knaff (2015) suggested that most of the forecast wind radii in the NHC basins can be bias corrected so that the initial wind radii match the current analysis but that in most cases this bias correction should be phased out within 12 hour. As such, the parts of bias correction according to the prediction time is seen as one of the important parts for improving the longest R30 predictions in the current system. Nevertheless, we find that application of the same bias correction equation is valid for

longest R30 predictions by approximately 48-h forecast time (50~53 % variance explained) in this system (dashed line in Figure 4.5c).

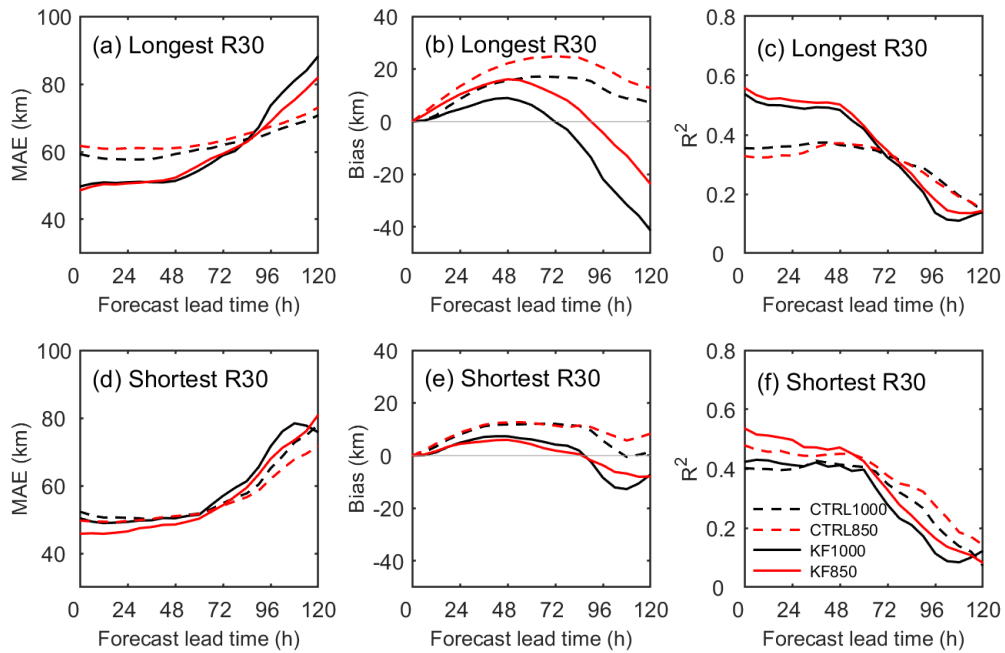


Figure 4.5. Comparisons of MAEs (a, c), R^2 (b, d), and bias (c, e) for longest (a-c) and shortest (d-e) R30 predictions of the outputs in current system (KF experiments, solid lines) and CTRL experiments (dashed lines) at 1000 hPa (black) and 850 hPa (red) using a model forecast wind fields at each lead time. The units of MAE and bias is km.

Meanwhile, the outputs of shortest R30 in the current system is very similar to the CTRL experiment according to the all prediction times, but shows a large difference in bias and R^2 (Figure 4.5d-f). In the performances of shortest R30 prediction, the KF850 outperforms the KF1000 overall, especially in R^2 (dashed lines in Figure 4.5f). A noticeable result is that the shortest R30 predictions in KF1000 has lower performance than the those of CTRL850 at most prediction times, suggesting that the use of a wind field of 850 hPa plays an important role for the estimating and predicting of shortest R30 in current system (Figure 4.5d-f). Compared with the longest R30 prediction in KF experiments, the outputs of the current system have similar results or trends in MAE and biases between the longest and shortest axes, but R^2 appears to be slightly lower in the shortest R30 predictions (Figure 4.5). This implies that the shortest axis in R30 is still more difficult to predict than the longest axis.

4.4. Summary and discussion

The wind field of the numerical weather prediction (NWP) is the most important data source for estimating and predicting the tropical cyclone (TC) wind radius in real-time. Although available high-resolution NWP datasets recently have been provided, the objective and reasonable determination of the area over TC-induced gale or 30-knot winds (R30), which are significantly affected by the complex and large-scale environmental flows surrounding the TC, remains a challenge. This study developed the objective and effective method for estimating the longest and shortest R30s in the western North Pacific (WNP) TCs from Global Forecast System (GFS) model, and applied to real-time R30 prediction.

When estimating the TC wind radius based on GFS winds, we used two ways to minimize the influence of background flow surrounding the TC and the terrain: a method for extracting the wind field of TC itself using the filtering technique, and a method using wind fields at 850 hPa, which is less sensitive to the effect of land. We first compared the longest and shortest axes of R30 estimated from the analysis-based winds with the estimates of KMA best track. The results showed the best performance for both longest and shortest R30 estimates using winds with filtering technique. More particularly, we found that the use of an 850 hPa wind field with the filtering technique has been improved the performance compared to other experiments, especially in the shortest R30.

For real-time prediction, the R30 estimated from the model analysis data was bias-corrected with the KMA's R30, and this correction was applied to estimate R30

using the 5-day forecast winds. The results showed a good performance until 48 hours, in which mean absolute error (MAE) and R^2 were 53 km (48 km) on average, and R^2 of 0.56 (0.54) for the longest (shortest) R30. After 72 hours, however, the predicted R30 showed a large error. This is likely because the real-time R30 results are dependent on the performance from the model forecast data, which is affected by additional errors such as the TC track and intensity. These results suggest that our TC wind radius estimation system can be a useful tool for estimating R30 in operational TC predictions. In this study, we used only the GFS prediction results, but ensemble prediction using various model results will further improve the R30 predictions by removing the model bias. This is what we want to do further by expanding this study.

5. Conclusion

The size of a tropical cyclone (TC) is an important factor in determining the possible TC-induced damaged area, and has an impact on the performance of TC intensity predictions and TC-induced storm surge/wave forecast modeling. Despite this importance, advances in research and prediction techniques related to TC size have not been largely addressed due to several issues, such as the lack of an objective dataset and difficulties in defining physically meaningful TC size. This dissertation investigated the three key topics to cover characteristics and predictions of TC size in terms of wind radii: (i) comparison of tropical cyclone wind radius estimates among three TC agencies over the western North Pacific, (ii) development of tropical cyclone wind radius prediction scheme based on statistical-dynamical approach and track pattern clustering, and (iii) prediction of the gale wind radius based on numerical weather prediction. The findings of this study can be summarized as follows.

First, this study investigated the characteristics of R30, R34, and R50 estimated by three agencies—the KMA, JMA, and JTWC—including their asymmetrical characteristics in terms of Vmax and spatial distributions, and examined how each agency considers TC size-related factors (Vmax, latitude, TC translation speed, and storm age). Comparing the mean values of both R30 and R50 of the three agencies, JMA had the largest mean value, which seems to be largely determined by TC winds combined with other mid-latitude synoptic systems, mainly for damage and disaster prevention purposes. On the other hand, the KMA and JTWC seem to determine the gale-force wind radius by focusing on the strong wind area of the TC itself. The factors

considered for estimating wind radii also were different between the agencies: KMA considered only V_{max} when estimating TC wind radii, while the JMA and JTWC considered not only V_{max} but also the latitude and TC translation speed partially, which is related to greater asymmetries.

Second, the statistical-dynamical regression model for predicting the change in TC size (R30 and R50) has been developed based on four clusters classified by distinct track patterns using the fuzzy c -Means clustering method and selected environmental predictors for each cluster, and evaluated the model performance. Analysis showed that the clustering model reduced errors, by 3-24% improvements at 24-120-h lead times in the training period and by a maximum of 8-9% at 72-96-h lead time in the testing period compared to the non-clustering model. Cluster 2 had the greatest improvement similarly in both periods rather than other clusters, because of the most distinct characteristics in terms of the tendency to TC size as well as to reduce variability in clustering (σ_c) leading to a better improvement in the forecast of TC size. In the real-time prediction of TC size, errors were still reduced using clustering models, but still need improvement in terms of model variance. However, through a representative case study, we found that real-time R30 predictions in the corresponding clusters are significantly influenced by track membership coefficients, which also reconfirms the possibilities of cluster analysis based on track patterns for improvement of TC wind radius prediction.

Finally, the system for objectively and effectively estimating the longest and shortest axes of the R30 from the available operational numerical weather prediction has been developed. Both longest and shortest axes of the R30 estimates using the

wind fields at 850 and 1000 hPa applied to filtering technique were significantly similar to the KMA best-track estimates. Particularly, the 850 hPa wind fields reproduced TC itself structure better than 1000 hPa winds, and reduced considerably the error of shortest R30 estimates in this system. For real-time prediction, when the wind fields at 6-120 hour forecast times were applied to the final automated system, the performance of both the longest and shortest R30s has been greatly improved by using the 850 hPa winds before the 48-hour forecast time, with mean absolute errors of 48~53 km on average, and R^2 of 0.54~0.56 maxima, respectively.

This thesis can be an important guideline for TC size estimation and prediction in terms of disaster prevention. The findings of agency-dependent characteristics of TC wind radius data help to better determine and understand the TC impact areas for TC risk reduction and management. In addition, our TC wind radii prediction schemes can be useful tool to determine the TC size in real-time, and prepare the warnings for the possible affected areas before the TC landfalls.

References

- Brand, S. 1972: Very large and very small typhoons of the western North Pacific Ocean. *J. Meteorol. Soc. Jpn.*, Ser. II, **50**, 332-341.
- Barcikowska, M., Feser, F., Von Storch, H., 2012: Usability of best track data in climate statistics in the western North Pacific. *Mon. Weather Rev.* **140**, 2818-2830.
- Bell, K., Ray, P.S. 2004: North Atlantic hurricanes 1977–99: surface hurricane-force wind radii. *Mon. Weather Rev.* **132**, 1167-1189.
- Bender, M.A., Marchok, T.P., Sampson, C.R., Knaff, J.A., Morin, M. J. 2017: Impact of storm size on prediction of storm track and intensity using the 2016 operational GFDL hurricane model. *Weather Forecast.*, **32**, 1491-1508.
- Bentamy, A., Croize-Fillon, D., Perigaud, C. 2008: Characterization of ASCAT measurements based on buoy and QuikSCAT wind vector observations. *Ocean Sci.* **4**, 265-274.
- Bezdek, J.C., Ehrlich, R, Full, W. 1984: FCM: The fuzzy c-means clustering algorithm. *Comput. Geosci.*, **10**, 191-203.
- Brennan, M.J., Hennon, C.C., Knabb, R. D. 2009: The operational use of QuikSCAT ocean surface vector winds at the National Hurricane Center. *Weather Forecast.*, **24**, 621-645.
- Camargo, S.J., Robertson, A.W., Gaffney, S.J., Smyth, P., Ghil, M. 2007: Cluster analysis of typhoon tracks. Part I: General properties. *J. Climate*, **20**, 3635-3653.

- Camargo, S.J., Robertson, A.W., Gaffney, S. J., Smyth, P., Ghil, M. 2007: Cluster analysis of typhoon tracks. Part II: Large-scale circulation and ENSO. *J. Climate*, **20**, 3654-3676.
- Cangialosi, J.P., Landsea, C.W. 2016: An examination of model and official National Hurricane Center tropical cyclone size forecasts. *Weather Forecast.*, **31**, 1293-1300.
- Cha, E.J., Knutson, T.R., Lee, T.C., Ying, M., Nakaegawa, T. 2020: Third assessment on impacts of climate change on tropical cyclones in the Typhoon Committee Region—Part II: Future projections. *Trop. Cyclone Res. Rev.* **9**, 75-86.
- Chan, K.T.F., Chan, J.C.L. 2012: Size and strength of tropical cyclones as inferred from QuikSCAT data. *Mon. Weather Rev.* **140**, 811-824.
- Chan, K.T.F., Chan, J.C.L. 2013: Angular momentum transports and synoptic flow patterns associated with tropical cyclone size change. *Mon. Weather Rev.* **141**, 3985-4007.
- Chan, K.T.F., Chan, J.C.L. 2015: Global climatology of tropical cyclone size as inferred from QuikSCAT data. *Int. J. Climatol.*, **35**, 4843-4848.
- Chan, K.T.F., Chan, J.C.L. 2018: The outer-core wind structure of tropical cyclones. *J. Meteorol. Soc. Jpn.*, Ser. II.
- Chavas, D.R., Emanuel, K.A. 2010: A QuikSCAT climatology of tropical cyclone size. *Geophys. Res. Lett.*, **37**.
- Chavas, D.R., Lin, N., Emanuel, K. 2015: A model for the complete radial structure of the tropical cyclone wind field. Part I: Comparison with observed structure. *J. Atmos. Sci.* **72**, 3647-3662.

- Chavas, D.R., Lin, N., Dong, W., Lin, Y. 2016: Observed tropical cyclone size revisited. *J. Climate*, **29**, 2923-2939.
- Chavas, D.R., Reed, K.A., Knaff, J.A. 2017: Physical understanding of the tropical cyclone wind-pressure relationship. *Nat. Commun.*, **8**, 1-11.
- Chu, P.S., Zhao, X., Ho, C.H., Kim, H.S., Lu, M.M., Kim, J.H. 2010: Bayesian forecasting of seasonal typhoon activity: A track-pattern-oriented categorization approach. *J. Climate*, **23**, 6654-6668.
- Chu, P.S., Zhao, X. 2011: Bayesian analysis for extreme climatic events: A review. *Atmos. Res.*, **102**, 243-262.
- Demuth, J.L., DeMaria, M., Knaff, J.A., Vonder Haar, T.H. 2004: Evaluation of Advanced Microwave Sounding Unit tropical-cyclone intensity and size estimation algorithms. *J. Appl. Meteorol.*, **43**, 282-296.
- Demuth, J.L., DeMaria, M., Knaff, J.A. 2006: Improvement of Advanced Microwave Sounding Unit tropical cyclone intensity and size estimation algorithms. *J. Appl. Meteorol, Clim.*, **45**, 1573-1581.
- DeMaria, M., Pickle, J.D. 1988: A simplified system of equations for simulation of tropical cyclones. *J. Atmos. Sci.* **45**, 1542-1554.
- DeMaria, M., Kaplan, J. 1994: A statistical hurricane intensity prediction scheme (SHIPS) for the Atlantic basin. *Weather Forecast.*, **9**, 209-220.
- Dolling, K., Ritchie, E.A., Tyo, J.S. 2016: The use of the deviation angle variance technique on geostationary satellite imagery to estimate tropical cyclone size parameters. *Weather Forecast.* **31**, 1625-1642.

- Dougherty, E., Davis, C.A. 2014: Observations of Wind Asymmetries in Atlantic Tropical Cyclones. In 2014 AGU Fall Meeting. AGU.
- Frank, W.M., Gray, W.M. 1980: Radius and frequency of 15 m s^{-1} (30 kt) winds around tropical cyclones. *J. Appl. Meteorol.* **19**, 219-223.
- Hill, K.A., Lackmann G.M., 2009: Influence of environmental humidity on tropical cyclone size. *Mon. Weather Rev.*, **137**, 3294–3315.
- Hodges, K., Cobb, A., Vidale, P.L. 2017: How well are tropical cyclones represented in reanalysis datasets?. *J. Climate*, **30**, 5243-5264.
- Holland, G.J., Merrill, R.T. 1984: On the dynamics of tropical cyclone structural changes. *Q. J. Roy. Meteor. Soc.*, **110**, 723-745.
- Hong, S., Shin, I. 2013: Wind speed retrieval based on sea surface roughness measurements from spaceborne microwave radiometers. *J. Appl. Meteorol. Clim.* **52**, 507-516.
- Houston, S.H., Shaffer, W.A., Powell, M.D., Chen, J. 1999: Comparisons of HRD and SLOSH surface wind fields in hurricanes: Implications for storm surge modeling. *Weather Forecast.*, **14**, 671-686.
- Irish, J.L., Resio, D.T., Ratcliff, J. J. 2008: The influence of storm size on hurricane surge. *J Phys Oceanogr*, **38**, 2003-2013.
- Kalnay, E. 2003: Atmospheric modeling, data assimilation and predictability. Cambridge university press.
- Kim, H.J., Moon, I.J., Oh, I. 2022: Comparison of Tropical Cyclone Wind Radius Estimates between the KMA, RSMC Tokyo, and JTWC. *Asia-Pac J Atmos Sci*, 1-14.

- Kim, H.S., Kim, J.H., Ho, C.H., Chu, P.S. 2011: Pattern classification of typhoon tracks using the fuzzy c-means clustering method. *J. Climate*, **24**, 488-508.
- Kim, S.H., Moon, I.J., Chu, P.S., 2018: Statistical-dynamical typhoon intensity predictions in the western North Pacific using track pattern clustering and ocean coupling predictors. *Weather Forecast.*, **33**, 347–365.
- Kilroy, G., Smith, R.K., Montgomery, M.T. 2017: A unified view of tropical cyclogenesis and intensification. *Q. J. Roy. Meteor. Soc.*, **143**, 450-462.
- Kimball, S.K., Mulekar, M.S. 2004: A 15-year climatology of North Atlantic tropical cyclones. Part I: Size parameters. *J. Climate*. **17**, 3555-3575.
- KMA 2019: Typhoon Best Track, Korea Meteorological Administration, 3pp (in Korean)
- Knaff, J.A., Sampson, C.R., DeMaria, M., Marchok, T.P., Gross, J.M., McAdie, C.J. 2007: Statistical tropical cyclone wind radii prediction using climatology and persistence. *Weather Forecast.* **22**, 781-791.
- Knaff, J.A., Harper, B. A. 2010: Tropical cyclone surface wind structure and wind-pressure relationships. Seventh Int. In Workshop on Tropical Cyclones, La Reunion, France, WMO, KN1.
- Knaff, J.A., DeMaria, M., Molenaar, D.A., Sampson, C.R., Seybold, M.G. 2011: An automated, objective, multiple-satellite-platform tropical cyclone surface wind analysis. *J. Appl. Meteorol. Clim.* **50**, 2149-2166.
- Knaff, J.A., Longmore, S.P., Molenaar, D.A. 2014: An objective satellite-based tropical cyclone size climatology. *Journal of Climate*, **27**, 455-476.

- Knaff, J.A., Slocum, C.J., Musgrave, K.D., Sampson, C.R., Strahl, B.R. 2016: Using routinely available information to estimate tropical cyclone wind structure. *Mon. Weather Rev.* **144**, 1233-1247.
- Knaff, J.A., Sampson, C.R., Chirokova, G. 2017: A global statistical–dynamical tropical cyclone wind radii forecast scheme. *Weather Forecast.* **32**, 629-644.
- Knaff, J.A., Sampson, C.R., Musgrave, K.D. 2018: Statistical tropical cyclone wind radii prediction using climatology and persistence: Updates for the western North Pacific. *Weather Forecast.*, **33**, 1093-1098.
- Knaff, J.A., et al. 2021: Estimating tropical cyclone surface winds: Current status, emerging technologies, historical evolution, and a look to the future. *Trop. Cyclone Res. Rev.* **10**, 125-150.
- Kossin, J.P., et al. 2007: Estimating hurricane wind structure in the absence of aircraft reconnaissance. *Weather Forecast.*, **22**, 89-101.
- Kunii, M. 2015: Assimilation of tropical cyclone track and wind radius data with an ensemble Kalman filter. *Weather Forecast.*, **30**, 1050-1063.
- Kurihara, Y., Bender, M.A., Ross, R.J. 1993: An initialization scheme of hurricane models by vortex specification. *Mon. Weather Rev.*, **121**, 2030-2045.
- Kimball, S.K., Mulekar, M.S. 2004: A 15-year climatology of North Atlantic tropical cyclones. Part I: Size parameters. *J. Climate.*, **17**, 3555-3575.
- Kwon, M. 2012: Estimation and statistical characteristics of the radius of maximum wind of tropical cyclones using COMS IR imagery. *Atmosphere.*, **22**, 473-481.
(in Korean with English abstract)

- Landsea, C.W., Franklin, J.L. 2013: Atlantic hurricane database uncertainty and presentation of a new database format. *Mon. Weather Rev.*, **141**, 3576-3592.
- Le, T.A, Takagi, H., Heidarzadeh, M., Takata, Y., Takahashi, A. 2019: Field Surveys and Numerical Simulation of the 2018 Typhoon Jebi: Impact of high waves and storm surge in semi-enclosed Osaka bay, Japan. *Pure. Appl. Geophys.*. **176**, 4139-4160.
- Lee, C.S., Cheung, K.K., Fang, W.T., Elsberry, R.L. 2010: Initial maintenance of tropical cyclone size in the western North Pacific. *Mon. Weather Rev.* **138**, 3207-3223.
- Lee, Y.K., Kwon, M. 2015: An Estimation of the of Tropical Cyclone Size Using COMS Infrared Imagery. *Atmosphere*. **25**, 569-573. (in Korean with English abstract).
- Lei, L., Whitaker, J.S. 2017: Evaluating the trade-offs between ensemble size and ensemble resolution in an ensemble-variational data assimilation system. *J. Adv. Model. Earth Sy.*, **9**, 781-789.
- Lin, N., Lane, P., Emanuel, K.A., Sullivan, R.M., Donnelly, J.P. 2014: Heightened hurricane surge risk in northwest Florida revealed from climatological-hydrodynamic modeling and paleorecord reconstruction. *J. Geophy. Res-Atmos.*, **119**, 8606-8623.
- Lin, N., Jing, R., Wang, Y., Yonekura, E., Fan, J., Xue, L. 2017: A statistical investigation of the dependence of tropical cyclone intensity change on the surrounding environment. *Mon. Weather Rev.*, **145**, 2813-2831.

- Lin, Y., Zhao, M., Zhang, M., 2015: Tropical cyclone rainfall area controlled by relative sea surface temperature. *Nat. Commun.*, **6**, 1-7.
- Liu, K.S., Chan, J.C. 2002: Synoptic flow patterns associated with small and large tropical cyclones over the western North Pacific. *Mon. Weather Rev.*, **130**, 2134-2142.
- Lungu, T., Callahan, P.S. 2006: QuikSCAT science data product user's manual: Overview and geophysical data products. D-18053-Rev A, version, 3.
- Matyas, C. J. 2010: A geospatial analysis of convective rainfall regions within tropical cyclones after landfall. *Int. J. Appl. Geo. Res.*, **1**, 71-91.
- Marchok, T.P. 2002: How the NCEP tropical cyclone tracker works. In Preprints, 25th Conf. on Hurricanes and Tropical Meteorology, San Diego, CA, Amer. Meteor. Soc. P (Vol. 1).
- McAdie, C.J. 2004: Development of a wind-radii CLIPER model. Preprints, 24th Conf. on Hurricanes and Tropical Meteorology, Miami, FL, Amer. Meteor. Soc., **5**, 170–171.
- Merrill, R.T. 1984: A comparison of large and small tropical cyclones. *Mon. Weather Rev.* **112**, 1408-1418.
- Misra, T., et al. 2019: SCATSAT-1 Scatterometer: an improved successor of OSCAT. *Curr. Sci.* **117**, 941-949.
- Muroi, C. 2018: Brief History and recent activities of RSMC Tokyo-Typhoon Centre. *Trop. Cyclone Res. Rev.* **7**, 57-64.

- Pérez-Alarcón, A., Sorí, R., Fernández-Alvarez, J.C., Nieto, R., Gimeno, L. 2021: Comparative climatology of outer tropical cyclone size using radial wind profiles. *Weather and Climate Extremes*, **33**, 100366.
- Powell, M. D., Reinhold, T. A. 2007: Tropical cyclone destructive potential by integrated kinetic energy. *B. Am. Meteorol. Soc.*, **88**, 513-526.
- Pun, I.F., Lin, I.I., Lien, C.C., Wu, C.C. 2018: Influence of the size of Supertyphoon Megi (2010) on SST cooling. *Mon. Weather Rev.*, **146**, 661-677.
- Tallapragada, V. et al., 2015: Forecasting tropical cyclones in the western North Pacific basin using the NCEP operational HWRF: Real-time implementation in 2012. *Weather Forecast.*, **30**, 1355-1373.
- Quiring, S.M., Schumacher, A.B., Guikema, S.D. 2014: Incorporating hurricane forecast uncertainty into a decision-support application for power outage modeling. *B. Am. Meteorol. Soc.*, **95**, 47-58.
- Sampson, C.R., Wittmann, P.A., Tolman, H.L. 2010: Consistent tropical cyclone wind and wave forecasts for the US Navy. *Weather Forecast.*, **25**, 1293-1306.
- Sampson, C.R., Knaff, J.A. 2015: A consensus forecast for tropical cyclone gale wind radii. *Weather Forecast.*, **30**, 1397-1403.
- Sampson, C.R., Fukada, E.M., Knaff, J.A., Strahl, B.R., Brennan, M.J., Marchok, T. 2017: Tropical cyclone gale wind radii estimates for the western North Pacific. *Weather Forecast.*, **32**, 1029-1040.
- Sampson, C.R., Goerss, J.S., Knaff, J.A., Strahl, B.R., Fukada, E.M., Serra, E.A. 2018: Tropical cyclone gale wind radii estimates, forecasts, and error forecasts for the western North Pacific. *Weather Forecast.* **33**, 1081-1092.

- Schenkel, B.A., Hart, R.E. 2012: An examination of tropical cyclone position, intensity, and intensity life cycle within atmospheric reanalysis datasets. *J. Climate*, **25**, 3453-3475.
- Schenkel, B.A., Lin, N., Chavas, D., Oppenheimer, M., Brammer, A. 2017: Evaluating outer tropical cyclone size in reanalysis datasets using QuikSCAT data. *J. Climate*. **30**, 8745-8762.
- Song, J., Klotzbach, P.J. 2016: Wind structure discrepancies between two best track datasets for western north Pacific tropical cyclones. *Mon. Weather Rev.* **144**, 4533-4551.
- Song, J., Duan, Y., Klotzbach, P.J. 2020: Revisiting the relationship between tropical cyclone size and intensity over the western North Pacific. *Geophys. Res. Lett.*, **47**, e2020GL088217.
- Tang, C.K., Chan, J.C.L., Yamaguchi, M. 2020: Effects of the outer size on tropical cyclone track forecasts. *Meteorological Applications*, **27**, e1888.
- Yeh, J.H., Joung, F.J., Lin, J.C. 2014: CDV index: a validity index for better clustering quality measurement. *J. Comput. and Commun.*, **2**, 163.
- Wang, S., Toumi, R. 2022: An analytic model of the tropical cyclone outer size. *npj Climate and Atmospheric Science*, **5**, 1-10.
- Wang, Z. 2012: Thermodynamic aspects of tropical cyclone formation. *J. Atmos. Sci.*, **69**, 2433-2451.
- Weber, H.C., Lok, C.C., Davidson, N.E., Xiao, Y. 2014: Objective estimation of the radius of the outermost closed isobar in tropical cyclones. *Trop. Cyclone Res. Rev.*, **3**, 1-21.

- Weatherford, C.L., Gray, W.M. 1988: Typhoon structure as revealed by aircraft reconnaissance. Part I: Data analysis and climatology. *Mon. Weather Rev.* **116**, 1032-1043.
- Whitney, L.D., Hobgood, J.S. 1997: The relationship between sea surface temperatures and maximum intensities of tropical cyclones in the eastern North Pacific Ocean. *J. Climate*, **10**, 2921-2930.
- Wu, C.C., Lien, G.Y., Chen, J.H., Zhang, F. 2010: Assimilation of tropical cyclone track and structure based on the ensemble Kalman filter (EnKF). *J. Atmos. Sci.*, **67**, 3806-3822.
- Wu, L., Tian, W., Liu, Q., Cao, J., Knaff, J.A. 2015: Implications of the observed relationship between tropical cyclone size and intensity over the western North Pacific. *J. Climate*. **28**, 9501-9506.
- Xu, J., Wang, Y. 2010: Sensitivity of the simulated tropical cyclone inner-core size to the initial vortex size. *Mon. Weather Rev.*, **138**, 4135–4157.
- Xu, J., Wang, Y. 2018: Dependence of tropical cyclone intensification rate on sea surface temperature, storm intensity, and size in the western North Pacific. *Weather Forecast.*, **33**, 523-537.
- Zhao, K., Zhao, C. 2019: Evaluation of HY-2A scatterometer ocean surface wind data during 2012–2018. *Remote Sens.* **11**, 2968.

국문 초록

열대저기압 (Tropical cyclone, TC)의 크기는 태풍의 직접적인 영향을 받는 영역을 결정 할 수 있기 때문에 TC의 방재 측면에서 중요한 의미를 갖는다. 그러나 태풍의 크기는 장기적이고 객관적인 관측 자료의 부족과 합리적인 TC의 영역을 결정하는 것에 대한 어려움과 같은 문제로 인해 현재까지도 광범위하게 연구 되지 않았다. 본 학위논문은 크게 (i) 한국, 일본, 미국 기관에서 추정된 TC 바람 반경의 상호비교, (ii) 통계-역학적 방법 및 태풍 진로 분류를 기반으로 한 TC의 바람 반경 예측, 그리고 (iii) Global Forecast System (GFS) 모델 자료를 기반으로 한 북서태평양의 강풍반경 예측과 관련하여, 바람으로부터 추정된 반경 측면에서 TC의 크기와 관련된 세 가지 주제를 다루었다.

먼저, 본 연구는 2015에서 2018년 동안 북서태평양 (western North Pacific, WNP)의 TC 기관인 Korea Meteorological Administration (KMA), Japan Meteorological Agency (JMA), 그리고 Joint Typhoon Warning center (JTWC) 에서 제공하는 강풍반경 (R30 또는 R34)과 폭풍반경(R50) 추정치들에서 나타나는 특징들을 조사 하였다. 그 결과, KMA의 R30 과 R50 추정치는 JMA의 추정치보다 각각 38% 및 29% 더 작았으며, JTWC보다 R30은 더 크고 (11%) R50은 더 작은 (12%) 추정치를 가지고 있었다. 이와 같은 기관 별 차이는 TC 기관이 태풍 자체에의 바람에만 초점을 맞추어 바람 반경을 추정하는지, 아니면 태풍정보를 보다 포괄적으로 만들기 위해서 다른 중위도의 종관 시스템 환경과 결합된 태풍의 반경을 추정하는지에 따라 크게 결정되는 것으로 보여진다. 전자는 주로 KMA와 JTWC에서, 후자는 주로 JMA에서 행해지는 것으로 나타났다. 또한 바람 반경을 추정하기 위해 고려하는 요소도 기관마다 달랐다. KMA는 강도가

강할수록 반경이 더 큰 경향을 보이며 태풍 강도에 크게 의존하는 반면에, JMA 와 JTWC 는 KMA 보다 태풍 강도에 덜 의존하지만 크기를 추정할 때 위도와 TC 의 이동속도를 추가로 고려한다는 것을 보여주었다. 특히, JMA 와 JTWC 에서 고려된 TC 의 이동속도는 추정된 바람반경이 KMA 에서 추정한 것보다 평균적으로 더 큰 비대칭 (가장 긴 반경과 가장 짧은 반경 사이의 더 큰 차이) 을 나타내는 이유를 뒷받침 한다.

둘째, 북서태평양의 TC 의 대칭적인 R30 및 R50을 예측 하기 위한 운용계획은 태풍 진로 분류와 통계적 회귀 방법을 사용하여 개발되었다. 통계 모델의 훈련을 위해 5일 간격으로 분류된 TC 의 진로는 fuzzy c-means clustering 방법에 따라 4개의 클러스터로 분류되었다. 현재의 통계-역학 모델은 각 클러스터 및 각 예측시간에 따라서 계산된 11개의 예측 변수에서 선정된 2~8개의 변수에 대하여 다중 선형 회귀를 적용하였다. 이 연구에서는 초기시간에서 TC 크기의 proxy 를 나타내는 5-knot 바람반경 (R5) 의 변화를 예측을 위해 사용된 종속변수로 사용하였다. 모델의 성능은 훈련(2008~2016)과 테스트(2017~2018) 기간으로 나누어 비교되었으며, 클러스터링이 TC 크기 예측에 미치는 영향에 대해서 비클러스터링 모델과 클러스터링 모델의 성능을 비교하여 평가되었다. 그 결과, 클러스터링 모델이 훈련 기간 동안 모든 예측시간에서 TC 크기 예측을 3-24% 개선하고 있었으며, 특히 Cluster 2에서 최대 43%의 상당한 개선을 보였다. 테스트 기간 동안, 클러스터링 모델은 모든 예측 리드 타임에서 평균 오차의 감소와 Cluster 2에서 가장 큰 개선을 보였으나 훈련 기간에 비해 개선이 상대적으로 작았다. Cluster 2의 경우 대부분의 TC 가 강하게 발달하면서 크기가 계속 증가하는 뚜렷한 경향이 clustering 을 통해 TC 크기의 표준편차 또는 가변성을 크게 감소시키게 됨으로써 보다 스마트한 예측인자의 선정을 가능하게 하여, 궁극적으로 TC 크기 예측을 향상시키는 것으로 나타났다. 또한 2017년과 2018년

TC 들의 실시간 R30 과 R50 예측에서, 전체 예측 시간에서 평균 절대 오차는 각각 R30과 R50에서 $61 \pm 27\text{km}$ 와 $21 \pm 9\text{km}$ 를 보이며, 클러스터링 모델의 오차가 비 클러스터링 모델 오차에 비해 약 18~19% 적은 것으로 나타났다. 현재 개발된 클러스터링 모델의 실시간 예측에 대해 추가적으로 분석 했을 때, TC 의 강도예측 및 R5 추정치에서 나타나는 고유한 오차와 태풍의 진로가 두 군집 사이에 위치하여 특정 군집으로 분류하기 어려운 경우에 나타나는 오차가 실시간 예측 성능을 저하시키는 것으로 나타났다.

마지막으로, WNP TC 의 강풍반경 (R30)을 객관적으로 추정하고 예측하기 위한 자동화 시스템은 Global Forecast System (GFS) 의 예측 바람 자료를 사용하여 개발 되었다. 이 시스템에서 GFS 자료로부터 R30의 장축과 단축을 효과적으로 추정하기 위하여, 1000 hPa 과 850 hPa 바람장에서 TC 자체의 바람을 생성하기 위한 필터링 기술을 적용하였다. 결과는 필터링이 적용된 850 hPa 의 바람장을 사용하면 R30 추정치의 성능의 상당한 개선을 보여 주었으며, 특히 단축에서 더 큰 개선이 나타남을 확인 하였다. 실시간 R30의 예측을 위해 필터링 기술과 반경 추정치의 bias correction 이 포함된 최종적인 시스템에 5일 모델 예측 바람장을 적용하였다. 예측된 R30의 성능은 48 시간 예측 까지 850 hPa 의 바람장을 사용 함으로서 크게 개선되었음을 확인 하였으며, 장축과 단축에서 각각 평균적으로 약 53 km (48 km) 의 절대 평균 오차를 보였다.

